Modelling and Design of Graphene-based THz Devices

by

Liang Yang

A thesis submitted in partial fulfilment of
the requirements for the degree of
Doctor of Philosophy

School of Electronic Engineering and Computer Science
Queen Mary University of London
United Kingdom

November 2018

TO MY PARENTS

Abstract

In recent years, terahertz (THz) frequency band has gained great interest of researchers in a number of fields due to attractive THz applications such as wireless communications, remote sensing and imaging. Graphene, a two-dimensional carbon material with extraordinary properties in the THz spectrum, has been considered as a promising candidate for novel THz devices to achieve these valuable applications. As related modelling methods are indispensable, this thesis summarises my PhD work on the development of novel numerical methods for graphene-based THz devices.

In the THz spectrum, both electrostatic bias and magnetostatic bias can change the conductivity of graphene. A finite-difference time-domain (FDTD) modelling based on auxiliary element method is proposed for the tunable linear responses of graphene. Moreover, graphene has nonlinear responses under strong THz radiation. A novel FDTD method, which is based on a $J - E$ characteristic formula, is proposed for modelling the nonlinear electrodynamic responses of graphene in the THz spectrum. FDTD results of linear responses are in agreement with theoretical and measurement results in the published literature. Nonlinear FDTD results successfully demonstrate nonlinear phenomena including odd-harmonic generations and frequency-mixing effects. The proposed FDTD modelling methods can be used as full-wave design tools for graphene-based devices.

In addition, the FDTD modelling methods are utilised in the design of electrically tunable graphene-based reflectarray antennas and magnetically tunable graphene-based reflectors. Regarding the tunable reflectors, their performance has been experimentally explored and discussed. In addition, a modified equivalent circuit modelling is developed to extract the parameters of graphene from measurement data.

Acknowledgments

Foremost, I want to express my sincere gratitude to my primary supervisor Prof. Yang Hao. His guidance and continuous support have encouraged me to go through the four-year research in London. I am also particularly grateful to my second supervisor Dr. Khalid Z. Rajab and independent assessor Dr. Akram Alomainy for proofreading of my stage reports and valuable comments on my research. Additionally, I appreciate the funding provided by the China Scholarship Council (CSC).

I would like to thank Dr. Anestis Katsounaros, Dr. Oleksandr Sushko, Dr. Max Munoz Torrico, Dr. Luigi La Spada, Dr. Henry Giddens, Dr. Jing Tian, Dr. Darryl Smith and Dr. Hangfeng Zhang for the research work we did together, and thank the help from Dr. Jingbo Wu at University of Cambridge and the cooperation provided by Prof. Alexey B. Kuzmenko and Dr. Jean-Marie Pomerol at University of Geneva. Moreover, I would like to give my thanks to other colleagues in our Antenna & Electromagnetics Research Group for valuable discussions, especially Dr. Hai Lin, Dr. Hongyu Shi, Dr. Yangjie Liu, Dr. Qiao Cheng, Dr. Biyi Wu, Dr. Jiefu Zhang, Dr. Menglin Chen and Mr. Dingliang Wen. I also would like to thank the rest of the group members for the positive working atmosphere we created together.

As the part of my life in London, I am very fortunate to acquire many friends: Dr. Min Zhou, Dr. Rui Zhang, Dr. Li Cheng, Dr. Ke Yang, Dr. Kang Liu, Dr. Jia Ran, Mr. Wanlin Li, Dr. Baiyang Liu, Mr. Yujie Liu, Mr. Hongchen Chu and Mr. Su Wei. It is friendships that enrich the memory of the last four years.

Finally and very importantly, thanks and appreciations must go to my parents. Their most profound love and unconditional support have always motivated me.

Table of Contents

List of Figures

List of Tables

List of Abbreviations

2D	Two-Dimensional
3D	Three-Dimensional
ADI-FDTD	Alternating Direction Implicit Finite-Difference Time-Domain
BEM	Boundary Element Method
CFL	Courant–Friedrich–Levy
CPML	Convolutional Perfectly Matched Layer
CR	Cyclotron Resonance
CVD	Chemical Vapour Disposition
ECM	Equivalent Circuit Modelling
EFIE	Electric Field Integral Equation
EM	Electromagnetic
FDM	Finite-Difference Method
FDTD	Finite-Difference Time-Domain
FEM	Finite Element Method
FHG	Fifth-order Harmonic Generation
FOM	Figure-of-Merit
FR	Faraday Rotation
FTIR	Fourier-Transform Infrared

GMP	Graphene Magnetoplasmon
h-BN	Hexagonal Boron Nitride
HIE-FDTD	Hybrid Implicit-Explicit Finite-Difference Time-Domain
IMD	Intensity Modulation Depth
IR	Infrared
ITO	Indium Tin Oxide
KR	Kerr Rotation
LOD-FDTD	Locally One-Dimensional Finite-Difference Time-Domain
MFIE	Magnetic Field Integral Equation
MoM	Method of Moments
PBC	Periodic Boundary Condition
PEC	Perfect Electric Conductor
PML	Perfect Match Layer
PMMA	Polymethyl Methacrylate
RTA	Relaxation Time Approximation
SBC	Surface Boundary Condition
SIBC	Surface Impedance Boundary Condition
SPP	Surface Plasmon Polariton
SRR	Split-Ring Resonator
STM	Scanning Tunnelling Microscopy
TF/SF	Total Field/Scattered Field
THG	Third-order Harmonic Generation
THz	Terahertz
UHV	Ultra-High Vacuum

Chapter 1

Introduction

The terahertz (THz) region, broadly defined as 0.1-30 THz (from 3 mm to 10 µm), has gained interest of researchers due to its unique spectral properties [1]. For example, in astronomy, the THz emission and absorption spectrum of molecules have been used for space exploration [2]. In medicine and security, THz radiation has been used for human body imaging [3] with lower health risks compared to X-ray radiation [4]. Moreover, THz radiation provides carrier frequencies higher than those used in current commercial wireless communication systems and has also been used to increase channel capacities for short-range ultra-broadband communication [5]. Various promising applications have made the THz region a growing research topic in the last decades [6].

The useful applications mentioned above require the support of investigations on material properties that are important for THz devices [7]. Researchers interested in the THz region have investigated properties of materials with different dimensions. In terms of traditional three-dimensional materials, such as silica [8] and gold [9], their permittivity and conductivity have been characterised at the THz spectrum. Moreover, a set of two-dimensional (2D) materials, discovered in recent years, such as graphene [10], phosphorene [11], borophene [12], silicene [13], transition-metal dichalcogenides [14] have also been investigated.

Among these novel 2D materials, graphene has triggered research in different fields due to its unique mechanical, thermal and electromagnetic (EM) [15] properties. It is necessary to propose numerical modelling techniques accounting for these properties to assist detailed device designs.

In this chapter, the THz region is introduced with its definition and many examples of its applications. Then, three numerical modelling methods that are popular in electromagnetics are introduced. The background of graphene deserves a separate chapter as provided in chapter 2.

1.1 The Terahertz Region

In this section, the terahertz region used in this thesis is clearly defined, and examples of THz applications are introduced.

1.1.1 Definition

In 2002, the spectrum ranging from 0.3 THz and 30 THz was proposed as the "terahertz gap" due to the lack of devices working as sources or detectors [16]. Three years later, the THz gap was defined as the spectrum in the region from 0.1–10 THz, with wavelengths from 3 mm to 30 µm [17]. According to the interest of researchers from different communities, the definition of the THz gap has varied over the past 16 years. However, the definition has been within the range of 0.1 THz and 30 THz in most situations. In this thesis, the THz region is defined as 0.1–30 THz due to the properties of graphene and graphene-based devices which are studied in the following chapters.

1.1.2 Examples of Terahertz Applications

The THz spectrum has inspired researchers to explore many exciting applications due to its close relation to daily life [18–20], such as imaging and wireless communications.

1.1.2.1 Terahertz Imaging

A great interest in the imaging by THz techniques has emerged due to the two advantages of THz radiation. The first one is the relatively low photon energy which avoids ionising effects on biological tissues [21]. The second one is the unique biological and chemical information provided by THz radiation [22]. In recent years, sensitive graphene-based THz emitters [23] and detectors [24] have been proposed, which promise applications for fast imaging of macroscopic samples [25].

In the medical field, tissues have different refractive index and absorption coefficients [26]. Tissue images can be obtained by processing the variations in reflection [27] or transmission [28]. Imaging resolution of several hundred nanometers has been achieved at the THz spectrum [29]. However, the absorption by water is an unavoidable issue of THz imaging, which limits the penetration depth of THz waves in moist tissues. The clinically prepared thin tissue samples are required for the imaging of the inside of many tissues [30].

In the security field, explosives, weapons and drugs have unique spectral "fingerprints" in the THz range [3]. Even though the energy of THz radiation is not high, it still has the ability to penetrate cloth and papers [31] which are opaque in the visible region. The remote imaging of concealed dangers is essential to critical security places. But, due to the absorption by the human body, it is a challenge for THz imaging to detect the dangers which are surgically implanted into the human body.

1.1.2.2 Terahertz Wireless Communications

The most fundamental motivation encouraging investigations on THz wireless communications are the requirements on broader bandwidth compared to wireless communication systems using millimetre waves [32].

In the last decade, the capabilities of THz wireless links have been demonstrated, such as a 12.5-Gbit/s data rate at 0.3 THz over 0.5-m distance [33] and a 100-Gbit/s data rate at 0.2 THz over 20-m distance [34]. The data rate of THz wireless links is much higher than the 4G Long Term Evolution-Advanced system, which is the current commercial wireless system with the date rate of 50–100 Mbit/s [35]. However, as can be seen from these examples, the primary challenge for THz links is the short communication distance.

In order to increase the communication distance, the THz windows with lower atmospheric absorption can be used to reduce the free-space losses [36], and high output power of THz transmitters is also required. Silicon germanium technologies, gallium nitride technologies and complementary metal-oxide-semiconductor technologies have all been investigated to improve THz band transceivers [37]. In addition, graphene-based antennas have been expected to play a potential role in THz transceivers [38].

1.2 Numerical Modelling Techniques in Electromagnetics

Numerical modelling techniques used in electromagnetics are powerful tools for the analysis of complex electromagnetic problems. These techniques can benefit designs of graphene-based devices as well. Three numerical modelling techniques with advantages and limitations are briefly reviewed in this section.

1.2.1 Finite Element Method

The finite element method (FEM) has been applied for solving multi-disciplinary engineering problems including fluid mechanics, solid mechanics, heat transfer and electromagnetics [39].

The FEM modelling subdivides the entire modelled domain into subdomains, i.e. elements. In two-dimensional FEM modelling, the elements can be rectangular, triangular and quadrilateral. In three-dimensional FEM modelling, tetrahedral, triangular prisms and rectangular bricks are employed to represent structure geometries. Such shapes of FEM elements provide the advantage on modelling structures with irregular geometries and capturing local effects. After the domain discretisation, interpolation functions, i.e. basis functions, are selected for elements. Usually, interpolation functions are first, second or higher order polynomials. Then, a system of equations is formulated by using either the Ritz variational method or the Galerkin method [40]. With related boundary conditions, the equation system can be solved using linear algebra techniques.

Broadband properties are essential for structures in electromagnetics. In this case, the traditional frequency-domain FEM is very time-consuming because the equation system needs to be solved at isolated frequencies. Fast frequency sweep can be employed to reduce the simulation time [41]. Even though time-domain FEM has been proposed, the equation system has to be solved at each time step [42].

1.2.2 Method of Moments

The method of moments (MoM) is a numerical method of solving a system of linear integral equations across several industries. The problems in electromagnetics can be expressed as the electric field integral equation (EFIE) or the magnetic field integral equation (MFIE) [43]. Essentially, MoM is the boundary element method (BEM), which is commonly known as MoM in electromagnetics [44].

In MoM, the unknown electric field or magnetic field is expended as a sum of basis functions with unknown coefficients. A linear equation system can be obtained by enforcing boundary conditions. The EFIE enforces the boundary condition on the electric field, and the MFIE enforces the boundary condition on the magnetic field. The Galerkin testing can be used to calculate the unknown coefficients [45].

To some extent, the procedure of MoM is similar to FEM. However, MoM is based on integral equations, and FEM is based on differential equations. Another difference is that MoM only needs to discretise the surface of the scatter or antenna because electromagnetic sources are the quantities of interest in MoM [46]. The less domain discretisation is an advantage compared to FEM which requires the entire domain to be discretised. However, the computing resource required by arbitrary large structures is a limitation to MoM.

1.2.3 Finite-Difference Time-Domain Method

The finite-difference time-domain (FDTD) method is a time-domain version of the finite-difference method (FDM) which uses finite differences to approximate the derivatives for solving differential equations. FDM is more suitable for time-domain implementation with comparison to FEM and MoM [47]. The latter two methods are usually considered as frequency-domain methods.

The basic FDTD method uses central-difference approximations to calculate the space and time derivatives of Maxwell's curl equations. Its modelling space is represented by interleaved cubical cells of discrete points containing electric fields or magnetic fields [48]. The electric and magnetic fields are updated at different time steps by using a leapfrog algorithm until the desired result is obtained. The size of its time step depends on the size of cells due to numerical stability issues [49]. The frequency-dispersive constitutive parameters of materials, which described by the Debye model, the Lorentz model or the Drude model, can be straightforwardly formulated in the time domain [50]. Arbitrary

frequency-dispersive media can employ the Padé approximation theory for broadband simulations [51].

As a time-domain method, the FDTD method has inherent modelling capabilities in simulations of broadband and nonlinear material properties [52]. Because this thesis mainly discusses the broadband linear and nonlinear THz responses of graphene, the FDTD method is chosen in the following chapters.

1.3 Objectives of the Thesis

The primary objectives of this thesis are presented as below:

1. Derive the formulation for FDTD modelling on the linear and nonlinear responses of graphene. Regarding the linear response of graphene, the existing FDTD modelling has taken into account the isotropic conductivity of graphene which is tunable by the gate voltage. The FDTD modelling can also be used for the anisotropic conductivity of graphene under magnetostatic bias. In this thesis, a new FDTD modelling on the anisotropic conductivity is implemented. Not only the transmission coefficient but also the polarisation variation are studied in the modelling method. Moreover, a novel FDTD modelling on the nonlinear response of graphene under strong EM radiation is proposed, which demonstrates the more accurate nonlinear phenomenon than existing FDTD modelling.

2. Explore the performance of graphene-based reflectors with magnetostatic tunability. The magnetostatic tunability of the graphene-based reflectors has not been reported in details under linearly polarised radiation at the room temperature. The proposed FDTD method models the full-wave performance of the reflector including the reflection coefficient and the Kerr rotation. Moreover, a modified equivalent circuit model is used to extract the parameters of graphene samples used in measurements.

3. Explore and design graphene-based reflectarray antennas. With the

consideration of free-space losses, the designs of graphene-based reflectarray antennas are explored at the spectrum with low atmosphere absorption. The unit-cell performance is simulated by proposed FDTD modelling methods. Their FDTD simulation results successfully demonstrate voltage-gate induced tunability in reflections which lead to tunable radiation patterns synthesised by traditional array theories.

1.4 Outline of the Thesis

The outline of the thesis is summarised as follows.

Chapter 2 covers the background of graphene including fabrication methods, electronic properties, linear/nonlinear response, graphene plasmonics and a brief introduction of some graphene-based THz devices.

Chapter 3 presents the FDTD modelling on linear response of graphene. The state-of-the-art is reviewed. An FDTD modelling based on the auxiliary element is proposed. FDTD results are compared with theoretical results and some measurement results.

Chapter 4 presents the FDTD modelling on nonlinear response of graphene. The state-of-the-art FDTD modelling on nonlinear materials is reviewed. An FDTD modelling based on a $J - E$ characteristic formula is proposed. FDTD results successfully demonstrate expected odd-harmonic generations and frequency-mixing effects.

Chapter 5 describes the modelling, fabrication and measurement of a magnetically tunable graphene-based reflector under linear polarised incidence at room temperature. The measured reflection intensity is presented and discussed. The variation of the polarised direction of EM waves is discussed according to full-wave simulations.

Chapter 6 describes the designs of graphene-based reflectarray antennas. Two designs respectively based on the graphene path array and the continuous graphene with metal metasurface are presented. The details of unit-cell design and tuneable radiation

patterns are also presented.

Chapter 7 presents the conclusion of the thesis and some thoughts for future work.

References

[1] S. L. Dexheimer, *Terahertz spectroscopy: principles and applications*. CRC press, 2007.

[2] C. K. Walker, *Terahertz astronomy*. CRC Press, 2015.

[3] J. F. Federici, B. Schulkin, F. Huang, D. Gary, R. Barat, F. Oliveira, and D. Zimdars, "THz imaging and sensing for security applications—explosives, weapons and drugs," *Semiconductor Science and Technology*, vol. 20, no. 7, p. S266, 2005.

[4] B. B. Hu and M. C. Nuss, "Imaging with terahertz waves," *Optics Letters*, vol. 20, no. 16, pp. 1716–1718, 1995.

[5] R. Piesiewicz, T. Kleine-Ostmann, N. Krumbholz, D. Mittleman, M. Koch, J. Schoebei, and T. Kurner, "Short-range ultra-broadband terahertz communications: Concepts and perspectives," *IEEE Antennas and Propagation Magazine*, vol. 49, no. 6, pp. 24–39, 2007.

[6] A. Redo-Sanchez and X.-C. Zhang, "Terahertz science and technology trends," *IEEE Journal of Selected Topics in Quantum Electronics*, vol. 14, no. 2, pp. 260–269, 2008.

[7] B. Ferguson and X.-C. Zhang, "Materials for terahertz science and technology," *Nature Materials*, vol. 1, no. 1, p. 26, 2002.

[8] M. Naftaly and R. E. Miles, "Terahertz time-domain spectroscopy for material characterization," *Proceedings of the IEEE*, vol. 95, no. 8, pp. 1658–1665, 2007.

[9] M. Walther, D. Cooke, C. Sherstan, M. Hajar, M. Freeman, and F. Hegmann, "Terahertz conductivity of thin gold films at the metal-insulator percolation transition," *Physical Review B*, vol. 76, no. 12, p. 125408, 2007.

[10] H. Yan, F. Xia, W. Zhu, M. Freitag, C. Dimitrakopoulos, A. A. Bol, G. Tulevski, and P. Avouris, "Infrared spectroscopy of wafer-scale graphene," *ACS Nano*, vol. 5, no. 12, pp. 9854–9860, 2011.

[11] A. Khandelwal, K. Mani, M. H. Karigerasi, and I. Lahiri, "Phosphorene – The two-dimensional black phosphorous: Properties, synthesis and applications," *Materials Science and Engineering B*, vol. 221, pp. 17–34, 2017.

[12] B. Peng, H. Zhang, H. Shao, Y. Xu, R. Zhang, and H. Zhu, "The electronic,

optical, and thermodynamic properties of borophene from first-principles calculations," *Journal of Materials Chemistry C*, vol. 4, no. 16, pp. 3592–3598, 2016.

[13] P. Vogt, P. De Padova, C. Quaresima, J. Avila, E. Frantzeskakis, M. C. Asensio, A. Resta, B. Ealet, and G. Le Lay, "Silicene: compelling experimental evidence for graphenelike two-dimensional silicon," *Physical Review Letters*, vol. 108, no. 15, p. 155501, 2012.

[14] C. J. Docherty, P. Parkinson, H. J. Joyce, M.-H. Chiu, C.-H. Chen, M.-Y. Lee, L.-J. Li, L. M. Herz, and M. B. Johnston, "Ultrafast transient terahertz conductivity of monolayer MoS_2 and WSe_2 grown by chemical vapor deposition," *ACS Nano*, vol. 8, no. 11, pp. 11 147–11 153, 2014.

[15] L. Ju, B. Geng, J. Horng, C. Girit, M. Martin, Z. Hao, H. A. Bechtel, X. Liang, A. Zettl, Y. R. Shen *et al.*, "Graphene plasmonics for tunable terahertz metamaterials," *Nature Nanotechnology*, vol. 6, no. 10, p. 630, 2011.

[16] C. Sirtori, "Applied physics: Bridge for the terahertz gap," *Nature*, vol. 417, no. 6885, pp. 132–133, 2002.

[17] G. P. Williams, "Filling the THz gap—high power sources and applications," *Reports on Progress in Physics*, vol. 69, no. 2, p. 301, 2005.

[18] Y.-C. Shen, "Terahertz pulsed spectroscopy and imaging for pharmaceutical applications: a review," *International Journal of Pharmaceutics*, vol. 417, no. 1-2, pp. 48–60, 2011.

[19] T. Kleine-Ostmann and T. Nagatsuma, "A review on terahertz communications research," *Journal of Infrared, Millimeter, and Terahertz Waves*, vol. 32, no. 2, pp. 143–171, 2011.

[20] A. Y. Pawar, D. D. Sonawane, K. B. Erande, and D. V. Derle, "Terahertz technology and its applications," *Drug Invention Today*, vol. 5, no. 2, pp. 157–163, 2013.

[21] A. R. Orlando and G. P. Gallerano, "Terahertz radiation effects and biological applications," *Journal of Infrared, Millimeter, and Terahertz Waves*, vol. 30, no. 12, pp. 1308–1318, 2009.

[22] P. H. Siegel, "Terahertz technology in biology and medicine," *IEEE Transactions on Microwave Theory and Techniques*, vol. 52, no. 10, pp. 2438–2447, 2004.

[23] J. Tong, M. Muthee, S.-Y. Chen, S. K. Yngvesson, and J. Yan, "Antenna enhanced graphene THz emitter and detector," *Nano Letters*, vol. 15, no. 8, pp. 5295–5301, 2015.

[24] X. Cai, A. B. Sushkov, R. J. Suess, M. M. Jadidi, G. S. Jenkins, L. O. Nyakiti, R. L. Myers-Ward, S. Li, J. Yan, D. K. Gaskill *et al.*, "Sensitive room-temperature terahertz detection via the photothermoelectric effect in graphene," *Nature Nanotechnology*, vol. 9, no. 10, p. 814, 2014.

[25] L. Vicarelli, M. Vitiello, D. Coquillat, A. Lombardo, A. Ferrari, W. Knap, M. Polini, V. Pellegrini, and A. Tredicucci, "Graphene field-effect transistors as room-temperature terahertz detectors," *Nature Materials*, vol. 11, no. 10, p. 865, 2012.

[26] S. Yamaguchi, Y. Fukushi, O. Kubota, T. Itsuji, T. Ouchi, and S. Yamamoto, "Brain tumor imaging of rat fresh tissue using terahertz spectroscopy," *Scientific Reports*, vol. 6, p. 30124, 2016.

[27] R. Woodward, B. Cole, V. Wallace, D. Arnone, R. Pye, E. Linfield, M. Pepper, and A. Davies, "Terahertz pulse imaging of in-vitro basal cell carcinoma samples," in *Conference on Lasers and Electro-Optics*. Optical Society of America, 2001, p. CWE4.

[28] D. Arnone, C. Ciesla, and M. Pepper, "Terahertz imaging comes into view," *Physics World*, vol. 13, no. 4, p. 35, 2000.

[29] H.-T. Chen, R. Kersting, and G. C. Cho, "Terahertz imaging with nanometer resolution," *Applied Physics Letters*, vol. 83, no. 15, pp. 3009–3011, 2003.

[30] K. Humphreys, J. Loughran, M. Gradziel, W. Lanigan, T. Ward, J. A. Murphy, and C. O'Sullivan, "Medical applications of terahertz imaging: a review of current technology and potential applications in biomedical engineering," in *The 26th Annual International Conference of the IEEE Engineering in Medicine and Biology Society*, vol. 1. IEEE, 2004, pp. 1302–1305.

[31] R. Appleby, "Passive millimetre–wave imaging and how it differs from terahertz imaging," *Philosophical Transactions of the Royal Society of London A: Mathematical, Physical and Engineering Sciences*, vol. 362, no. 1815, pp. 379–393, 2004.

[32] J. Federici and L. Moeller, "Review of terahertz and subterahertz wireless commu-

nications," *Journal of Applied Physics*, vol. 107, no. 11, p. 6, 2010.

[33] H.-J. Song, K. Ajito, A. Wakatsuki, Y. Muramoto, N. Kukutsu, Y. Kado, and T. Nagatsuma, "Terahertz wireless communication link at 300 GHz," in *IEEE Topical Meeting on Microwave Photonics (MWP)*. IEEE, 2010, pp. 42–45.

[34] S. Koenig, D. Lopez-Diaz, J. Antes, F. Boes, R. Henneberger, A. Leuther, A. Tessmann, R. Schmogrow, D. Hillerkuss, R. Palmer *et al.*, "Wireless sub-THz communication system with high data rate," *Nature Photonics*, vol. 7, no. 12, p. 977, 2013.

[35] R. N. Mitra and D. P. Agrawal, "5G mobile technology: A survey," *ICT Express*, vol. 1, no. 3, pp. 132–137, 2015.

[36] K.-C. Huang and Z. Wang, "Terahertz terabit wireless communication," *IEEE Microwave Magazine*, vol. 12, no. 4, pp. 108–116, 2011.

[37] I. F. Akyildiz, J. M. Jornet, and C. Han, "Terahertz band: Next frontier for wireless communications," *Physical Communication*, vol. 12, pp. 16–32, 2014.

[38] S. Abadal, E. Alarcón, A. Cabellos-Aparicio, M. Lemme, and M. Nemirovsky, "Graphene-enabled wireless communication for massive multicore architectures," *IEEE Communications Magazine*, vol. 51, no. 11, pp. 137–143, 2013.

[39] M. G. Larson and F. Bengzon, *The finite element method: theory, implementation, and applications*. Springer Science & Business Media, 2013, vol. 10.

[40] J.-M. Jin, *The finite element method in electromagnetics*. John Wiley & Sons, 2015.

[41] V. De La Rubia, U. Razafison, and Y. Maday, "Reliable fast frequency sweep for microwave devices via the reduced-basis method," *IEEE Transactions on Microwave Theory and Techniques*, vol. 57, no. 12, pp. 2923–2937, 2009.

[42] J.-M. Jin, M. Zunoubi, K. C. Donepudi, and W. C. Chew, "Frequency-domain and time-domain finite-element solution of Maxwell's equations using spectral lanczos decomposition method," *Computer Methods in Applied Mechanics and Engineering*, vol. 169, no. 3-4, pp. 279–296, 1999.

[43] J. M. Rius, E. Ubeda, and J. Parrón, "On the testing of the magnetic field integral equation with RWG basis functions in method of moments," *IEEE Transactions on*

Antennas and Propagation, vol. 49, no. 11, pp. 1550–1553, 2001.

[44] O. Alkhateeb and I. Tsukerman, "A boundary difference method for electromagnetic scattering problems with perfect conductors and corners," *IEEE Transactions on Antennas and Propagation*, vol. 61, no. 10, pp. 5117–5126, 2013.

[45] W. C. Gibson, *The method of moments in electromagnetics*. Chapman and Hall/CRC, 2007.

[46] S. Rao, D. Wilton, and A. Glisson, "Electromagnetic scattering by surfaces of arbitrary shape," *IEEE Transactions on Antennas and Propagation*, vol. 30, no. 3, pp. 409–418, 1982.

[47] A. Taflove and S. C. Hagness, *Computational electrodynamics*. Artech House, 2005.

[48] K. Yee, "Numerical solution of initial boundary value problems involving Maxwell's equations in isotropic media," *IEEE Transactions on Antennas and Propagation*, vol. 14, no. 3, pp. 302–307, 1966.

[49] G. G. O'Brien, M. A. Hyman, and S. Kaplan, "A study of the numerical solution of partial differential equations," *Journal of Mathematics and Physics*, vol. 29, no. 1-4, pp. 223–251, 1950.

[50] M. A. Alsunaidi and A. A. Al-Jabr, "A general ADE-FDTD algorithm for the simulation of dispersive structures," *IEEE Photonics Technology Letters*, vol. 21, no. 12, pp. 817–819, 2009.

[51] W. H. Weedon and C. M. Rappaport, "A general method for FDTD modeling of wave propagation in arbitrary frequency-dispersive media," *IEEE Transactions on Antennas and Propagation*, vol. 45, no. 3, pp. 401–410, 1997.

[52] R. M. Joseph and A. Taflove, "FDTD Maxwell's equations models for nonlinear electrodynamics and optics," *IEEE Transactions on Antennas and Propagation*, vol. 45, no. 3, pp. 364–374, 1997.

Chapter 2

Background of Graphene

In 2010, the Nobel Prize in physics was awarded to the breakthrough work on graphene [1] which is a two-dimensional (2D) carbon material consisting of a monolayer of carbon atoms tightly packed into a 2D honeycomb lattice [2]. However, the first experimentally discovered graphene is just on the scale of several sub-micrometre, and its homogeneity is poor [3]. Thus, efforts have been devoted to achieving fabrication methods for producing large-area and high-quality graphene [4]. Meanwhile, related methods of graphene characterisation, providing vivid images of graphene, have also been investigated [5].

The discovery of graphene boosts not only theoretical study but also experimental validations of its material properties [6]. As a semi-metal material, one of the attractive properties of graphene is its unique conductivity which can be controlled by external voltage bias [7] or magnetostatic bias [8]. Both the understanding of graphene features and the improved fabrication methods producing high-quality graphene provide opportunities for the arising of graphene-based devices which can manipulate electromagnetic (EM) waves at the THz spectrum [9].

This chapter provides the background of graphene which includes fabrication methods, electronic properties, linear responses, nonlinear responses and graphene plasmonics. Moreover, two kinds of graphene-based devices closely related with following chapters

are also introduced.

2.1 Fabrication Methods

The production approaches of graphene can be categorised into the top-down approach and the bottom-up approach (Figure 2.1) [10].

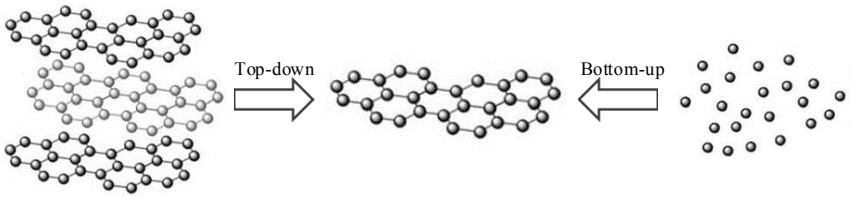

Figure 2.1: A schematic of the two production approaches of graphene. The top-down approach uses natural graphite to obtain graphene. And the bottom-up approach uses carbon atoms to synthesise graphene [10].

The top-down approach generally refers to the graphene preparation from bulk graphite, which is a natural carbon material consisting of stacked layers of graphene sheets [11]. Various exfoliation mechanisms can be utilised to overcome the van der Waals force between adjacent graphene sheets, such as mechanical exfoliation [12], electrochemical exfoliation [13], liquid-phase exfoliation [14], and exfoliation and reduction of graphite oxide [15]. Except for mechanical exfoliation, the other three kinds of exfoliation mechanisms suffer from not only small sample sizes but also uncontrolled quantity which has a significant impact on graphene properties. The bottom-up approach, mainly consisting of chemical vapour deposition and epitaxial growth, means the synthesis of graphene from alternative gases containing carbon atoms [16].

In this section, three approaches with the capability of producing high-quality graphene are introduced.

2.1.1 Mechanical Exfoliation

The discovery work of graphene in 2004 [3] makes the mechanical exfoliation method well-known in the world because it is this method that gave rise to the existence of graphene.

Its mechanical mechanism is to break the attraction force (i.e. the van der Waals force) between adjacent graphene sheets in natural graphite by using a nominal force. A schematic of mechanical exfoliation using Scotch tape to cleave a thin graphite flake is shown in Figure 2.2.

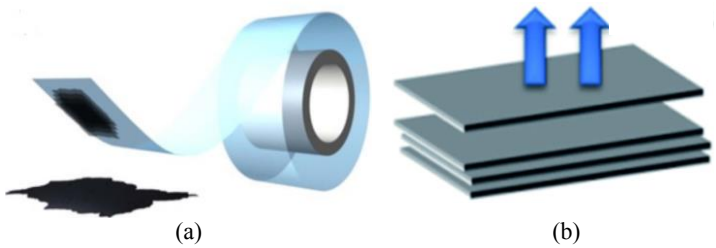

Figure 2.2: (a) A schematic of mechanical exfoliation using Scotch tapes to produce graphene (adapted from [17]). (b) Scotch tapes add forces on a thin graphite flake to cleave a graphene sheet (adapted from [12])

.

It is very difficult to obtain a one-atom-thick carbon material (i.e. graphene) from the initial exfoliation, with each subsequent exfoliation making the graphite flake thinner. Thus, the procedure will be repeated until a monolayer graphene is obtained. The unpredictability of the "Scotch tape" method makes it labour-intensive [18]. To save human labour, many researchers have proposed a home-designed exfoliation machine with electric motors [19]. However, the small size of graphene produced by mechanical exfoliation is a disadvantage for large-area applications.

2.1.2 Epitaxial Growth

Epitaxial growth can also synthesise large-area and good-quality graphene. Its schematic is shown in Figure 2.3.

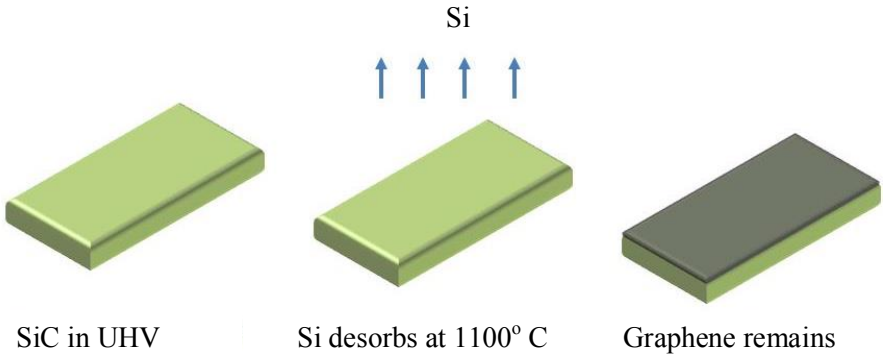

Figure 2.3: A schematic of epitaxial growth graphene using silicon carbide (adapted from [20]). Silicon atoms leave the surface of silicon carbide at high temperature in a vacuum environment. The left carbon atoms form graphene.

In epitaxial growth, the mainly used C-source material is silicon carbide (SiC) which is a semiconductor consisting of silicon atoms and carbon atoms. The mechanism of epitaxial growth can go back to the graphitisation of SiC in 1962 by sublimating Si atoms in a high-temperature vacuum environment [21]. A refined method has been proposed to grow graphene on the surface of SiC substrate at a high temperature (1100 °C) in ultra-high vacuum (UHV) [22]. The carbon atoms left on the SiC surface during the process of graphitisation form graphene. The produced graphene layer has a strong interaction with its SiC substrate which makes it difficult for transferring graphene to another substrate. Fortunately, SiC, as a good insulating material, can satisfy the requirement of some electronic devices or circuits. Moreover, it is noticed that SiC can have different microstructure. Thus, 4H-SiC [23] and 6H-SiC [24] are frequently used for graphene synthesis due to their similar hexagonal phase to the atom arrangement of graphene.

2.1.3 Chemical Vapour Deposition

Chemical vapour deposition (CVD) method has been successfully utilised for graphene synthesis since 2008 [25]. During the last decade, efforts have been made to improve its capability. Nowadays, CVD has been considered as the most popular method of large-area graphene synthesis at a relatively low price. Moreover, the synthesised graphene can be easily transferred to different substrates. A large amount of CVD graphene applications have emerged [26]. A schematic of CVD graphene is shown in Figure 2.4.

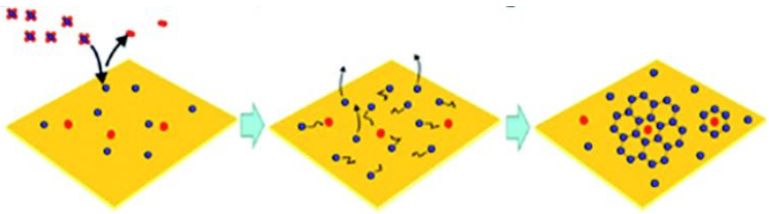

Figure 2.4: A schematic of CVD graphene. Carbon atoms decomposed from hydrocarbon gas form graphene on transition metals acting as substrates (adapted from [27]).

The CVD method firstly involves the decomposition of hydrocarbon gas, such as methane (CH_4), ethylene (C_2H_4) and acetylene (C_2H_2), over transition metals [26] [28]. The transition metals act as not only substrates but also catalysts that can reduce the temperature of the reactions [29]. For example, the temperature in thermal decomposition can be reduced from 1200 °C to 900 °C by using a copper substrate [30]. There are different options of transition metals such as nickel (Ni) [31], copper (Cu) [32], palladium (Pd) [33], ruthenium (Ru) [34], iridium (Ir) [35], platinum (Pt) [36] and cobalt (Co) [37]. Among these transition metals, Ni and Cu are low-cost metals adopted widely in CVD methods [26]. However, the growth mechanisms on Ni and Cu are different because the carbon solubility of Ni is much higher than Cu. It has been shown that only a small amount of carbon atoms are dissolved in Cu in high-concentration hydrocarbon gas with the long growth time [38].

The mechanism of Ni-based CVD is known as a segregation process [39]. In the

first step, Ni film is annealed at 900–1000 °C in protection atmosphere Ar/H_2. Then the carbon atoms decomposed from hydrocarbon gas are dissolved into Ni film which becomes a solid solution of carbon atoms. The Ni-C solid solution is cooled down in protection gas to diffuse carbon atoms out. Finally, diffused carbon atoms form graphene films on the surface of Ni substrate. Both the cooling rate and the defects in the Ni substrate can affect the quality of synthesised graphene. Defects can generate multilayer graphene on several micron sizes which reduces the homogeneity of monolayer graphene over the entire surface of Ni substrate.

In contrast to Ni-based CVD, Cu-based CVD, a surface reaction process, is different because the small number of dissolved carbon atoms in the Cu substrate can be ignored [40]. The surface of copper is usually oxidised, so the first step of Cu-based CVD is to remove the copper-oxide layer by annealing in a hydrogen atmosphere. The annealing process brings two benefits: the increased grain and reduced defects on the Cu surface. Then the decomposed carbon atoms form self-limiting mono-layer graphene islands over the surface of Cu substrate. As the increment of growth time, the size of graphene islands becomes larger, and eventually, the islands form a continuous graphene film. By controlling growth parameters, various shapes of graphene film such as hexagonal [41], rectangular [42] and flower shape [43] have been fabricated. However, the initial graphene islands have different lattice orientations. Moreover, the different thermal expansion coefficient of graphene islands and Cu can lead to the generation of wrinkles over the graphene films.

Among the three approaches introduced in this section, the CVD method would be the most suitable one for applications that require transferring large-area, good-quality graphene. In chapter 5, graphene-based reflectors with CVD graphene were measured and discussed at THz frequencies. Moreover, CVD graphene is also suitable for the potential fabrication of graphene-based reflectarray antennas discussed in chapter 6.

2.2 Electrons in Graphene

Ambipolar electric field effects of graphene indicate that graphene has two types of charge carriers: electrons (the n-type carrier) and holes (the p-type carrier) [44].

The carrier density of graphene can be tuned by changing the gate voltage applied to graphene. Except for the electrical doping through gate voltage, the carrier density can also be influenced by doping of chemical species which can be categorised into elemental doping and molecular doping [45]. In elemental doping, many carbons in graphene are substituted by nitrogen atoms and boron atoms which lead to n-type doped and p-type doped graphene respectively [46]. In molecular doping, the coverage of ammonia and water vapour leads to n-type doped and p-type doped graphene respectively [47, 48]. Moreover, it is noticed that experimental results of graphene with high charge carrier density $n > 10^{12}$ cm^{-2} can be well described as a system with a single carrier type [49].

This section mainly introduces the properties of electrons in graphene such as density, mobility and relaxation time.

2.2.1 Electron Density

Electrons in graphene behave like massless Dirac Fermions [50]. The Fermions include nano-scale particles characterised by their half-integer spin. Their distribution over energy levels in a system can be described by Fermi-Dirac distribution function (i.e. Fermi function) [51]

$$f_d(\varepsilon) = \left(e^{(\varepsilon-\mu_c)/k_BT} + 1\right)^{-1} \tag{2.1}$$

where ϵ is the energy level, T is the temperature, k_B is Boltzmann's constant and μ_c is the chemical potential which is a temperature-dependent variable. At absolute zero temperature ($T = 0$ K), the chemical potential is referred to as the Fermi level and no states above it are filled. At higher temperature, electrons gradually transit between completely filled states and completely empty states [52]. The result of Fermi func-

tion is the probability that an electron can occupy the energy level ϵ. The probability distributions of electrons at different temperatures are plotted in Figure 2.5.

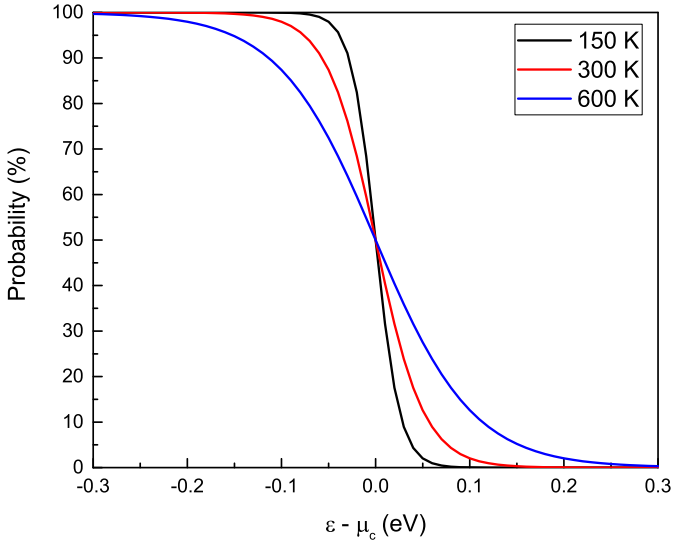

Figure 2.5: Fermi-Dirac distribution at temperature 150 K, 300 K and 600 K. With the increment of energy level ϵ, occupation probability of electrons decrease. The probability of electrons occupying the level of chemical potential is 50%.

From the viewpoint of energy levels, the electron density n of graphene can be calculated by the equation read as [53][54]

$$n = \frac{2}{\pi\hbar^2 v_F^2}\int_0^\infty \varepsilon[f_d(\varepsilon) - f_d(\varepsilon + 2\mu_c)]\mathrm{d}\varepsilon \tag{2.2}$$

where $v_F = 1.0 \times 10^6$ m/s is the Fermi velocity, $\hbar$ is the reduced Planck's constant, μ_c is the chemical potential, ϵ is the energy level of electrons and $f_d(\varepsilon)$ is Fermi-Dirac distribution function expressed as equation (2.1).

If the chemical potential is much larger than the thermal energy $|\mu_c| \gg k_B T$, equation (2.2) can be simplified as [55][56]

$$n = \frac{\mu_c}{\pi\hbar^2 v_F^2}. \tag{2.3}$$

The comparison of equation (2.2) and equation (2.3) is plotted in Figure 2.6, which demonstrates good agreement with each other at the room temperature.

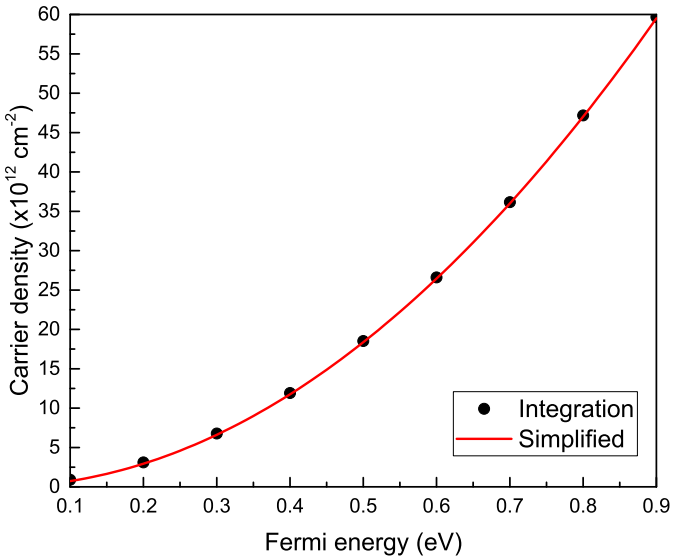

Figure 2.6: Carrier densities calculated by the integration equation (2.2) and its simplified equation (2.3) under the condition $|\mu_c| \gg k_B T$. At the room temperature 300 K ($k_B T = 0.0259$ eV), the results of two equations show good consistency.

When a gate voltage is applied to graphene, the density of gate-voltage induced electrons can be described by the equation read as [57]

$$n = C_{gate}(V_G - V_{CNP})/e \tag{2.4}$$

where $C_{gate} = \epsilon_{insulator}/t_{insulator}$ is the gate capacitance per unit area, $\epsilon_{insulator}$ is the permittivity of insulator, $t_{insulator}$ is the thickness of insulator beneath graphene, V_G is the applied gate voltage, V_{CNP} is the charge neutral point voltage and e is the charge of an electron. Note that V_{CNP} can be shifted away from zero gate voltage due to chemical doping [58]. With the assumption $V_{CNP} = 0$ V, the gate-voltage induced carrier densities of graphene on quartz and alumina insulators are shown in Figure 2.7. According to the experimental data in [50], the maximum gate voltage is chosen as 100 V in Figure 2.7.

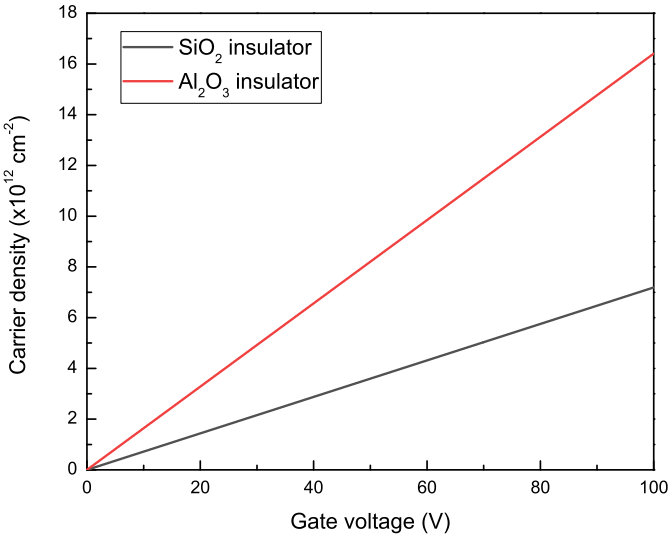

Figure 2.7: Carrier density induced by gate voltage. Graphene is treated as intrinsic with $V_{CNP} = 0$. The cases of quartz (SiO_2) insulator and alumina (Al_2O_3) insulator are plotted in the figure. The thickness of both insulator is set as 300 nm. The relative permittivity of SiO_2 (Al_2O_3) is 3.9 (8.9).

2.2.2 Electron Mobility

The electron mobility of graphene characterises how quickly an electron, pulled by an electric field, can move through a graphene sheet. The high carrier mobility of graphene has been considered as an advantage in transistor designs [59].

In suspended graphene, a mobility of $200,000$ cm^2(Vs)$^{-1}$ has been reported for low carrier densities 5×10^{11} cm^{-2} at low temperature [60, 61]. However, at the room temperature, the increased resistivity reduces the mobility to $120,000$ cm^2(Vs)$^{-1}$ [62]. The increased resistivity can also originate from the edge state of graphene ribbon [63] and metal contacts of voltage-gate structures [64, 65]. With considerations on resistivity and gate voltage, the molibity of graphene can be calculated as [57, 66]

$$\mu = \frac{1}{ne\rho} \tag{2.5}$$

where n is the gate-induced electron density expressed as equation (2.4) and ρ is the

electrical resistivity of graphene.

Moreover, substrates also have effects on the mobility of graphene [67]. For graphene sheets on SiO_2 substrates, electron scattering mechanisms further reduce the mobility to $40,000\ \mathrm{cm}^2(\mathrm{Vs})^{-1}$ [68]. In comparison to SiO_2, the mobility of graphene on hexagonal boron nitride (h-BN) substrate is an order of magnitude better [66, 69]. From the point view of scattering mechanisms, the mobility can also be given by [55, 70]

$$\mu = \frac{lev_F}{\mu_c} = \frac{e\tau v_F^2}{\mu_c} = \frac{ev_F^2}{\Gamma\mu_c} \tag{2.6}$$

where $l = v_F\tau$ is the distance of free path of electrons, $v_F = 1.0 \times 10^6$ m/s is the Fermi velocity, $\tau = 1/\Gamma$ is the relaxation time of electrons, Γ is the scattering rate of electrons and μ_c is the chemical potential.

2.2.3 Electron Relaxation Time

The relaxation time τ describes the time between two scattering events during the process of electron movement. It plays a fundamental role in studying graphene and its conductivity.

There are mainly three different scattering mechanisms in graphene, i.e. the longitudinal acoustic phonon scattering rate τ_{ac}^{-1}, the impurity scattering rate τ_{imp}^{-1} and the surface optical phonon scattering rate τ_{ph}^{-1} [71]. The total scattering rate, which is the inverse of the relaxation time τ, is written as

$$\tau^{-1} = \tau_{ac}^{-1} + \tau_{imp}^{-1} + \tau_{sp}^{-1}. \tag{2.7}$$

If $\mu_c \gg k_BT$, an effective relaxation time τ_{eff} measured from dc conductivity is a good approximation to fit experimental data [72, 73], which is also known as relaxation-time approximation (RTA) [74].

2.3 Linear Response of Graphene

The linear response of graphene can be characterised by its conductivity. When THz waves illuminate graphene, the effects of intraband transitions dominate conductivity, which follows the form of the Drude model. Moreover, graphene under magnetic bias exhibits the anisotropic conductivity expressed by a two-dimensional tensor. The details of related conductivity equations are provided in this section.

2.3.1 Isotropic Conductivity

Graphene's electronic band structure is shown in Figure 2.8 [75]. Its valence band and conduction band connect with each other. Only the electrons in its conduction band contribute to conductivity. When electromagnetic waves illuminate graphene, electrons absorb the energy of EM waves and transit from lower energy states to higher energy states. Thus, the conductivity of graphene has two contributions: intraband transitions and interband transitions.

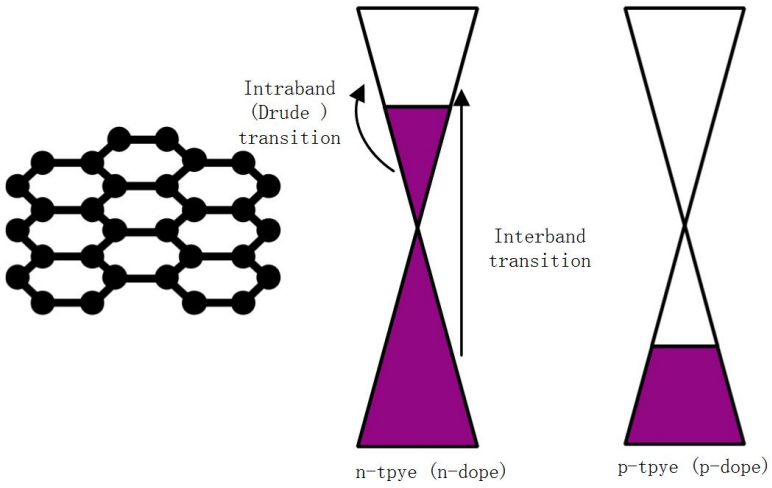

Figure 2.8: Band diagrams: n-type (n-dope) graphene with purple parts representing the energy levels occupied by electrons [75].

The conductivity of graphene can be calculated according to the Kubo formula, and

its equation is shown as below [54]

$$\sigma(\omega) = \frac{je^2(\omega - 2j\Gamma)}{\pi\hbar^2} \times \left[\frac{1}{(\omega - j2\Gamma)^2} \int_0^\infty \varepsilon \left(\frac{\partial f_d(\varepsilon)}{\partial \varepsilon} - \frac{\partial f_d(-\varepsilon)}{\partial \varepsilon} \right) d\varepsilon \right. \\ \left. - \int_0^\infty \frac{f_d(-\varepsilon) - f_d(\varepsilon)}{(\omega - j2\Gamma)^2 - 4(\varepsilon/\hbar)^2} d\varepsilon \right] \tag{2.8}$$

where the first term, named as intraband conductivity $\sigma(\omega)_{intra}$, is the results of intraband electron transitions and the second term, which originates from interband electron transitions, is named as interband conductivity $\sigma(\omega)_{inter}$.

The intraband conductivity follows the Drude model and can be expressed as

$$\sigma(\omega)_{intra} = -\frac{je^2 k_B T}{\pi\hbar^2(\omega - j2\Gamma)} \left(\frac{\mu_c}{k_B T} + 2\ln\left(e^{-\frac{\mu_c}{k_B T}} + 1\right) \right) \tag{2.9}$$

where e is the charge of an electron, k_B is the Boltzmann constant, $\hbar$ is the reduced Planck constant, T is temperature, μ_c is chemical potential and Γ is an effective scattering rate.

For $|\mu_c|, \hbar\omega \gg k_B T$, the interband conductivity can be approximated as

$$\sigma(\omega)_{inter} \cong -\frac{je^2}{4\pi\hbar} \ln\left(\frac{2|\mu_c| - (\omega - j2\Gamma)\hbar}{2|\mu_c| + (\omega - j2\Gamma)\hbar} \right). \tag{2.10}$$

The interband transition (i.e. electron transition from valence band to conduction band) cannot happen until the EM energy is larger than two-times chemical potential [76].

At terahertz (THz) frequencies, which range from 0.3 THz (1 mm) and 30 THz (10 μm) [77], the conductivity has a Drude-like frequency dependence [6]. The effects of interband electron transitions can be ignored for the graphene with typical values of chemical potential as shown in Figure 2.9.

Except for the Kubo formula, the intraband conductivity of graphene $\sigma(\omega)_{intra}$ can also be analysed by Boltzmann transport theories and expressed as [73]

$$\sigma(\omega)_{intra} = \frac{D}{\pi(j\omega + \Gamma)} = \frac{D\tau}{\pi(j\omega\tau + 1)} = \sigma_0 \frac{1}{1 + j\omega\tau} \tag{2.11}$$

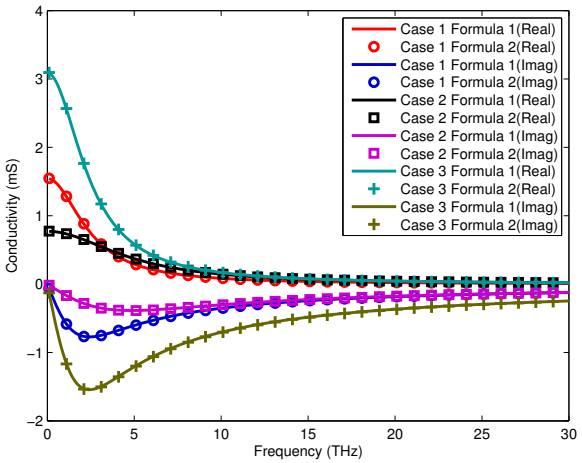

Figure 2.9: Linear conductivity of graphene. Formula 1 consider the effect interband transitions. Formula 2 does not consider the effect interband transitions. For all cases, $T = 300$ K; for the case 1, $\mu_c = 0.2$ eV, $\Gamma = 5$ meV; for the case 2, $\mu_c = 0.2$ eV, $\Gamma = 10$ meV; for the case 3, $\mu_c = 0.4$ eV, $\Gamma = 5$ meV.

where ω is the angular frequency, Γ is the scattering rate, $\tau = 1/\Gamma$ is the relaxation time, $D = (v_F e^2/\hbar)\sqrt{\pi|n|}$ is the Drude weight, $v_F = 1.0 \times 10^6$ m/s is the Fermi velocity, e is the charge of an electron, $\hbar$ is the reduced Plank's constant, n is the electron density and $\sigma_0 = D\tau/\pi$ is the dc conductivity.

The comparison between measured the dc conductivity σ_0 and the fitted Drude weight D of graphene can be found in [73]. Only the ratio of D and Γ can be determined from the dc conductivity. To know the value of D separately, the value of the carrier density n or the value of the chemical potential μ_c will be required. One of the methods to determine the value of μ_c is to measure the forbidden energy at infrared (IR) spectrum where interband electron transitions dominate.

2.3.2 Anisotropic Conductivity

When graphene is under magnetic bias, the conductivity of graphene can be described by a 2×2 tensor read as

$$\sigma = \begin{bmatrix} \sigma_{xx} & \sigma_{xy} \\ \sigma_{yx} & \sigma_{yy} \end{bmatrix} = \begin{bmatrix} \sigma_d & \sigma_o \\ -\sigma_o & \sigma_d \end{bmatrix}. \tag{2.12}$$

For THz, with the assumption $\mu_c \gg L$, where $L = v_F\sqrt{2\hbar e B_0}$ is the Landau level, electron transitions crossing the chemical potential μ_c have the highest possibilities and σ_{xx} and σ_{yx} follow the Drude model read as [78]

$$\sigma_{xx}(\omega, B_0) = \sigma_d = \sigma_0 \frac{1 + j\omega\tau}{(\omega_c\tau)^2 + (1 + j\omega\tau)^2} \tag{2.13}$$

$$\sigma_{yx}(\omega, B_0) = -\sigma_o = \sigma_0 \frac{\omega_c\tau}{(\omega_c\tau)^2 + (1 + j\omega\tau)^2} \tag{2.14}$$

where $\sigma_0 = \frac{2e^2\tau}{\pi\hbar^2} k_B T \ln\left(2\cosh\frac{\mu_c}{2k_BT}\right)$ is the dc conductivity, e is the charge of an electron, k_B is the Boltzmann constant, $\hbar$ is the reduced Planck constant, T is temperature, μ_c is chemical potential, τ is the relaxation time and

$$\omega_c \approx \frac{L^2}{2\hbar\mu_c} = \frac{eB_0 v_F^2}{\mu_c} \tag{2.15}$$

is the cyclotron frequency.

The electrons rotating at the cyclotron frequency ω_c will absorb the energy of external electromagnetic waves if $\omega \approx \omega_c$, where ω is the radiation frequency. The width of the cyclotron-resonance (CR) absorption line is usually determined by the scattering rate of electrons [79]. In the equation (2.15), ω_c has a directly proportional relation with the strength of magnetic bias B_0, but an inversely proportional relation with μ_c, which is shown in Figure 2.10.

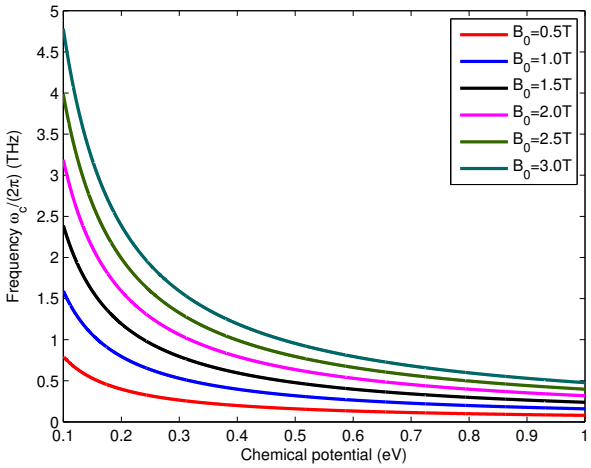

Figure 2.10: Cyclotron frequencies with different chemical potentials. The strength of magnetic bias B_0 is in a range from 0.5 T to 3.0 T

2.3.3 Faraday and Kerr Rotation

Faraday rotation (FR), discovered by Michael Faraday, is a physical phenomenon linking light and magnetism. He observed that the polarisation of light was rotated when a external magnetic field was induced in the same direction as the path of light. This phenomenon is known as the FR or Faraday effect, which originates from the cyclotron effect. Because polarisation is one of the fundamental properties of EM waves, the Faraday rotation has been observed at the THz spectrum. In addition, the Faraday effect can be considered as an analog of the dc Hall effect.

Under a static magnetic field, the off-diagonal conductivity of graphene σ_o, which has been expressed in equation (2.14), is non-zero [80]. Therefore, if THz radiation polarising in the x-direction illuminates this graphene, the polarisation of transmitted THz radiation will be rotated away from the x-direction, which is the FR of graphene, as shown in Figure 2.11. The change of the sign is because the FR angle is closely related to the real part of odd-diagonal conductivity σ_o, which changes the sign around the cyclotron frequency [81]. At the THz spectrum, the FR angle has been measured, which presents a positive sign at low frequencies and a negative sign at high frequencies [82].

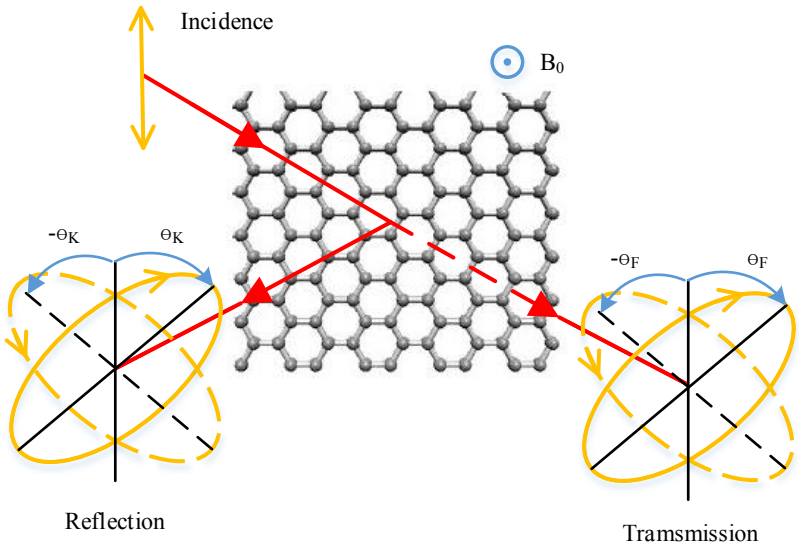

Figure 2.11: A schematic of the Faraday rotation angle θ_F and the Kerr rotation angle θ_K of graphene under magnetostaic bias B_0. Due to the Faraday (Kerr) effect, the linear polarisation of incidence becomes the elliptical polarisation of transmission (reflection). The rotation angle is defined as the angle between the polarisation direction of original incidence and the main axis of elliptical polarisation.

In addition, the polarisation is also rotated in reflected THz radiation from graphene under magnetostatic bias, which is known as the Kerr rotation (KR) of graphene [83], as shown in Figure 2.11. The measurement on KR of graphene also demonstrated that signs of the KR angle change at the THz spectrum [84]. The sign change is due to the fact that of the KR of graphene mainly depends on the real part of σ_o [85].

2.4 Non-linear Response of Graphene

At the illumination of strong THz waves, graphene exhibits nonlinear response. In this section, the origin of the nonlinearity of graphene is firstly introduced from the aspect of currents. Then, the conductivity of absorption saturation and the conductivity of third-harmonic generation are introduced. Finally, experimental work on the nonlinearity of graphene is summarised.

2.4.1 Theories on the Nonlinearity of Graphene

The energy band structure of graphene has a linear dispersion relation $\epsilon_p = v_F p$ near its Dirac points [86], which provides a qualitative understanding of the nonlinear nature in graphene. According to the Newton equation of motion $\mathrm{d}p/\mathrm{d}t = -eE_x(t)$ and the relation of velocity v and momentum p i.e. $v = \partial\epsilon_p/\partial p$, the induced ac current in graphene under the illumination of electric filed $E_x(t) = \cos\omega t$ can be expressed as [87]

$$\begin{aligned} j_x(t) &= en_s v_F \mathrm{sgn}(\sin\omega t) \\ &= en_s v_F \frac{4}{\pi}\left(\sin\omega t + \frac{1}{3}\sin 3\omega t + \frac{1}{5}\sin 5\omega t + \dots\right) \end{aligned} \tag{2.16}$$

where e is the charge of an electron, n_s is the density of electron and v_F is the Fermi velocity. It can be found out that the current $j_x(t)$ is a sign function with its expansion indicating the effects of frequency multiplication as shown in Figure 2.12. The expansion terms only consist of odd-harmonic generations because the centrosymmetric character of a flat graphene forbids the even-harmonic generations [88].

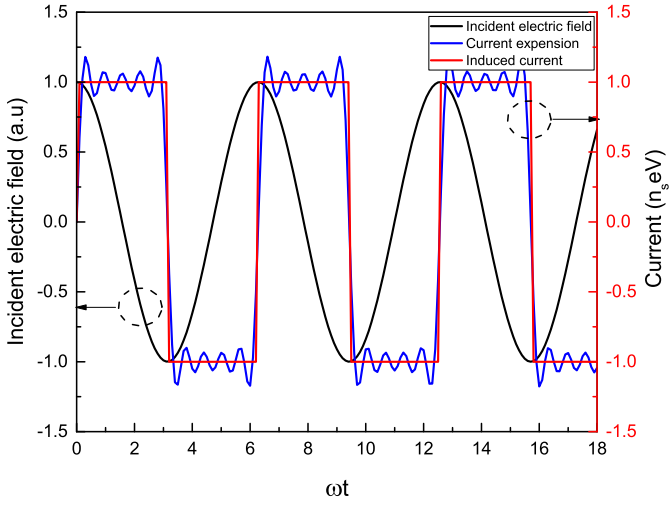

Figure 2.12: Qualitative understanding: Electric field, induced current and its expansion showing the odd-harmonic generation.

However, the simple qualitative understanding discussed above does not take into account the Fermi distribution of electrons in graphene. By using the kinetic Boltzmann

theory, an exact response of graphene with electrons at different energy levels can be expressed as [89]

$$j(t) = -\frac{g_s g_v e v_F}{(2\pi\hbar)} \int \frac{\mathbf{p}\mathrm{d}\mathbf{p}}{p} F_0\left(\mathbf{p} - \mathbf{p}_0(t)\right) \tag{2.17}$$

where $g_s = g_v = 2$ are the spin and valley degeneracies in graphene, v_F is Fermi velocity, $F_0(\mathbf{p}) = 1 + \exp\{[(Vp - \mu_c)/T]\}^{-1}$ is the Fermi-Driac function and p is momentum.

The nonlinearity of graphene originates from its surface currents which is different from traditional materials with nonlinear electric susceptibility $\chi^{(2)}$,$\chi^{(3)}$ describing the nonlinear response to EM waves. The nonlinearity of graphene can be characterised by its electric conductivity. The third-order conductivity of graphene with resonant behaviour at THz has been proposed in [90] to analyse various nonlinear phenomena. The nonlinear conductivity of graphene for the phenomenon of third-harmonic generation and absorption saturation is discussed below. Two dimensionless parameters are introduced

$$\Omega = \frac{\hbar\omega}{|\mu_c|}, \quad \gamma = \frac{\hbar\Gamma}{|\mu_c|}. \tag{2.18}$$

In terms of the third-harmonic generation, the induced current polarised in the x-direction, can be written as [90]

$$\begin{aligned} J_x^{(3)}(3\omega) &= \frac{1}{8} \times \sigma_{xxxx}^{(3)}(\omega,\omega,\omega) E_x^3(\omega) \\ &= \frac{1}{8} \times \sigma_0^{(3)} S_{xxxx}^{(3)}(\Omega,\Omega,\Omega) \times E_x^3(\omega) \end{aligned} \tag{2.19}$$

where $J_x^{(3)}(3\omega)$ is the induced third-order current in the unit of A/m, $E_x(\omega) = E_0 e^{j\omega t}$ is the illumination, $\sigma_{xxxx}^{(3)}(\omega,\omega,\omega) = \sigma_0^{(3)} S_{xxxx}^{(3)}(\Omega,\Omega,\Omega)$ is the intraband contribution from conductivity in the unit of $\mathrm{S{\cdot}m^2/V^2}$, $\sigma_0^{(3)} = (e^4\hbar v_F^2)/(4\pi\mu_c^4)$ and

$$S_{xxxx}^{(3)}(\Omega,\Omega,\Omega) = \frac{3}{(j\Omega+\gamma)(2j\Omega+\gamma)(3j\Omega+\gamma)} \tag{2.20}$$

is a third-order dimensionless conductivity as plotted in Figure 2.13

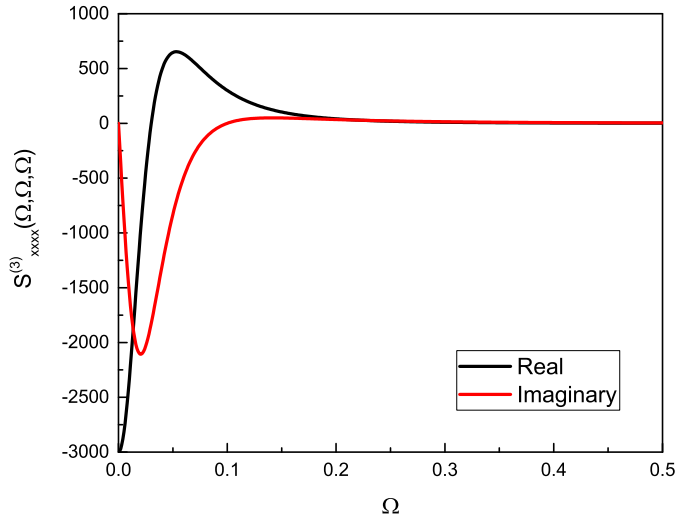

Figure 2.13: The intraband third-order dimensionless conductivity contributing to third-harmonic generations with $\gamma = 0.1$.

In terms of absorption saturation, the induced current at the frequency ω of incident wave $E_0 e^{j\omega t}$ can be expressed as [90]

$$\begin{aligned} J_x^{(3)}(\omega) &= \frac{1}{8}E_0^3\Big(\sigma_{xxxx}^{(3)}(\omega,\omega,-\omega)+\sigma_{xxxx}^{(3)}(\omega,-\omega,\omega)+\sigma_{xxxx}^{(3)}(-\omega,\omega,\omega)\Big)e^{j\omega t} \\ &= \frac{3}{8}E_0^3\sigma_0^{(3)}\Big(S_{xxxx}^{(3)}(\Omega,\Omega,-\Omega)+S_{xxxx}^{(3)}(\Omega,-\Omega,\Omega)+S_{xxxx}^{(3)}(-\Omega,\Omega,\Omega)\Big)e^{j\omega t} \end{aligned} \tag{2.21}$$

where the dimensionless conductivity $S_{xxxx}^{(3)}(\Omega,\Omega,-\Omega)$, $S_{xxxx}^{(3)}(\Omega,-\Omega,\Omega)$ and $S_{xxxx}^{(3)}(-\Omega,\Omega,\Omega)$ are expressed as

$$S_{xxxx}^{(3)}(\Omega,\Omega,-\Omega) = \frac{-1}{(j\Omega+\gamma)^2(2j\Omega+\gamma)} \quad , \tag{2.22a}$$

$$S_{xxxx}^{(3)}(\Omega,-\Omega,\Omega) = \frac{-1}{\gamma(j\Omega+\gamma)^2} \quad , \tag{2.22b}$$

$$S_{xxxx}^{(3)}(-\Omega,\Omega,\Omega) = \frac{-1}{\gamma(-j\Omega+\gamma)(j\Omega+\gamma)} \quad . \tag{2.22c}$$

The total effect of these three dimensionless conductivity is plotted in Figure 2.14

It has been predicted in [91] that a THz field with a peak value of 1 kV/cm is capable of inducing third-order harmonic generation (THG) on monolayer graphene at room temperature. Moveover, the strength of electric fields for graphene to exhibit

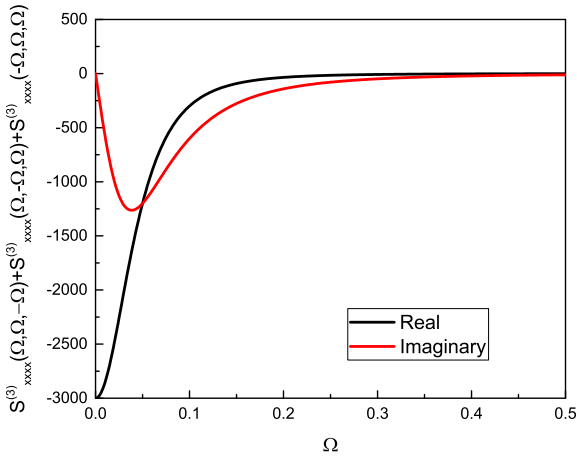

Figure 2.14: The intraband third-order dimensionless conductivity contributing to absorption saturation with $\gamma = 0.1$

nonlinearity depends on the carrier density of graphene:

$$E(\mathrm{V/cm}) \geq 300 \times n_s(10^{11}\mathrm{cm}^2), \tag{2.23}$$

which is plotted in Figure 2.15.

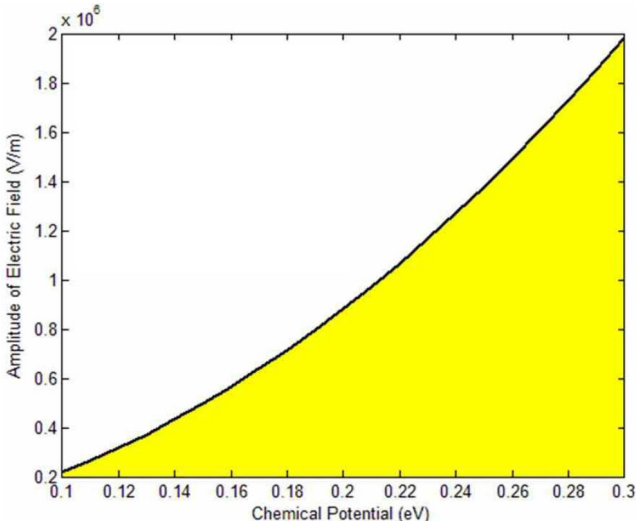

Figure 2.15: Requirement on electric field amplitude for various chemical potentials. In the yellow region, the amplitude is not high enough.

As shown in Figure 2.15, higher chemical potential requires larger electric field amplitude. The amplitude of generated third-order harmonic can be tuned by varying the

Fermi level of graphene with bias voltage [92]. To maximise the THG, the optimised relation between incident field amplitudes and Fermi levels has been discussed in [93]. Further enhancement can also be achieved by utilising appropriate graphene-dielectric-metal structures [94].

2.4.2 Experimental Observation of the Nonlinearity of Graphene

The development of strong THz sources has enabled experimental investigations on the nonlinearity of graphene. In recent years, THz field pulses with peak electric fields between 0.2 and 120 kV/cm have been used [95–102].

Experimental results have demonstrated that the CVD-grown graphene under the strong THz radiation has higher transmission compared to the graphene at lower field strength [95, 96]. It has been explained that the higher THz-induced transparency arises from the reduced conductivity due to saturable effects of current and increased intraband scattering rate in graphene [97]. The field-strength dependent behaviour indicates the existence of nonlinearity in graphene.

However, the carrier-carrier scattering limits harmonic generation in an experiment using the epitaxial multi-layer graphene [98]. With the considerations of scattering, it has been demonstrated that suspended graphene has stronger nonlinearity [99]. In other measurements, the odd-harmonic generation of graphene has been verified experimentally using a 45-layer graphene sample [100]. There are also observations on harmonic generations of graphene at millimetre wave range [101] and optical range [102].

2.5 Graphene Plasmonics

Surface plasmons are electromagnetic waves propagating along the boundary surface of a metal and a dielectric. The propagation of surface plasmons are accompanied by collective oscillations of surface charges in metals. The resembled oscillations, which

have been known as graphene plasmons, exist in the electrons confined on the surface of graphene [74]. At the THz spectrum, the unique electronic properties of graphene have made graphene plasmons different from the surface plasmons in metals and motivated a rapid progress in the field of graphene plasmonics [103].

Due to the mismatch on wavevector, free-space terahertz radiation cannot couple to plasmon excitations in homogeneous graphene sheets. In the experiments of graphene with natural nanoscale inhomogeneities, substrate terraces and wrinkles can generate intrinsic graphene plasmons [104]. However, graphene plasmon resonances originating from the nanoscale inhomogeneities cannot be tuned over a broad terahertz frequency range. To tackle this issue, engineered graphene structures in sub-wavelength have been used, such as patterned graphene and continuous graphene with grating structures.

2.5.1 Patterned Graphene

Experiments have demonstrated that THz radiation can strongly couple to plasmons in patterned graphene [105–110].

Graphene ribbons, as the simplest form of engineered graphene structure, were initially proposed in 2011 to excite graphene plasmons at the THz frequencies [105]. The experiments demonstrated that plasmon excitations of graphene ribbons can be controlled through changing ribbon width and electrostatic doping. The enhanced THz absorption indicates the strong coupling between terahertz radiation and graphene plasmons. By cutting the ribbons, an optimised geometry of graphene cut-wires has shown an enhancement of up to 50% in the absorption of THz radiation [106].

Other geometries, such as graphene disks [107], graphene anti-dots [108] and graphene rings [109], have also been investigated. Compared to graphene disks, the resonance frequencies of graphene anti-dots can be more easily tuned by the gate voltage [108]. Moreover, graphene rings have demonstrated two plasmon modes because each graphene ring consists of a graphene disc and a smaller graphene anti-dot. In addition, two plasmon

modes have also be observed from graphene disks under magnetostatic bias where the plasmon modes are split into an edge mode and a bulk mode [110].

According to the above experimental work, the frequencies of plasmon modes of patterned graphene can be tuned by changing the aspects followed as (i) the geometry of engineered graphene structure, (ii) the value of gate voltage and (iii) the strength of magnetostatic bias.

2.5.2 Continuous Graphene with Grating Structure

Grating structures, which have been widely used in optics to compensate wavevector mismatches, have also been adopted to excite plasmonics in continuous graphene. Different from plasmonic oscillations bounded by patterned graphene, a continuous graphene with grating structures can support the propagation of plasmonic waves.

Theoretical analysis has shown that the periodic silicon diffractive grating structure in a square-wave shape can excite the highly confined plasmonic waves in monolayer graphene films [111]. The resonant frequency is mainly determined by the period of the grating. As the period decreases, the resonant frequency shifts to higher frequencies. Further experimental work not only confirmed the theoretical analysis but also demonstrated that the surface plasmon polaritons (SPPs) propagating through monolayer graphene can be tuned by applying a gate voltage [112]. To apply the gate voltage, a dielectric spacer was deposited between the graphene layer and silicon diffractive grating structure. However, the square-wave shaped grating is a one-dimensional structure, therefore only the electric field polarising in the direction perpendicular to the grating lines can achieve the phase-matching effect [113].

Except for dielectric grating structures, the grating structures made of metal, such as gold and silver, have also been investigated. The comparison between dielectric grating and metallic grating has shown that the height of metallic grating has less effect on SPPs than the height of dielectric grating because the EM waves penetrate more into

the dielectric grating [114]. For metal–graphene plasmon resonance, the width of metallic grating is the main effect on resonance frequency [115].

2.6 Graphene-based THz Devices

The interesting properties of graphene have been adopted for various graphene devices. In this section, two kinds of graphene-based devices, which are closely related with the thesis, are introduced on their recent years' development.

2.6.1 Graphene-based Salisbury Screen

Salisbury screen, which is a sandwich structure consisting of a resistive sheet, a dielectric layer and a ground plane, can be used to control the reflection of electromagnetic waves from conducting material [116]. There is a 180° phase difference in incident waves and reflected waves, so they cancel each other to obtain absorption performance. The absorption spectrum depends on the thickness of the substrate, which makes it a single-band absorber. Graphene has been used as the resistive sheet of Salisbury screen at the THz spectrum [117]. Its figure-of-merit includes absorption efficiency, bandwidth, sensitivity to polarisation and bandwidth.

In order to achieve multi-band absorption, stacked multi-layer structures can be used [118]. The similar principle has been adopted in a multi-layer graphene-based absorber [119]. However, its thickness is increased. Except for continuous graphene, designs based on graphene metasurface can obtain broadband absorption by exciting resonance modes [120–122]. Plasmonic resonance modes can also be excited in hybrid graphene-metal structures [123, 124] and also in graphene ribbons [125]. Its absorption performance can also be explained from the aspect of impedance match of circuit models [126]. Metamaterials have been used as substrates for the impedance match [127, 128].

When magnetostatic bias is applied to graphene, the anisotropic conductivity of

graphene provides nonreciprocal features which make the device sensitive to right-hand and left-hand polarised waves [129]. Fundamental limits of some special cases have been proposed in [130]. Later a near optimal non-reciprocal isolator has been demonstrated [84]. The anisotropic response actually is the results of the Faraday effect in graphene. However, its effect is more obvious at the low THz spectrum. By using metasurface, the Faraday effect at the higher THz can be enhanced and reduce the requirement of the strength of magnetostatic bias [131].

2.6.2 Graphene-based Antenna

An antenna is a transitional structure between electromagnetic waves propagating in free space and currents oscillating in materials. It can be used to radiate or receive EM waves. In history, the first antenna was demonstrated by Heinrich Hertz in 1888 [132]. During the development of more than a century, the antenna has become a specific research field, and various antenna types have been proposed. According to their geometrical characteristic, antennas can be classified into wire antennas, aperture antennas, microstrip antennas, array antennas, reflector antennas and lens antennas [133]. Each type of antenna has its radiation characteristics. However, there are many common parameters used as figure-of-merit such as directivity, gain, bandwidth and radiation efficiency [134]. In recent years, graphene has been considered as a promising material in antenna investigation [135].

Surface plasmon polariton (SPP) waves, confined EM waves, have been theoretically and experimentally proved its existence in graphene [105, 136]. This fact inspires the researchers to bring the concept of plasmonic antennas used in optics [137, 138] to graphene application at the THz spectrum [139]. The SPP modes of graphene patch antennas have been analytically studied which demonstrate the capability on antenna minimisation [140]. The termination of graphene patch antenna works as mirrors for SPP waves, which means that the resonance behaviour in scattered waves can be described by Fabry–Pérot model [141]. When graphene patch is coupled with a well-matched feeding

line (i.e. very small return loss), the radiation efficiency is as low as 15% due to the dissipation losses of graphene [142]. The challenge of low radiation efficiency also occurs in other antenna designs such as the dipole antenna with 10% radiation efficiency [143, 144] and a leaky-wave antenna with about 15% radiation efficiency [145]. However, electronic beam scanning of the leaky wave antenna is a potential advantage [145]. The balance between radiation efficiency and tunability need to be considered for these graphene-based plasmonic resonance antenna [146, 147]. It is noticed that their metal counterparts also face the issue of radiation efficiency of electrically small antennas [148]. Minimised metal-graphene hybrid antennas have been demonstrated with 10% radiation efficiency [149, 150].

Another exciting type of antennas is a reflectarray antenna. The reflectarray antenna is a device using the phase distribution to reform the radiation source to be the desired beam in the far field. Graphene-based unit cells have been proposed to provide the phase distribution [151]. The phase variation of unit cells is the achieved by tuning the complex conductivity of graphene. The performance of graphene-based reflectarray has demonstrated a similar gain to its gold counterpart [152]. Except for graphene with particular geometries, arrays of metal antennas deposited on a graphene sheet have been demonstrated working in an ON or OFF state [153].

2.7 Summary

In the last decade, the requirements on large-area and high-quality graphene have motivated researchers to improve the production approaches of graphene. Mechanical exfoliation, chemical vapour deposition and epitaxial growth have demonstrated outstanding performance among various production approaches. Benefiting from the development of graphene fabrication, THz devices manipulating electromagnetic waves have begun to take the advantages of the peculiar conductivity of graphene which can be controlled by electrostatic bias and magnetostatic bias. The properties of electrons such as carrier

density, mobility and relaxation time can affect graphene's conductivity. At the THz spectrum, graphene's linear conductivity can be described by the Drude model. The carrier density determines the Drude weight and the relaxation time influences the value of the Durde peak. The carrier mobility as a parameter linking the carrier density and relaxation time indicates the quality of graphene. Under the illumination of strong THz waves, the carrier density and relaxation time also decide graphene's nonlinear responses such as the absorption saturation and the third-harmonic generation.

References

[1] Y. Hancock, "The 2010 nobel prize in physics—ground-breaking experiments on graphene," *Journal of Physics D: Applied Physics*, vol. 44, no. 47, p. 473001, 2011.

[2] A. K. Geim and K. S. Novoselov, "The rise of graphene," *Nature Materials*, vol. 6, no. 3, pp. 183–191, 2007.

[3] K. S. Novoselov, A. K. Geim, S. V. Morozov, D. Jiang, Y. Zhang, S. V. Dubonos, I. V. Grigorieva, and A. A. Firsov, "Electric field effect in atomically thin carbon films," *Science*, vol. 306, no. 5696, pp. 666–669, 2004.

[4] M. J. Allen, V. C. Tung, and R. B. Kaner, "Honeycomb carbon: a review of graphene," *Chemical Reviews*, vol. 110, no. 1, pp. 132–145, 2009.

[5] V. Skákalová and A. B. Kaiser, *Graphene: properties, preparation, characterisation and devices*. Elsevier, 2014.

[6] A. C. Neto, F. Guinea, N. M. Peres, K. S. Novoselov, and A. K. Geim, "The electronic properties of graphene," *Reviews of Modern Physics*, vol. 81, no. 1, p. 109, 2009.

[7] Z. Fei, A. Rodin, G. Andreev, W. Bao, A. McLeod, M. Wagner, L. Zhang, Z. Zhao, M. Thiemens, G. Dominguez *et al.*, "Gate-tuning of graphene plasmons revealed by infrared nano-imaging," *Nature*, vol. 487, no. 7405, p. 82, 2012.

[8] V. Gusynin and S. Sharapov, "Unconventional integer quantum hall effect in graphene," *Physical Review Letters*, vol. 95, no. 14, p. 146801, 2005.

[9] T. Otsuji, S. B. Tombet, A. Satou, H. Fukidome, M. Suemitsu, E. Sano, V. Popov, M. Ryzhii, and V. Ryzhii, "Graphene-based devices in terahertz science and technology," *Journal of Physics D: Applied Physics*, vol. 45, no. 30, p. 303001, 2012.

[10] R. S. Edwards and K. S. Coleman, "Graphene synthesis: relationship to applications," *Nanoscale*, vol. 5, no. 1, pp. 38–51, 2013.

[11] J. M. Tour, "Top-down versus bottom-up fabrication of graphene-based electronics," *Chemistry of Materials*, vol. 26, no. 1, pp. 163–171, 2013.

[12] M. Yi and Z. Shen, "A review on mechanical exfoliation for the scalable production of graphene," *Journal of Materials Chemistry A*, vol. 3, no. 22, pp. 11 700–11 715,

2015.

[13] C.-Y. Su, A.-Y. Lu, Y. Xu, F.-R. Chen, A. N. Khlobystov, and L.-J. Li, "High-quality thin graphene films from fast electrochemical exfoliation," *ACS Nano*, vol. 5, no. 3, pp. 2332–2339, 2011.

[14] K. R. Paton, E. Varrla, C. Backes, R. J. Smith, U. Khan, A. O'Neill, C. Boland, M. Lotya, O. M. Istrate, P. King *et al.*, "Scalable production of large quantities of defect-free few-layer graphene by shear exfoliation in liquids," *Nature Materials*, vol. 13, no. 6, p. 624, 2014.

[15] J. H. Lee, D. W. Shin, V. G. Makotchenko, A. S. Nazarov, V. E. Fedorov, Y. H. Kim, J.-Y. Choi, J. M. Kim, and J.-B. Yoo, "One-step exfoliation synthesis of easily soluble graphite and transparent conducting graphene sheets," *Advanced Materials*, vol. 21, no. 43, pp. 4383–4387, 2009.

[16] C. K. G. Sunipa Roy and C. K. Sarkar, *Nanotechnology: Synthesis to Applications*. CRC Press, 2017.

[17] K. Novoselov and A. C. Neto, "Two-dimensional crystals-based heterostructures: materials with tailored properties," *Physica Scripta*, vol. 2012, no. T146, p. 014006, 2012.

[18] M. A. Rafiee, J. Rafiee, Z. Wang, H. Song, Z.-Z. Yu, and N. Koratkar, "Enhanced mechanical properties of nanocomposites at low graphene content," *ACS Nano*, vol. 3, no. 12, pp. 3884–3890, 2009.

[19] L. Yuan, J. Ge, X. Peng, Q. Zhang, Z. Wu, Y. Jian, X. Xiong, H. Yin, and J. Han, "A reliable way of mechanical exfoliation of large scale two dimensional materials with high quality," *AIP Advances*, vol. 6, no. 12, p. 125201, 2016.

[20] "Interfaces with epitaxial graphene," https://sites.google.com/site/doughertydaniel/interfaces-with-epitaxial-graphene, accessed: 2018-09-11.

[21] D. Badami, "Graphitization of α-silicon carbide," *Nature*, vol. 193, no. 4815, p. 569, 1962.

[22] P. Sutter, "Epitaxial graphene: How silicon leaves the scene," *Nature Materials*, vol. 8, no. 3, p. 171, 2009.

[23] G. Prakash, M. A. Capano, M. L. Bolen, D. Zemlyanov, and R. G. Reifenberger,

"AFM study of ridges in few-layer epitaxial graphene grown on the carbon-face of 4H–SiC (0001)," *Carbon*, vol. 48, no. 9, pp. 2383–2393, 2010.

[24] N. Camara, J.-R. Huntzinger, G. Rius, A. Tiberj, N. Mestres, F. Pérez-Murano, P. Godignon, and J. Camassel, "Anisotropic growth of long isolated graphene ribbons on the C face of graphite-capped 6H-SiC," *Physical Review B*, vol. 80, no. 12, p. 125410, 2009.

[25] Q. Yu, J. Lian, S. Siriponglert, H. Li, Y. P. Chen, and S.-S. Pei, "Graphene segregated on ni surfaces and transferred to insulators," *Applied Physics Letters*, vol. 93, no. 11, p. 113103, 2008.

[26] Y. Zhang, L. Zhang, and C. Zhou, "Review of chemical vapor deposition of graphene and related applications," *Accounts of Chemical Research*, vol. 46, no. 10, pp. 2329–2339, 2013.

[27] J. Yu, J. Li, W. Zhang, and H. Chang, "Synthesis of high quality two-dimensional materials via chemical vapor deposition," *Chemical Science*, vol. 6, no. 12, pp. 6705–6716, 2015.

[28] A. N. Obraztsov, "Chemical vapour deposition: making graphene on a large scale," *Nature Nanotechnology*, vol. 4, no. 4, p. 212, 2009.

[29] C.-M. Seah, S.-P. Chai, and A. R. Mohamed, "Mechanisms of graphene growth by chemical vapour deposition on transition metals," *Carbon*, vol. 70, pp. 1–21, 2014.

[30] R. Muñoz and C. Gómez-Aleixandre, "Review of CVD synthesis of graphene," *Chemical Vapor Deposition*, vol. 19, no. 10-11-12, pp. 297–322, 2013.

[31] K. S. Kim, Y. Zhao, H. Jang, S. Y. Lee, J. M. Kim, K. S. Kim, J.-H. Ahn, P. Kim, J.-Y. Choi, and B. H. Hong, "Large-scale pattern growth of graphene films for stretchable transparent electrodes," *Nature*, vol. 457, no. 7230, p. 706, 2009.

[32] X. Li, W. Cai, J. An, S. Kim, J. Nah, D. Yang, R. Piner, A. Velamakanni, I. Jung, E. Tutuc *et al.*, "Large-area synthesis of high-quality and uniform graphene films on copper foils," *Science*, vol. 324, no. 5932, pp. 1312–1314, 2009.

[33] S.-Y. Kwon, C. V. Ciobanu, V. Petrova, V. B. Shenoy, J. Bareno, V. Gambin, I. Petrov, and S. Kodambaka, "Growth of semiconducting graphene on palladium," *Nano Letters*, vol. 9, no. 12, pp. 3985–3990, 2009.

[34] P. W. Sutter, J.-I. Flege, and E. A. Sutter, "Epitaxial graphene on ruthenium," *Nature Materials*, vol. 7, no. 5, p. 406, 2008.

[35] J. Coraux, A. T. N 'Diaye, C. Busse, and T. Michely, "Structural coherency of graphene on Ir (111)," *Nano Letters*, vol. 8, no. 2, pp. 565–570, 2008.

[36] P. Sutter, J. T. Sadowski, and E. Sutter, "Graphene on Pt (111): Growth and substrate interaction," *Physical Review B*, vol. 80, no. 24, p. 245411, 2009.

[37] A. Varykhalov and O. Rader, "Graphene grown on Co (0001) films and islands: Electronic structure and its precise magnetization dependence," *Physical Review B*, vol. 80, no. 3, p. 035437, 2009.

[38] S. Chen, H. Ji, H. Chou, Q. Li, H. Li, J. W. Suk, R. Piner, L. Liao, W. Cai, and R. S. Ruoff, "Millimeter-size single-crystal graphene by suppressing evaporative loss of Cu during low pressure chemical vapor deposition," *Advanced Materials*, vol. 25, no. 14, pp. 2062–2065, 2013.

[39] X. Li, W. Cai, L. Colombo, and R. S. Ruoff, "Evolution of graphene growth on Ni and Cu by carbon isotope labeling," *Nano Letters*, vol. 9, no. 12, pp. 4268–4272, 2009.

[40] C. Mattevi, H. Kim, and M. Chhowalla, "A review of chemical vapour deposition of graphene on copper," *Journal of Materials Chemistry*, vol. 21, no. 10, pp. 3324–3334, 2011.

[41] Z. Yan, J. Lin, Z. Peng, Z. Sun, Y. Zhu, L. Li, C. Xiang, E. L. Samuel, C. Kittrell, and J. M. Tour, "Toward the synthesis of wafer-scale single-crystal graphene on copper foils," *ACS Nano*, vol. 6, no. 10, pp. 9110–9117, 2012.

[42] H. Wang, G. Wang, P. Bao, S. Yang, W. Zhu, X. Xie, and W.-J. Zhang, "Controllable synthesis of submillimeter single-crystal monolayer graphene domains on copper foils by suppressing nucleation," *Journal of the American Chemical Society*, vol. 134, no. 8, pp. 3627–3630, 2012.

[43] Y. Zhang, L. Zhang, P. Kim, M. Ge, Z. Li, and C. Zhou, "Vapor trapping growth of single-crystalline graphene flowers: synthesis, morphology, and electronic properties," *Nano Letters*, vol. 12, no. 6, pp. 2810–2816, 2012.

[44] A. K. Geim and K. S. Novoselov, "The rise of graphene," in *Nanoscience and*

Technology: A Collection of Reviews from Nature Journals. World Scientific, 2010, pp. 11–19.

[45] H. Liu, Y. Liu, and D. Zhu, "Chemical doping of graphene," *Journal of Materials Chemistry*, vol. 21, no. 10, pp. 3335–3345, 2011.

[46] L. Panchakarla, K. Subrahmanyam, S. Saha, A. Govindaraj, H. Krishnamurthy, U. Waghmare, and C. Rao, "Synthesis, structure, and properties of boron-and nitrogen-doped graphene," *Advanced Materials*, vol. 21, no. 46, pp. 4726–4730, 2009.

[47] Q. Su, S. Pang, V. Alijani, C. Li, X. Feng, and K. Müllen, "Composites of graphene with large aromatic molecules," *Advanced Materials*, vol. 21, no. 31, pp. 3191–3195, 2009.

[48] B. Das, R. Voggu, C. S. Rout, and C. Rao, "Changes in the electronic structure and properties of graphene induced by molecular charge-transfer," *Chemical Communications*, no. 41, pp. 5155–5157, 2008.

[49] S. Dushenko, H. Ago, K. Kawahara, T. Tsuda, S. Kuwabata, T. Takenobu, T. Shinjo, Y. Ando, and M. Shiraishi, "Gate-tunable spin-charge conversion and the role of spin-orbit interaction in graphene," *Physical Review Letters*, vol. 116, no. 16, p. 166102, 2016.

[50] K. S. Novoselov, A. K. Geim, S. Morozov, D. Jiang, M. Katsnelson, I. Grigorieva, S. Dubonos, Firsov, and AA, "Two-dimensional gas of massless dirac fermions in graphene," *Nature*, vol. 438, no. 7065, p. 197, 2005.

[51] A. L. Wasserman, *Thermal physics: concepts and practice.* Cambridge University Press, 2011.

[52] S. Panda, *Microelectronics and optoelectronics technology.* Laxmi Publications, 2009.

[53] L. Falkovsky, "Unusual field and temperature dependence of the hall effect in graphene," *Physical Review B*, vol. 75, no. 3, p. 033409, 2007.

[54] G. W. Hanson, "Dyadic green's functions for an anisotropic, non-local model of biased graphene," *IEEE Transactions on Antennas and Propagation*, vol. 56, no. 3, pp. 747–757, 2008.

[55] D. L. Sounas and C. Caloz, "Gyrotropy and nonreciprocity of graphene for microwave applications," *IEEE Transactions on Microwave Theory and Techniques*, vol. 60, no. 4, pp. 901–914, 2012.

[56] H. Dong, C. Conti, A. Marini, and F. Biancalana, "Terahertz relativistic spatial solitons in doped graphene metamaterials," *Journal of Physics B: Atomic, Molecular and Optical Physics*, vol. 46, no. 15, p. 155401, 2013.

[57] N. K. Emani, A. V. Kildishev, V. M. Shalaev, and A. Boltasseva, "Graphene: a dynamic platform for electrical control of plasmonic resonance," *Nanophotonics*, vol. 4, no. 1, pp. 214–223, 2015.

[58] N. E. Staley, C. P. Puls, and Y. Liu, "Suppression of conductance fluctuation in weakly disordered mesoscopic graphene samples near the charge neutral point," *Physical Review B*, vol. 77, no. 15, p. 155429, 2008.

[59] F. Schwierz, "Graphene transistors," *Nature Nanotechnology*, vol. 5, no. 7, p. 487, 2010.

[60] K. I. Bolotin, K. Sikes, Z. Jiang, M. Klima, G. Fudenberg, J. Hone, P. Kim, and H. Stormer, "Ultrahigh electron mobility in suspended graphene," *Solid State Communications*, vol. 146, no. 9-10, pp. 351–355, 2008.

[61] X. Du, I. Skachko, A. Barker, and E. Y. Andrei, "Approaching ballistic transport in suspended graphene," *Nature Nanotechnology*, vol. 3, no. 8, p. 491, 2008.

[62] E. V. Castro, H. Ochoa, M. Katsnelson, R. Gorbachev, D. Elias, K. Novoselov, A. Geim, and F. Guinea, "Limits on charge carrier mobility in suspended graphene due to flexural phonons," *Physical Review Letters*, vol. 105, no. 26, p. 266601, 2010.

[63] Z. Chen, Y.-M. Lin, M. J. Rooks, and P. Avouris, "Graphene nano-ribbon electronics," *Physica E: Low-dimensional Systems and Nanostructures*, vol. 40, no. 2, pp. 228–232, 2007.

[64] D. B. Farmer, H.-Y. Chiu, Y.-M. Lin, K. A. Jenkins, F. Xia, and P. Avouris, "Utilization of a buffered dielectric to achieve high field-effect carrier mobility in graphene transistors," *Nano Letters*, vol. 9, no. 12, pp. 4474–4478, 2009.

[65] S. Kim, J. Nah, I. Jo, D. Shahrjerdi, L. Colombo, Z. Yao, E. Tutuc, and S. K. Banerjee, "Realization of a high mobility dual-gated graphene field-effect transistor

with Al_2O_3 dielectric," *Applied Physics Letters*, vol. 94, no. 6, p. 062107, 2009.

[66] P. Zomer, S. Dash, N. Tombros, and B. Van Wees, "A transfer technique for high mobility graphene devices on commercially available hexagonal boron nitride," *Applied Physics Letters*, vol. 99, no. 23, p. 232104, 2011.

[67] L. Ponomarenko, R. Yang, T. Mohiuddin, M. Katsnelson, K. Novoselov, S. Morozov, A. Zhukov, F. Schedin, E. Hill, and A. Geim, "Effect of a high-κ environment on charge carrier mobility in graphene," *Physical Review Letters*, vol. 102, no. 20, p. 206603, 2009.

[68] J.-H. Chen, C. Jang, S. Xiao, M. Ishigami, and M. S. Fuhrer, "Intrinsic and extrinsic performance limits of graphene devices on SiO_2," *Nature Nanotechnology*, vol. 3, no. 4, p. 206, 2008.

[69] C. R. Dean, A. F. Young, I. Meric, C. Lee, L. Wang, S. Sorgenfrei, K. Watanabe, T. Taniguchi, P. Kim, K. L. Shepard *et al.*, "Boron nitride substrates for high-quality graphene electronics," *Nature Nanotechnology*, vol. 5, no. 10, p. 722, 2010.

[70] Z. Ni, L. Ponomarenko, R. Nair, R. Yang, S. Anissimova, I. Grigorieva, F. Schedin, P. Blake, Z. Shen, E. Hill *et al.*, "On resonant scatterers as a factor limiting carrier mobility in graphene," *Nano Letters*, vol. 10, no. 10, pp. 3868–3872, 2010.

[71] I.-T. Lin, Y.-P. Lai, K.-H. Wu, and J.-M. Liu, "Terahertz optoelectronic property of graphene: Substrate-induced effects on plasmonic characteristics," *Applied Sciences*, vol. 4, no. 1, pp. 28–41, 2014.

[72] I.-T. Lin and J.-M. Liu, "Terahertz frequency-dependent carrier scattering rate and mobility of monolayer and aa-stacked multilayer graphene," *IEEE Journal of Selected Topics in Quantum Electronics*, vol. 20, no. 1, pp. 122–129, 2014.

[73] J. Horng, C.-F. Chen, B. Geng, C. Girit, Y. Zhang, Z. Hao, H. A. Bechtel, M. Martin, A. Zettl, M. F. Crommie *et al.*, "Drude conductivity of Dirac fermions in graphene," *Physical Review B*, vol. 83, no. 16, p. 165113, 2011.

[74] M. Jablan, H. Buljan, and M. Soljačić, "Plasmonics in graphene at infrared frequencies," *Physical Review B*, vol. 80, no. 24, p. 245435, 2009.

[75] M. Pykal, P. Jurečka, F. Karlickỳ, and M. Otyepka, "Modelling of graphene functionalization," *Physical Chemistry Chemical Physics*, vol. 18, no. 9, pp. 6351–6372,

2016.

[76] T. Stauber, N. Peres, and A. Geim, "Optical conductivity of graphene in the visible region of the spectrum," *Physical Review B*, vol. 78, no. 8, p. 085432, 2008.

[77] C. Sirtori, "Applied physics: Bridge for the terahertz gap," *Nature*, vol. 417, no. 6885, pp. 132–133, 2002.

[78] V. Gusynin, S. Sharapov, and J. Carbotte, "On the universal ac optical background in graphene," *New Journal of Physics*, vol. 11, no. 9, p. 095013, 2009.

[79] S. Mikhailov, "Nonlinear cyclotron resonance of a massless quasiparticle in graphene," *Physical Review B*, vol. 79, no. 24, p. 241309, 2009.

[80] V. Gusynin, S. Sharapov, and J. Carbotte, "Magneto-optical conductivity in graphene," *Journal of Physics: Condensed Matter*, vol. 19, no. 2, p. 026222, 2006.

[81] T. Morimoto, Y. Hatsugai, and H. Aoki, "Optical hall conductivity in ordinary and graphene quantum hall systems," *Physical Review Letters*, vol. 103, no. 11, p. 116803, 2009.

[82] I. Crassee, J. Levallois, A. L. Walter, M. Ostler, A. Bostwick, E. Rotenberg, T. Seyller, D. Van Der Marel, and A. B. Kuzmenko, "Giant Faraday rotation in single-and multilayer graphene," *Nature Physics*, vol. 7, no. 1, p. 48, 2011.

[83] R. Shimano, G. Yumoto, J. Yoo, R. Matsunaga, S. Tanabe, H. Hibino, T. Morimoto, and H. Aoki, "Quantum Faraday and Kerr rotations in graphene," *Nature Communications*, vol. 4, p. 1841, 2013.

[84] M. Tamagnone, C. Moldovan, J.-M. Poumirol, A. B. Kuzmenko, A. M. Ionescu, J. R. Mosig, and J. Perruisseau-Carrier, "Near optimal graphene terahertz non-reciprocal isolator," *Nature Communications*, vol. 7, p. 11216, 2016.

[85] Y. Zhou, X. Xu, H. Fan, Z. Ren, X. Chen, and J. Bai, "Tunable magneto-optical kerr effect in gated monolayer graphene in terahertz region," *Journal of the Physical Society of Japan*, vol. 82, no. 7, p. 074717, 2013.

[86] M. I. Katsnelson, "Graphene: carbon in two dimensions," *Materials Today*, vol. 10, no. 1-2, pp. 20–27, 2007.

[87] S. Mikhailov, "Non-linear electromagnetic response of graphene," *Europhysics Letters*, vol. 79, no. 2, p. 27002, 2007.

[88] E. Hendry, P. J. Hale, J. Moger, A. Savchenko, and S. Mikhailov, "Coherent nonlinear optical response of graphene," *Physical Review Letters*, vol. 105, no. 9, p. 097401, 2010.

[89] S. Mikhailov and K. Ziegler, "Nonlinear electromagnetic response of graphene: frequency multiplication and the self-consistent-field effects," *Journal of Physics: Condensed Matter*, vol. 20, no. 38, p. 384204, 2008.

[90] S. Mikhailov, "Quantum theory of the third-order nonlinear electrodynamic effects of graphene," *Physical Review B*, vol. 93, no. 8, p. 085403, 2016.

[91] A. Wright, X. Xu, J. Cao, and C. Zhang, "Strong nonlinear optical response of graphene in the terahertz regime," *Applied Physics Letters*, vol. 95, no. 7, p. 072101, 2009.

[92] V. A. Margulis, E. Muryumin, and E. Gaiduk, "Frequency dependence of optical third-harmonic generation from doped graphene," *Physics Letters A*, vol. 380, no. 1, pp. 304–310, 2016.

[93] I. Al-Naib, M. Poschmann, and M. M. Dignam, "Optimizing third-harmonic generation at terahertz frequencies in graphene," *Physical Review B*, vol. 91, no. 20, p. 205407, 2015.

[94] N. Savostianova and S. Mikhailov, "Giant enhancement of the third harmonic in graphene integrated in a layered structure," *Applied Physics Letters*, vol. 107, no. 18, p. 181104, 2015.

[95] H. Y. Hwang, N. C. Brandt, H. Farhat, A. L. Hsu, J. Kong, and K. A. Nelson, "Nonlinear THz conductivity dynamics in p-type CVD-grown graphene," *The Journal of Physical Chemistry B*, vol. 117, no. 49, pp. 15 819–15 824, 2013.

[96] H. A. Hafez, I. Al-Naib, M. M. Dignam, Y. Sekine, K. Oguri, F. Blanchard, D. G. Cooke, S. Tanaka, F. Komori, H. Hibino *et al.*, "Nonlinear terahertz field-induced carrier dynamics in photoexcited epitaxial monolayer graphene," *Physical Review B*, vol. 91, no. 3, p. 035422, 2015.

[97] H. Hafez, I. Al-Naib, K. Oguri, Y. Sekine, M. Dignam, A. Ibrahim, D. Cooke, S. Tanaka, F. Komori, H. Hibino *et al.*, "Nonlinear transmission of an intense terahertz field through monolayer graphene," *AIP Advances*, vol. 4, no. 11, p.

117118, 2014.

[98] M. Paul, Y. Chang, Z. Thompson, A. Stickel, J. Wardini, H. Choi, E. Minot, B. Hou, J. Nees, T. Norris *et al.*, "High-field terahertz response of graphene," *New Journal of Physics*, vol. 15, no. 8, p. 085019, 2013.

[99] M. J. Paul, B. Lee, J. L. Wardini, Z. J. Thompson, A. D. Stickel, A. Mousavian, H. Choi, E. D. Minot, and Y.-S. Lee, "Terahertz induced transparency in single-layer graphene," *Applied Physics Letters*, vol. 105, no. 22, p. 221107, 2014.

[100] P. Bowlan, E. Martinez-Moreno, K. Reimann, T. Elsaesser, and M. Woerner, "Ultrafast terahertz response of multilayer graphene in the nonperturbative regime," *Physical Review B*, vol. 89, no. 4, p. 041408, 2014.

[101] M. Dragoman, D. Neculoiu, G. Deligeorgis, G. Konstantinidis, D. Dragoman, A. Cismaru, A. Muller, and R. Plana, "Millimeter-wave generation via frequency multiplication in graphene," *Applied Physics Letters*, vol. 97, no. 9, p. 093101, 2010.

[102] S.-Y. Hong, J. I. Dadap, N. Petrone, P.-C. Yeh, J. Hone, and R. M. Osgood Jr, "Optical third-harmonic generation in graphene," *Physical Review X*, vol. 3, no. 2, p. 021014, 2013.

[103] T. Low and P. Avouris, "Graphene plasmonics for terahertz to mid-infrared applications," *ACS Nano*, vol. 8, no. 2, pp. 1086–1101, 2014.

[104] I. Crassee, M. Orlita, M. Potemski, A. L. Walter, M. Ostler, T. Seyller, I. Gaponenko, J. Chen, and A. Kuzmenko, "Intrinsic terahertz plasmons and magnetoplasmons in large scale monolayer graphene," *Nano Letters*, vol. 12, no. 5, pp. 2470–2474, 2012.

[105] L. Ju, B. Geng, J. Horng, C. Girit, M. Martin, Z. Hao, H. A. Bechtel, X. Liang, A. Zettl, Y. R. Shen *et al.*, "Graphene plasmonics for tunable terahertz metamaterials," *Nature Nanotechnology*, vol. 6, no. 10, p. 630, 2011.

[106] Y. Fan, N.-H. Shen, T. Koschny, and C. M. Soukoulis, "Tunable terahertz metasurface with graphene cut-wires," *ACS Photonics*, vol. 2, no. 1, pp. 151–156, 2015.

[107] H. Yan, X. Li, B. Chandra, G. Tulevski, Y. Wu, M. Freitag, W. Zhu, P. Avouris, and F. Xia, "Tunable infrared plasmonic devices using graphene/insulator stacks,"

Nature Nanotechnology, vol. 7, no. 5, p. 330, 2012.

[108] P. Q. Liu, F. Valmorra, C. Maissen, and J. Faist, "Electrically tunable graphene anti-dot array terahertz plasmonic crystals exhibiting multi-band resonances," *Optica*, vol. 2, no. 2, pp. 135–140, 2015.

[109] H. Yan, F. Xia, Z. Li, and P. Avouris, "Plasmonics of coupled graphene micro-structures," *New Journal of Physics*, vol. 14, no. 12, p. 125001, 2012.

[110] H. Yan, Z. Li, X. Li, W. Zhu, P. Avouris, and F. Xia, "Infrared spectroscopy of tunable dirac terahertz magneto-plasmons in graphene," *Nano Letters*, vol. 12, no. 7, pp. 3766–3771, 2012.

[111] W. Gao, J. Shu, C. Qiu, and Q. Xu, "Excitation of plasmonic waves in graphene by guided-mode resonances," *ACS Nano*, vol. 6, no. 9, pp. 7806–7813, 2012.

[112] W. Gao, G. Shi, Z. Jin, J. Shu, Q. Zhang, R. Vajtai, P. M. Ajayan, J. Kono, and Q. Xu, "Excitation and active control of propagating surface plasmon polaritons in graphene," *Nano Letters*, vol. 13, no. 8, pp. 3698–3702, 2013.

[113] X. Zhu, W. Yan, P. Uhd Jepsen, O. Hansen, N. Asger Mortensen, and S. Xiao, "Experimental observation of plasmons in a graphene monolayer resting on a two-dimensional subwavelength silicon grating," *Applied Physics Letters*, vol. 102, no. 13, p. 131101, 2013.

[114] W. Wei, J. Nong, L. Tang, Y. Zhu, and H. Shi, "Coupling of graphene plasmonics modes induced by near-field perturbation at terahertz frequencies," *Plasmonics*, vol. 11, no. 4, pp. 1109–1118, 2016.

[115] M. M. Jadidi, A. B. Sushkov, R. L. Myers-Ward, A. K. Boyd, K. M. Daniels, D. K. Gaskill, M. S. Fuhrer, H. D. Drew, and T. E. Murphy, "Tunable terahertz hybrid metal–graphene plasmons," *Nano Letters*, vol. 15, no. 10, pp. 7099–7104, 2015.

[116] W. W. Salisbury, "Absorbent body for electromagnetic waves," Jun. 10 1952, US Patent 2,599,944.

[117] J. Min Woo, M.-S. Kim, H. Woong Kim, and J.-H. Jang, "Graphene based salisbury screen for terahertz absorber," *Applied Physics Letters*, vol. 104, no. 8, p. 081106, 2014.

[118] R. L. Fante and M. T. Mccormack, "Reflection properties of the Salisbury screen,"

IEEE Transactions on Antennas and Propagation, vol. 36, no. 10, pp. 1443–1454, 1988.

[119] B. Wu, H. M. Tuncer, M. Naeem, B. Yang, M. T. Cole, W. I. Milne, and Y. Hao, "Experimental demonstration of a transparent graphene millimetre wave absorber with 28% fractional bandwidth at 140 GHz," *Scientific Reports*, vol. 4, p. 4130, 2014.

[120] C. Liu, L. Qi, and X. Zhang, "Broadband graphene-based metamaterial absorbers," *AIP Advances*, vol. 8, no. 1, p. 015301, 2018.

[121] A. Andryieuski and A. V. Lavrinenko, "Graphene metamaterials based tunable terahertz absorber: effective surface conductivity approach," *Optics Express*, vol. 21, no. 7, pp. 9144–9155, 2013.

[122] M. Faraji, M. K. Moravvej-Farshi, and L. Yousefi, "Tunable THz perfect absorber using graphene-based metamaterials," *Optics Communications*, vol. 355, pp. 352–355, 2015.

[123] Y. Zhang, Y. Feng, B. Zhu, J. Zhao, and T. Jiang, "Graphene based tunable metamaterial absorber and polarization modulation in terahertz frequency," *Optics Express*, vol. 22, no. 19, pp. 22 743–22 752, 2014.

[124] G. Deng, P. Chen, J. Yang, Z. Yin, and L. Qiu, "Graphene-based tunable polarization sensitive terahertz metamaterial absorber," *Optics Communications*, vol. 380, pp. 101–107, 2016.

[125] R. Alaee, M. Farhat, C. Rockstuhl, and F. Lederer, "A perfect absorber made of a graphene micro-ribbon metamaterial," *Optics Express*, vol. 20, no. 27, pp. 28 017–28 024, 2012.

[126] B.-z. Xu, C.-q. Gu, Z. Li, L.-l. Liu, and Z.-y. Niu, "Circuit model for graphene-based absorber at low-terahertz frequencies," *Journal of Physics D: Applied Physics*, vol. 47, no. 25, p. 255103, 2014.

[127] S. He and T. Chen, "Broadband THz absorbers with graphene-based anisotropic metamaterial films," *IEEE Transactions on Terahertz Science and Technology*, vol. 3, no. 6, pp. 757–763, 2013.

[128] B.-z. Xu, C.-q. Gu, Z. Li, and Z.-y. Niu, "A novel structure for tunable terahertz

absorber based on graphene," *Optics Express*, vol. 21, no. 20, pp. 23 803–23 811, 2013.

[129] M. Wang, Y. Wang, M. Pu, C. Hu, X. Wu, Z. Zhao, and X. Luo, "Circular dichroism of graphene-based absorber in static magnetic field," *Journal of Applied Physics*, vol. 115, no. 15, p. 154312, 2014.

[130] M. Tamagnone, A. Fallahi, J. R. Mosig, and J. Perruisseau-Carrier, "Fundamental limits and near-optimal design of graphene modulators and non-reciprocal devices," *Nature Photonics*, vol. 8, no. 7, p. 556, 2014.

[131] M. Tamagnone, T. M. Slipchenko, C. Moldovan, P. Q. Liu, A. Centeno, H. Hasani, A. Zurutuza, A. M. Ionescu, L. Martin-Moreno, J. Faist *et al.*, "Magnetoplasmonic enhancement of Faraday rotation in patterned graphene metasurfaces," *Physical Review B*, vol. 97, no. 24, p. 241410, 2018.

[132] J. D. Kraus, "Heinrich Hertz-theorist and experimenter," *IEEE Transactions on Microwave Theory and Techniques*, vol. 36, no. 5, pp. 824–829, 1988.

[133] C. A. Balanis, "Antenna theory: A review," *Proceedings of the IEEE*, vol. 80, no. 1, pp. 7–23, 1992.

[134] W. L. Stutzman and G. A. Thiele, *Antenna theory and design*. John Wiley & Sons, 2012.

[135] D. Correas-Serrano and J. S. Gomez-Diaz, "Graphene-based antennas for terahertz systems: A review," *arXiv preprint arXiv:1704.00371*, 2017.

[136] A. Dubinov, V. Y. Aleshkin, V. Mitin, T. Otsuji, and V. Ryzhii, "Terahertz surface plasmons in optically pumped graphene structures," *Journal of Physics: Condensed Matter*, vol. 23, no. 14, p. 145302, 2011.

[137] J. Dorfmuller, R. Vogelgesang, W. Khunsin, C. Rockstuhl, C. Etrich, and K. Kern, "Plasmonic nanowire antennas: experiment, simulation, and theory," *Nano Letters*, vol. 10, no. 9, pp. 3596–3603, 2010.

[138] R. Esteban, T. Teperik, and J.-J. Greffet, "Optical patch antennas for single photon emission using surface plasmon resonances," *Physical Review Letters*, vol. 104, no. 2, p. 026802, 2010.

[139] J. M. Jornet and I. F. Akyildiz, "Graphene-based nano-antennas for electromag-

netic nanocommunications in the terahertz band," in *Proceedings of the Fourth European Conference on Antennas and Propagation (EuCAP)*. IEEE, 2010, pp. 1–5.

[140] ——, "Graphene-based plasmonic nano-antenna for terahertz band communication in nanonetworks," *IEEE Journal on Selected Areas in Communications*, vol. 31, no. 12, pp. 685–694, 2013.

[141] I. Llatser, C. Kremers, A. Cabellos-Aparicio, J. M. Jornet, E. Alarcón, and D. N. Chigrin, "Graphene-based nano-patch antenna for terahertz radiation," *Photonics and Nanostructures-Fundamentals and Applications*, vol. 10, no. 4, pp. 353–358, 2012.

[142] J. S. Gomez-Diaz and J. Perruisseau-Carrier, "Microwave to THz properties of graphene and potential antenna applications," in *International Symposium on Antennas and Propagation (ISAP)*. IEEE, 2012, pp. 239–242.

[143] T. Zhou, Z. Cheng, H. Zhang, M. Le Berre, L. Militaru, and F. Calmon, "Miniaturized tunable terahertz antenna based on graphene," *Microwave and Optical Technology Letters*, vol. 56, no. 8, pp. 1792–1794, 2014.

[144] M. Tamagnone, J. G. Diaz, J. Perruisseau-Carrier, and J. R. Mosig, "High-impedance frequency-agile THz dipole antennas using graphene," in *The 7th European Conference on Antennas and Propagation (EuCAP)*. IEEE, 2013, pp. 533–536.

[145] M. Esquius-Morote, J. S. Gómez-Dı, J. Perruisseau-Carrier *et al.*, "Sinusoidally modulated graphene leaky-wave antenna for electronic beamscanning at THz," *IEEE Transactions on Terahertz Science and Technology*, vol. 4, no. 1, pp. 116–122, 2014.

[146] M. Tamagnone, J. Gomez-Diaz, J. Mosig, and J. Perruisseau-Carrier, "Analysis and design of terahertz antennas based on plasmonic resonant graphene sheets," *Journal of Applied Physics*, vol. 112, no. 11, p. 114915, 2012.

[147] M. Tamagnone, J. Gomez-Diaz, J. R. Mosig, and J. Perruisseau-Carrier, "Reconfigurable terahertz plasmonic antenna concept using a graphene stack," *Applied Physics Letters*, vol. 101, no. 21, p. 214102, 2012.

[148] C. Pfeiffer, "Upper bounds on the radiation efficiency of electrically small anten-

nas," in *IEEE International Symposium on Antennas and Propagation & USNC/URSI National Radio Science Meeting*. IEEE, 2017, pp. 1197–1198.

[149] J. Perruisseau-Carrier, M. Tamagnone, J. S. Gomez-Diaz, and E. Carrasco, "Graphene antennas: Can integration and reconfigurability compensate for the loss?" in *European Microwave Conference (EuMC)*. IEEE, 2013, pp. 369–372.

[150] M. Tamagnone, J. S. G. Diaz, J. Mosig, and J. Perruisseau-Carrier, "Hybrid graphene-metal reconfigurable terahertz antenna," in *IEEE MTT-S International Microwave Symposium Digest (IMS)*. IEEE, 2013, pp. 1–3.

[151] E. Carrasco, M. Tamagnone, and J. Perruisseau-Carrier, "Tunable graphene reflective cells for THz reflectarrays and generalized law of reflection," *Applied Physics Letters*, vol. 102, no. 10, p. 104103, 2013.

[152] E. Carrasco and J. Perruisseau-Carrier, "Reflectarray antenna at terahertz using graphene," *IEEE Antennas and Wireless Propagation Letters*, vol. 12, pp. 253–256, 2013.

[153] M. Dragoman, A. Muller, D. Dragoman, F. Coccetti, Plana, and R, "Terahertz antenna based on graphene," *Journal of Applied Physics*, vol. 107, no. 10, p. 104313, 2010.

Chapter 3

Finite-Difference Time-Domain Modelling on Linearity of Graphene

3.1 Introduction

In recent years, applications of graphene attract great interest among researchers due to its extraordinary electronic properties [1]. Externally applied voltage [2], magnetic biasing [3] and sample geometry [4] all can change the electronic properties of graphene. These facts make graphene a candidate for performance tunable devices, such as graphene-based electromagnetic (EM) devices, governed by the Maxwell's equations [5].

Theoretical and experimental work on the conductivity of graphene have paved the way for the design of novel THz devices manipulating EM waves [6]. To support the design of EM devices, numericall modelling has always been considered as an important tool. If a closed-form solution to Maxwell equations cannot be obtained, numerical modelling methods are indispensable for analysis of device performance.

The background of FDTD modelling on the linear response of graphene is reviewed in this chapter. An FDTD modelling method based on the auxiliary element approach has been proposed. The simulation results demonstrate good agreement with theoretical and experimental results published in the literature. The proposed modelling methods are expected to support the design of graphene-based devices which can manipulate EM waves.

3.2 The state-of-the-art of FDTD Modelling on Linear Response of Graphene

Researchers have proposed several methods to model graphene-based structures. In this section, a review is provided from two aspects on modelling: the two-dimensional nature of graphene and the linear conductivity of graphene.

3.2.1 FDTD Modelling on the 2D Nature of Graphene

Graphene, consisting of a mono-layer carbon atoms, is a two-dimensional material. However, traditional materials considered in FDTD modelling are three-dimensional materials. Due to the 2D nature, the sheet conductivity of graphene is in the unit of Siemens (S) rather than the volumetric conductivity in the unit of Siemens/metre (S/m). Thus, the first issue related to FDTD modelling on graphene is how to deal with its nature of 2D properties. Several solutions to this issue have been proposed.

Many researchers have modelled the graphene by associating its surface conductivity with the volumetric counterpart which is locally averaged in the FDTD grid [7] through a subcell dispersive formulation [8]. The graphene with an averaged frequency-dispersive conductivity can be treated as an electrically thin dispersive material. The influence of subcell with dispersive conductivity on perfectly matched layers and periodic boundary conditions have been discussed in [9] and [10] respectively. It is noticed that the thickness

of graphene in the FDTD simulations equals to the subcell size. In [10], the Yee cell size is set as the $\lambda_{min}/20$ where λ_{min} is the lowest wavelength, and the portion taken by subcell is 0.1. Thus, in simulations, the thickness of graphene is larger than the actual thickness of graphene. As a result, FDTD simulation results do not match with theoretical calculation using Dyadic Green's functions in [11] for incident angle larger than 75 degree.

Graphene can also be modelled as an infinitely thin sheet by using Surface Boundary Condition (SBC) [12] or Surface Impedance Boundary Condition (SIBC) [13]. In the SBC method, backward and forward difference schemes are implemented in the Yee cells around graphene. These two schemes have different accuracy compared to the central difference scheme which is normally adopted in FDTD algortihm [14]. In the SIBC method, the surface impedance needs to be approximated as a sum of partial fractions by using fitting techniques even though a simple Drude model can well describe the intraband conductivity.

Another way to deal with the surface conductivity of graphene is to use Dirac-Delta function [15]. An advantage of this method is that it is easy to implement the algorithm with normal FDTD updating schemes. However, in the updating equations, current terms are divided by the Yee-cell size, which actually means that volumetric current terms are used in the updating equation. This feature leads to the requirement on fine mesh. To increase simulation efficiency limited by fine mesh, the locally one-dimensional finite-difference time-domain (LOD-FDTD) method was applied in [16, 17] and the alternating direction implicit finite-difference time-domain (ADI-FDTD) method was applied in [18]. Moreover, hybrid implicit-explicit finite-difference time-domain (HIE-FDTD) methods have been proposed as well [19–21].

3.2.2 FDTD Modelling on the Linear Conductivity of Graphene

The linear response of graphene has two contributions: intraband conductivity and interband conductivity.

The formula of intraband conductivity of graphene is in the Drude form in the frequency domain. There are several approaches to convert the frequency-dispersive intraband conductivity into time-domain updating equations of FDTD modelling [22]. When magnetic bias is applied to the graphene sheet, a matrix exponential method has been proposed to take anisotropic conductivity of graphene into account [15].

The equation describing the interband conductivity of graphene is logarithmic making it difficult to directly be coupled into the updating equations of FDTD. However, some researchers have used fitting techniques to approximate the equation with suitable formulas written in Lorentz terms [23], complex conjugate terms [24] or other rational terms [25]. The number of fitting items depends on the bandwidth in simulations.

3.3 Proposed FDTD Modelling on Linear Response of Graphene

In this section, details of proposed FDTD modelling on linear response of graphene are provided. The proposed modelling method is based on the auxiliary element method and the Dirac-Delta function.

Consider a free standing graphene sheet in the $x-y$ plane, as shown in Figure 3.1, the current distributions of graphene only exists on its surface without normal components. Thus, the surface conductivity of graphene can be described by a 2D conductivity tensor. In FDTD modelling, we use the conductivity tensor to describe the anisotropic surface conductivity of graphene. The anisotropic conductivity is generated by the gyrotropic

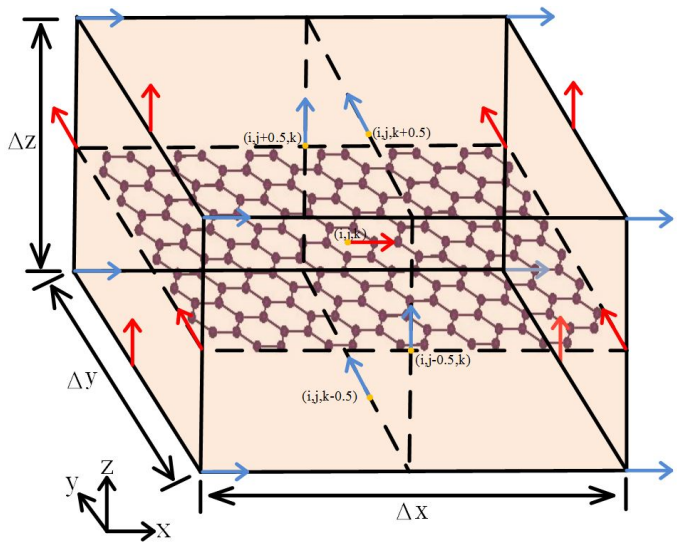

Figure 3.1: A graphene sheet lies in the xy-plane. To remove the Dirac-Delta function from updating equations, a spatial integration is taken from $-\Delta z/2$ to $\Delta z/2$ around the graphene sheet.

effect of electrons under static magnetic field. The conductivity tensor is expressed as

$$\sigma(\omega) = \begin{bmatrix} \sigma_{xx}(\omega) & \sigma_{xy}(\omega) \\ \sigma_{yx}(\omega) & \sigma_{yy}(\omega) \end{bmatrix} = \begin{bmatrix} \sigma_d(\omega) & -\sigma_o(\omega) \\ \sigma_o(\omega) & \sigma_d(\omega) \end{bmatrix} \tag{3.1}$$

where the diagonal element $\sigma_d(\omega)$ and the off-diagonal element $\sigma_o(\omega)$ are equation and respectively. However, only the intraband conductivity is taken into account. It can be found that the conductivity tensor is consistent with the equation which the graphene is not biased as shown in Figure 3.2.

In the frequency domain, the relation between surface currents and electric fields is read as

$$\begin{aligned} J(\omega) &= \begin{bmatrix} J_x(\omega) \\ J_y(\omega) \end{bmatrix} = \begin{bmatrix} \sigma_d(\omega) & -\sigma_o(\omega) \\ \sigma_o(\omega) & \sigma_d(\omega) \end{bmatrix} \begin{bmatrix} E_x(\omega) \\ E_y(\omega) \end{bmatrix} \\ &= \begin{bmatrix} \sigma_d(\omega)E_x(\omega) - \sigma_o(\omega)E_y(\omega) \\ \sigma_o(\omega)E_x(\omega) + \sigma_d(\omega)E_y(\omega) \end{bmatrix} \end{aligned} \tag{3.2}$$

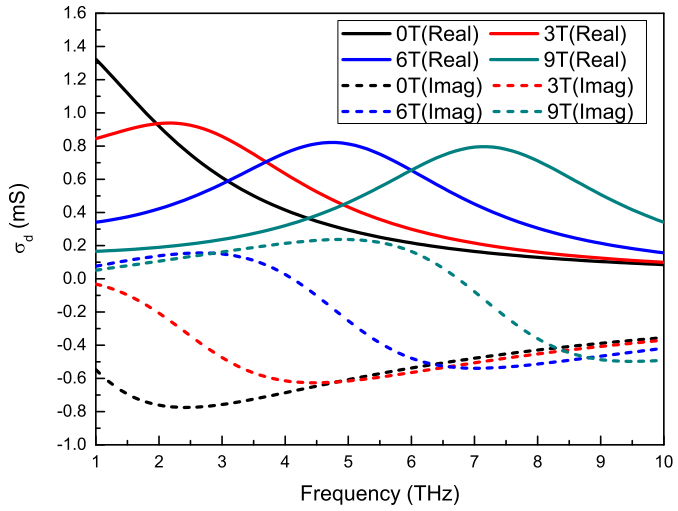

(a)

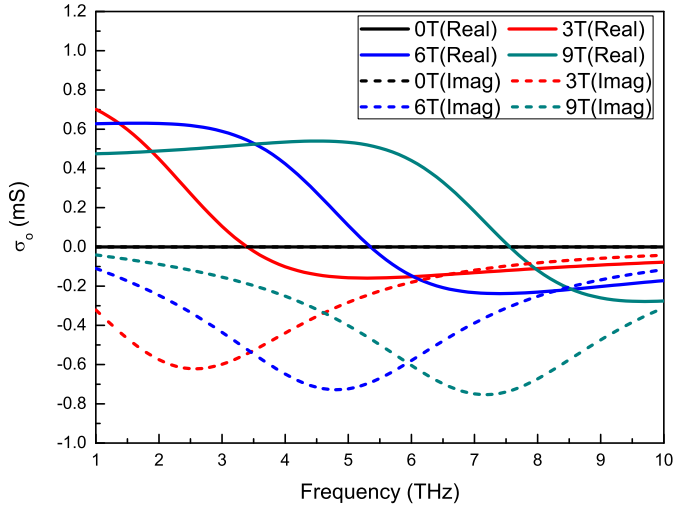

(b)

Figure 3.2: Real part and imaginary part surface conductivity of graphene. The CR frequencies are 2.4 THz, 4.8 THz and 7.2 THz ($T = 300$ K, $\mu_c = 0.2$ eV and $\tau = 0.4$ ps).

Four auxiliary elements are taken as

$$M_i(\omega) = \sigma_d(\omega)E_i(\omega), \text{where } i = x \text{ or } y \tag{3.3}$$

$$N_i(\omega) = \sigma_o(\omega)E_i(\omega), \text{where } i = x \text{ or } y \tag{3.4}$$

Explicitly, their frequency-domain and time-domain relations among surface currents

and auxiliary elements are expressed by the following four equations

$$J_x(\omega) = M_x(\omega) - N_y(\omega) \tag{3.5}$$

$$J_y(\omega) = N_x(\omega) + M_y(\omega) \tag{3.6}$$

$$J_x^{n+0.5} = M_x^{n+0.5} - N_y^{n+0.5} \tag{3.7}$$

$$J_y^{n+0.5} = N_x^{n+0.5} + M_y^{n+0.5} \tag{3.8}$$

Based on the relations above, equation (3.3) can be written as

$$M_i(\omega) = \sigma_d(\omega)E_i(\omega) = \sigma_0 \frac{1 + j\omega\tau}{(\omega_c\tau)^2 + (1 + j\omega\tau)^2} E_i(\omega), \tag{3.9}$$

then we can obtain

$$[(\omega_c\tau)^2 + 1 + 2\tau j\omega + \tau^2(j\omega)^2]M_i(\omega) = \sigma_0(1 + j\omega\tau)E_i(\omega). \tag{3.10}$$

Taking $a = \omega_c\tau$ for convenience, the frequency domain equation can be converted to the time domain equation as such:

$$(a^2 + 1)M_i(t) + 2\tau\frac{\partial M_i(t)}{\partial t} + \tau^2\frac{\partial^2 M_i(t)}{\partial^2 t} = \sigma_0 E_i(t) + \sigma_0\tau\frac{\partial E_i(t)}{\partial t}. \tag{3.11}$$

By applying the time-domain difference approximation to equation (3.11) at the time step $t = n - 0.5$, we can obtain

$$\begin{aligned}(a^2 + 1)M_i^{n-0.5} + 2\tau \times \frac{1}{2}\left(\frac{M_i^{n+0.5} - M_i^{n-0.5}}{\Delta t} + \frac{M_i^{n-0.5} - M_i^{n-1.5}}{\Delta t}\right) + \\ \tau^2 \times \frac{M_i^{n+0.5} - 2M_i^{n-0.5} + M_i^{n-1.5}}{\Delta t^2} = \sigma_0 \times \frac{E_i^n + E_i^{n-1}}{2} + \sigma_0\tau \times \frac{E_i^n - E_i^{n-1}}{\Delta t}.\end{aligned} \tag{3.12}$$

Thus, the updating equation for the auxiliary element M_i is written as

$$\begin{aligned}&\left(\frac{\tau}{\Delta t}+\frac{\tau^2}{\Delta t^2}\right)M_i^{n+0.5}\\&=\left(\frac{\sigma_0}{2}+\frac{\sigma_0\tau}{\Delta t}\right)E_i^n+\left(\frac{\sigma_0}{2}-\frac{\sigma_0\tau}{\Delta t}\right)E_i^{n-1}-\left(1+a^2-\frac{2\tau^2}{\Delta t^2}\right)\\&+\left(\frac{\tau}{\Delta t}-\frac{\tau^2}{\Delta t^2}\right)M_i^{n-1.5}.\end{aligned}\tag{3.13}$$

In terms of the auxiliary element N_i, similar procedures as M_i can be taken to obtain the updating equations of N_i, which are shown from equation (3.14) to equation (3.18).

$$N_i(\omega)=\sigma_0(\omega)E_i(\omega)=\sigma_0\frac{\omega_c\tau}{(\omega_c\tau)^2+(1+j\omega\tau)^2}E_i(\omega)\tag{3.14}$$

$$\left[a^2+1+2\tau j\omega+\tau^2(j\omega)^2\right]N_i(\omega)=\sigma_0 aE_i(\omega)\tag{3.15}$$

$$(a^2+1)N_i(t)+2\tau\frac{\partial N_i(t)}{\partial t}+\tau^2\frac{\partial^2 N_i(t)}{\partial^2 t}=\sigma_0 aE_i(t)\tag{3.16}$$

$$\begin{aligned}(a^2+1)N_i^{n-0.5}+2\tau\times\frac{1}{2}\left(\frac{N_i^{n+0.5}-N_i^{n-0.5}}{\Delta t}+\frac{N_i^{n-0.5}-N_i^{n-1.5}}{\Delta t}\right)\\+\tau^2\times\frac{N_i^{n+0.5}-2N_i^{n-0.5}+N_i^{n-1.5}}{\Delta t^2}=\sigma_0 a\times\frac{E_i^n+E_i^{n-1}}{2}\end{aligned}\tag{3.17}$$

$$\begin{aligned}&\left(\frac{\tau}{\Delta t}+\frac{\tau^2}{\Delta t^2}\right)N_i^{n+0.5}\\&=\frac{\sigma_0 a}{2}E_i^n+\frac{\sigma_0 a}{2}\frac{\sigma_0 a}{2}E_i^{n-1}-\left(1+a^2-\frac{2\tau^2}{\Delta t^2}\right)N_i^{n-0.5}\\&+\left(\frac{\tau}{\Delta t}-\frac{\tau^2}{\Delta t^2}\right)N_i^{n-1.5}\end{aligned}\tag{3.18}$$

Updating equations for M_x, M_y, N_x and N_y are summarised by the following four equations

$$\begin{aligned}M_x^{n+0.5}(i,j,k)&=C_{me}[E_x^n(i,j,k)+E_x^n i-1,j,k]\\&+C_{mep}[E_x^{n-1}(i,j,k)+E_x^{n-1}(i-1,j,k)]-C_{mm}M_x^{n-0.5}(i,j,k)\\&+C_{mmp}M_x^{n-1.5}(i,j,k)\end{aligned}\tag{3.19}$$

$$\begin{aligned} M_y^{n+0.5}(i,j,k) &= C_{me}[E_y^n(i,j,k) + E_y^n i, j-1, k] \\ &+ C_{mep}[E_y^{n-1}(i,j,k) + E_y^{n-1}(i,j-1,k)] - C_{mm}M_y^{n-0.5}(i,j,k) \\ &+ C_{mmp}M_y^{n-1.5}(i,j,k) \end{aligned} \tag{3.20}$$

$$\begin{aligned} N_y^{n+0.5}(i,j,k) &= C_{ne}[E_y^n(i,j,k) + E_y^n(i,j-1,k) + E_y^{n-1}(i,j,k) + E_y^{n-1}(i,j-1,k)] \\ &- C_{nn}N_y^{n-0.5}(i,j,k) + C_{nnp}N_y^{n-1.5}(i,j,k) \end{aligned} \tag{3.21}$$

$$\begin{aligned} N_x^{n+0.5}(i,j,k) &= C_{ne}[E_x^n(i,j,k) + E_x^n(i-1,j,k) + E_x^{n-1}(i,j,k) + E_x^{n-1}(i-1,j,k)] \\ &- C_{nn}N_x^{n-0.5}(i,j,k) + C_{nnp}N_x^{n-1.5}(i,j,k) \end{aligned} \tag{3.22}$$

where $C_{me} = \sigma_0 b(\Delta t + 2\tau)/(4\Delta t)$, $C_{mep} = \sigma_0 b(\Delta t - 2\tau)/(4\Delta t)$, $C_{ne} = \sigma_0 ab/4$, $C_{mm} = C_{nn} = b(1 + a^2 - 2\tau^2/\Delta t^2)$, $C_{mmp} = C_{nnp} = \tau b(\Delta t - \tau)/\Delta t^2$ and $b = \Delta^2/(\tau\Delta t + \tau^2)$.

Using the Dirac-Delta function to represent the 2D dimension of graphene in Maxwell equation, we can obtain

$$\begin{aligned} &\frac{E_x^{n+1}(i,j,k) - E_x^n(i,j,k)}{\Delta t} \\ &\qquad = \frac{1}{\epsilon_x}\Bigg(\frac{H_z^{n+0.5}(i,j,k) - H_z^{n+0.5}(i,j-1,k)}{\Delta y} \\ &\qquad - \frac{H_y^{n+0.5}(i,j,k) - H_y^{n+0.5}(i,j,k-1)}{\Delta z} \\ &\qquad - \frac{J_{2Dx}^{n+0.5}(i,j)\delta(z-k_0) + J_{2Dx}^{n+0.5}(i+1,j)}{2\Delta z} \times \delta(z-k_0)\Bigg) \end{aligned} \tag{3.23}$$

To eliminate the Dirac-Delta function, we need to take the integration along the

direction perpendicular to the surface of graphene [26]

$$\begin{aligned}
&\int_{k_0-\Delta z}^{k_0+\Delta z} \frac{E_x^{n+1}(i,j,k) - E_x^n(i,j,k)}{\Delta t} \mathrm{d}z \\
&= \int_{k_0-\Delta z}^{k_0+\Delta z} \left[\frac{1}{\epsilon_x} \left(\frac{H_z^{n+0.5}(i,j,k) - H_z^{n+0.5}(i,j-1,k)}{\Delta y} \right.\right. \\
&- \frac{H_y^{n+0.5}(i,j,k) - H_y^{n+0.5}(i,j,k-1)}{\Delta z} \\
&\left.\left. - \frac{J_{2Dx}^{n+0.5}(i,j)\delta(z-k_0) + J_{2Dx}^{n+0.5}(i+1,j)}{2\Delta z} \times \delta(z-k_0) \right) \right] \mathrm{d}z
\end{aligned} \tag{3.24}$$

Finally, the updating equations for electric fields are expressed as

$$\begin{aligned}
&\frac{E_x^{n+1}(i,j,k) - E_x^n(i,j,k)}{\Delta t} \\
&= \frac{1}{\epsilon_x} \left(\frac{H_z^{n+0.5}(i,j,k) - H_z^{n+0.5}(i,j-1,k)}{\Delta y} \right. \\
&- \frac{H_y^{n+0.5}(i,j,k) - H_y^{n+0.5}(i,j,k-1)}{\Delta z} \\
&\left. - \frac{J_{2Dx}^{n+0.5}(i,j,k_0) + J_{2Dx}^{n+0.5}(i+1,j,k_0)}{2\Delta z} \right)
\end{aligned} \tag{3.25}$$

$$\begin{aligned}
&\frac{E_y^{n+1}(i,j,k_0) - E_y^n(i,j,k_0)}{\Delta t} \\
&= \frac{1}{\epsilon_x} \left(\frac{H_x^{n+0.5}(i,j,k_0) - H_z^{n+0.5}(i,j,k_0-1)}{\Delta z} \right. \\
&- \frac{H_z^{n+0.5}(i,j,k_0) - H_z^{n+0.5}(i-1,j,k_0)}{\Delta x} \\
&\left. - \frac{J_{2Dy}^{n+0.5}(i,j,k_0) + J_{2Dy}^{n+0.5}(i,j+1,k_0)}{2\Delta z} \right).
\end{aligned} \tag{3.26}$$

The updating equations of magnetic fields follow normal FDTD updating equations.

3.4 Simulation Results and Validation

The proposed method is used to simulate three different scenarios. Simulation results are compared with theoretical or measurement results.

3.4.1 Case One: Tunable Transmission through Graphene

To validate the proposed FDTD method, a suspended graphene in the x-y plane is simulated. The graphene is characterised by $T = 300$ K and $\tau = 0.7$ ps. In the simulation space, conventional cubic Yee cells with $d = 3$ nm are employed. Periodic boundary conditions [27] are used in the x- and y-direction to treat the graphene as an infinite sheet. A normal incident plane wave with a Gaussian pulse is excited by a total field/scattered field boundary [28]. Perfect matched layer absorbs waves propagating in the z-direction. The size of time step is set by Courant–Friedrich–Levy stability [29].

In simulations, the total transmission coefficient is computed by

$$T = \frac{\sqrt{|E_{x,tran}(f)|^2 + |E_{y,tran}(f)|^2}}{|E_{inc}(f)|} \tag{3.27}$$

where $E_{x,tran}(f)$, $E_{y,tran}(f)$ and $E_{inc}(f)$ are frequency-domain values reprenting x-component of transmitted fields, y-component of transmitted fields and incidence fields respectively. The frequency-domain values are converted from time-domain ones by the Fourier transformation.

Figure 3.3 shows the total transmission coefficient with different chemical potentials and magnetic biases. The FDTD simulation results are compared with theoretical results from the equivalent circuit model proposed in [30]. As shown in Figure 3.3, results obtained from the two methods have good agreement with each other.

3.4.2 Case Two: Faraday and Kerr Rotation of Graphene

In simulations, the FDTD boundary conditions are similar to those presented in section 3.4.1. Plane waves polarised in x-direction propagates in z-direction. To calculate the polarisation rotation angles of Faraday effect in FDTD simulations, the following

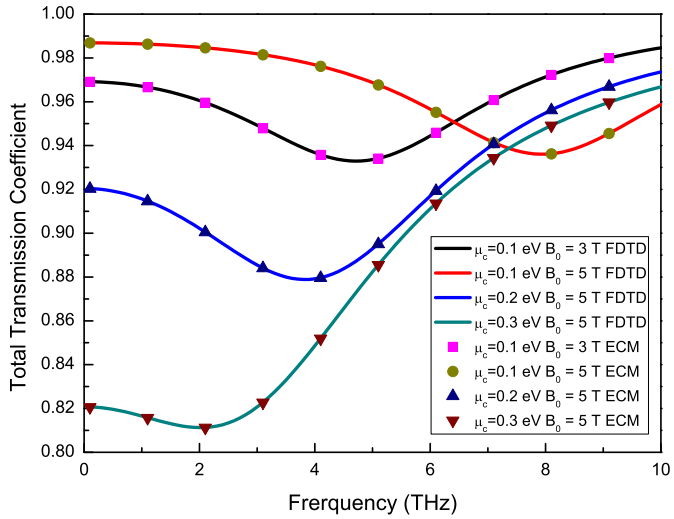

Figure 3.3: Total transmission coefficient of graphene. The comparison of FDTD simulation results (solid lines) and equivalent circuit model [30] results (symbols) is shown in the figure. Different chemical potentials and magnetic biasing are used.

equation is used

$$\theta_F(\omega) = \arctan\left[\frac{E_{y,\text{trans}}(\omega)}{E_{x,\text{trans}}(\omega)}\right]_{\text{real}} \tag{3.28}$$

where the "real" means the real part of a complex Faraday rotation angle, $E_{x,\text{trans}}(\omega)$ is the x-component of the transmission and $E_{y,\text{trans}}(\omega)$ is the y-component of the transmission.

In Figure 3.4, Faraday rotations calculated by the FDTD method are compared with the results obtained from the theoretical formula expressed as [31]

$$\theta_F(\omega) = \frac{1}{2}\arg\left[\frac{2 + Z_0\sigma_+(\omega)}{2 + Z_0\sigma_-(\omega)}\right] \tag{3.29}$$

where $Z_0 = 377\ \Omega$ is the free-space impedance and $\sigma_\pm(\omega) = \sigma_{xx}(\omega) \mp j\sigma_{xy}(\omega)$ is the conductivity for the right (+) and left (-) circularly polarised EM waves.

At the low-THz regime, a uniform graphene layer has shown that the Faraday rotation angle is giant for a single monoatomic layer [32]. The rotation angle decrease with the increment of frequency and the performance of Faraday rotation is, therefore, weaker at

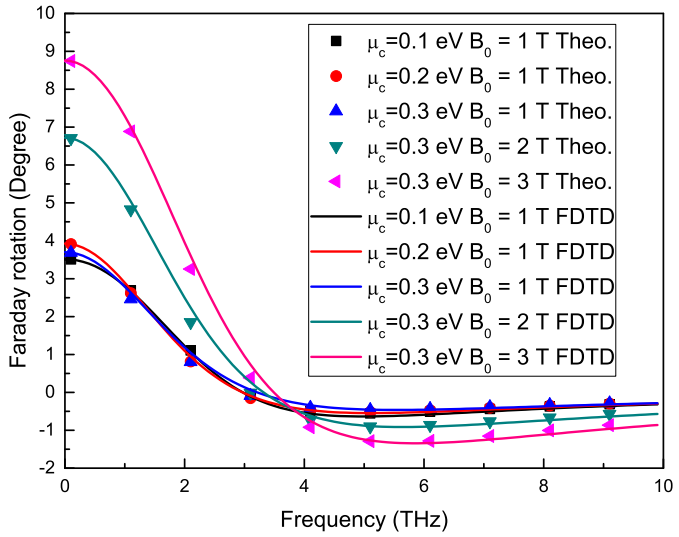

Figure 3.4: Faraday rotations of a suspended graphene. FDTD results (solid lines) are compared with theoretical results (symbols) below 10 THz.

the higher THz regime. Its low-THz characteristic is due to the fact that the Drude peak of graphene conductivity appears in the low-THz regime. By using a patterned graphene layer, giant Faraday rotation has been achieved up to 6 THz [33]. The drawback is that gaps among patterns decrease the whole coverage area of graphene, and the highest rotation angle at the higher THz regime is lower than the rotation angle of a uniform graphene at the low-THz regime. Thus, the obtainable rotation angle is reduced on the whole THz regime.

The angle of Kerr rotations in FDTD simulations is calculated by

$$\theta_K(\omega) = \arctan\left[\frac{E_{y,\mathrm{refl}}(\omega)}{E_{x,\mathrm{refl}}(\omega)}\right]_{\mathrm{real}} \tag{3.30}$$

where the "real" means the real part of a complex Kerr rotation angle, $E_{x,\mathrm{refl}}(\omega)$ is the x-component of the reflection and $E_{y,\mathrm{refl}}(\omega)$ is the y-component of the reflection.

In Figure 3.5, Kerr rotations calculated by the FDTD method are also compared with

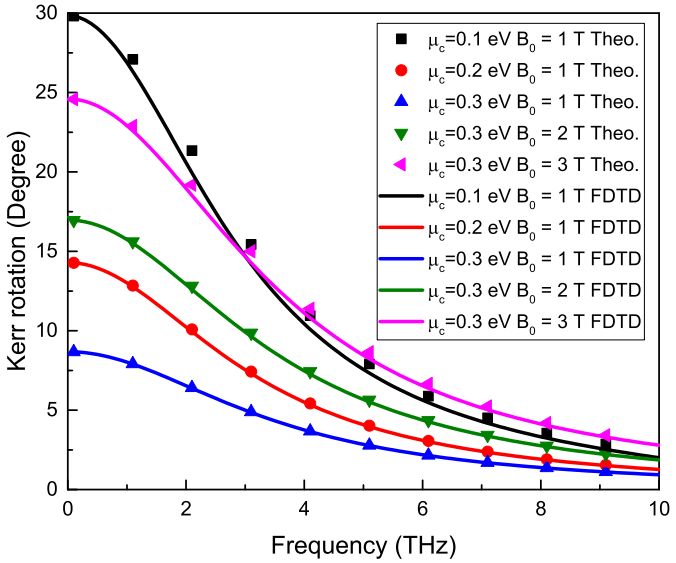

Figure 3.5: Kerr rotations of a suspended graphene. FDTD results (solid lines) are compared with theoretical results (symbols) below 10 THz.

the results obtained from the theoretical formula expressed as [31]

$$\theta_K(\omega) = -\frac{1}{2}\arg\left[\frac{r_-}{r_+}\right] \tag{3.31}$$

where $r_\pm = -Z_0\sigma_\mp/(2+Z_0\sigma_\mp)$ is the complex reflection coefficient for the right (+) and left (-) circularly polarised EM waves.

3.4.3 Case Three: Graphene-based Salisbury Screen

FDTD simulations of Salisbury Screen are compared with measurement results presented in [34]. Figure 3.6 shows the structures of single-layer Salisbury screen and multi-player Salisbury screen. Each dielectric layer has a thickness of 1.3 mm and a relative permittivity of 3.8. PEC is used to simulate a metal sheet with very high conductivity.

All graphene sheets are assumed to have the same parameters: T= 300 K, Γ= 5 meV and $\mu_c = 0.15$ eV. Because the Dirac-Delta function has been used to represent the thickness of graphene in the updating equation (3.23), the currents terms in the updating

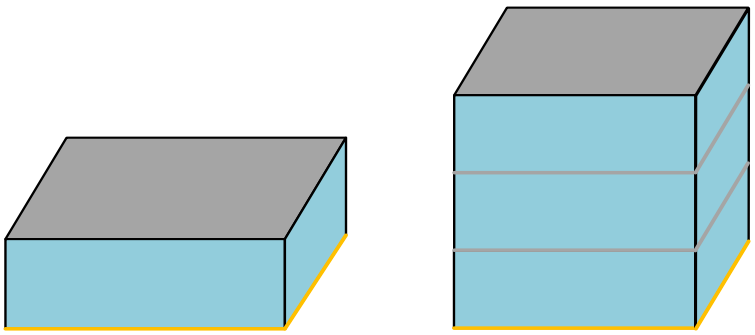

Figure 3.6: The schematic diagram of graphene-based Salisbury screen: (a) single-layer Salisbury screen (b) three-layer Salisbury screen. The grey, blue and yellow colour represent graphene sheet, substrate and metal ground plane respectively.

equations (3.23) and (3.23) act as effective volumetric current terms. In order to satisfy the 2D property of graphene, the FDTD simulations require the Yee cell size which is sufficiently small for the frequency range of interest. In Figure 3.7, the comparison between ECM results and FDTD results demonstrates that the cell size 0.4 μm can be used from 90 GHz to 190 GHz. In the simulation space, uniform cubic Yee cells with $\Delta x = \Delta y = \Delta z = 0.4$ μm are employed.

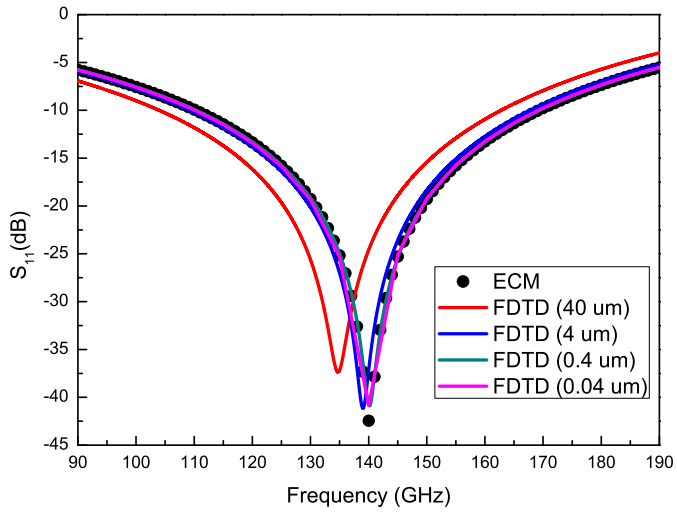

Figure 3.7: Comparison between the results of equivalent circuit model (ECM) [34] and the results of FDTD for the graphene-based Salisbury screen. In FDTD simulations, the cell size takes values from 40 μm, 4 μm, 0.4 μm and 0.04 μm. When the cell size equals to 0.4 μm, the numerical result converges to the ECM result.

In the x- and y-direction, PBCs are used to model the infinite dimension in these directions because normal incidence was used in measurement. In the z-direction, 8-cell CPML is employed [35]. The Total Field/Scattered Field (TF/SF) boundary [28] is implemented in the upper simulation space to generate a normal incidence with a Gaussian pulse. Due to the limitation of Courant–Friedrich–Levy (CFL) stability, the time step is set to be 0.7 fs. FDTD results are compared with the measurement results [34], as illustrated in Figure 3.8. In FDTD simulations, material parameters are taken from the ECM parameters used in [34]. However, Figure 3.8 shows that the peaks of simulation results shift away from experimental results. In Salisbury screen, the resonance frequencies are determined by the thickness of dielectric spacers. The shift could originate from the difference between the ECM parameters and the real thickness of each dielectric spacer in the measurement of [34] due to fabrication errors.

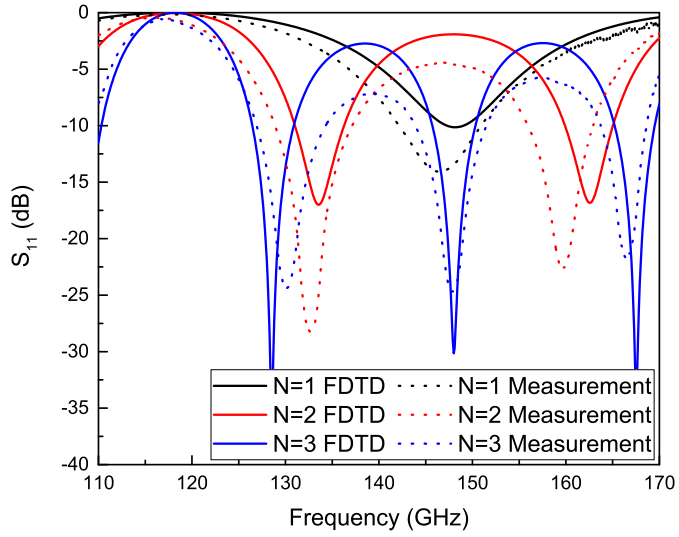

Figure 3.8: Reflection coefficient (dB) of graphene-based Salisbury screen. FDTD results are compared with measurement results published in [34]. N represents the layer number of Salisbury screens.

3.5 Summary

In this chapter, an FDTD modelling method based on the auxiliary element approach has been proposed, and the details of updating equations have been provided. In the

derivation of updating equations, the Dirac-Delta function has been eliminated by the spatial integral around a Yee cell, which leads to finer mesh to represent graphene as a thin film. The proposed method has been used to simulate different scenarios. The simulation results have been compared with theoretical results including transmission, reflection, Faraday rotation and Kerr rotation. Various parameters of graphene have been considered. Moreover, the simulation results of graphene-based Salisbury screens demonstrate good agreement with experimental results published in the literature. It is expected that the proposed modelling method can be used for other graphene-based structures.

References

[1] A. C. Neto, F. Guinea, N. M. Peres, K. S. Novoselov, and A. K. Geim, "The electronic properties of graphene," *Reviews of Modern Physics*, vol. 81, no. 1, p. 109, 2009.

[2] K. S. Novoselov, A. K. Geim, S. V. Morozov, D. Jiang, Y. Zhang, S. V. Dubonos, I. V. Grigorieva, and A. A. Firsov, "Electric field effect in atomically thin carbon films," *Science*, vol. 306, no. 5696, pp. 666–669, 2004.

[3] V. Gusynin and S. Sharapov, "Unconventional integer quantum hall effect in graphene," *Physical Review Letters*, vol. 95, no. 14, p. 146801, 2005.

[4] K. Nakada, M. Fujita, G. Dresselhaus, and M. S. Dresselhaus, "Edge state in graphene ribbons: Nanometer size effect and edge shape dependence," *Physical Review B*, vol. 54, no. 24, p. 17954, 1996.

[5] J. S. Gomez-Diaz and J. Perruisseau-Carrier, "Microwave to THz properties of graphene and potential antenna applications," in *International Symposium on Antennas and Propagation (ISAP)*. IEEE, 2012, pp. 239–242.

[6] K. S. Novoselov, V. Fal, L. Colombo, P. Gellert, M. Schwab, K. Kim *et al.*, "A roadmap for graphene," *Nature*, vol. 490, no. 7419, p. 192, 2012.

[7] G. D. Bouzianas, N. V. Kantartzis, and T. D. Tsiboukis, "RCS analysis of finite graphene sheets through an enhanced frequency-dependent FDTD method," in *The 6th European Conference on Antennas and Propagation (EUCAP)*. IEEE, 2012, pp. 3094–3097.

[8] M. K. Karkkainen, "Subcell FDTD modeling of electrically thin dispersive layers," *IEEE Transactions on Microwave Theory and Techniques*, vol. 51, no. 6, pp. 1774–1780, 2003.

[9] X. Yu and C. D. Sarris, "A perfectly matched layer for subcell FDTD and applications to the modeling of graphene structures," *IEEE Antennas and Wireless Propagation Letters*, vol. 11, pp. 1080–1083, 2012.

[10] G. D. Bouzianas, N. V. Kantartzis, C. S. Antonopoulos, and T. D. Tsiboukis, "Optimal modeling of infinite graphene sheets via a class of generalized FDTD schemes,"

IEEE Transactions on Magnetics, vol. 48, no. 2, pp. 379–382, 2012.

[11] G. W. Hanson, "Dyadic green's functions and guided surface waves for a surface conductivity model of graphene," *Journal of Applied Physics*, vol. 103, no. 6, p. 064302, 2008.

[12] V. Nayyeri, M. Soleimani, and O. M. Ramahi, "Modeling graphene in the finite-difference time-domain method using a surface boundary condition," *IEEE Transactions on Antennas and Propagation*, vol. 61, no. 8, pp. 4176–4182, 2013.

[13] J. C. Mak and C. D. Sarris, "A surface impedance boundary condition approach to the FDTD modeling of graphene," in *Antennas and Propagation Society International Symposium (APSURSI)*. IEEE, 2013, pp. 902–903.

[14] D. M. Sullivan, *Electromagnetic simulation using the FDTD method*. John Wiley & Sons, 2013.

[15] X.-H. Wang, W.-Y. Yin, and Z. Chen, "Matrix exponential FDTD modeling of magnetized graphene sheet," *IEEE Antennas and Wireless Propagation Letters*, vol. 12, pp. 1129–1132, 2013.

[16] I. Ahmed, E. H. Khoo, and E. Li, "Efficient modeling and simulation of graphene devices with the LOD-FDTD method," *IEEE Microwave and Wireless Components Letters*, vol. 23, no. 6, pp. 306–308, 2013.

[17] T. Zhang, X.-H. Wang, Y. Guo, J. Hu, and W.-Y. Yin, "Improved FDTD method for studying on graphene frequency selective surface (GFSS) characteristics for nano-electromagnetics applications," in *IEEE International Symposium on Electromagnetic Compatibility*. IEEE, 2013, pp. 376–379.

[18] I. Ahmed, E. H. Khoo, and D. Li, "Efficient simulation of graphene antennas for biomedicai applications," in *IEEE MTT-S International Microwave Workshop Series on RF and Wireless Technologies for Biomedical and Healthcare Applications*. IEEE, 2013, pp. 1–3.

[19] M.-L. Zhai, H.-L. Peng, X.-H. Wang, X. Wang, Z. Chen, and W.-Y. Yin, "The conformal HIE-FDTD method for simulating tunable graphene-based couplers for thz applications," *IEEE Transactions on Terahertz Science and Technology*, vol. 5, no. 3, pp. 368–376, 2015.

[20] J. Chen, N. Xu, A. Zhang, and J. Guo, "Using dispersion HIE-FDTD method to simulate the graphene-based polarizer," *IEEE Transactions on Antennas and Propagation*, vol. 24, no. 7, pp. 3011–3017, 2016.

[21] Y. Guo, T. Zhang, W.-Y. Yin, and X.-H. Wang, "Improved hybrid FDTD method for studying tunable graphene frequency-selective surfaces (GFSS) for THz-wave applications," *IEEE Transactions on Terahertz Science and Technology*, vol. 5, no. 3, pp. 358–367, 2015.

[22] U. S. Inan and R. A. Marshall, *Numerical electromagnetics: the FDTD method*. Cambridge University Press, 2011.

[23] I. Ahmed, E. H. Khoo, O. Kurniawan, and E. P. Li, "Modeling and simulation of active plasmonics with the FDTD method by using solid state and Lorentz–Drude dispersive model," *JOSA B*, vol. 28, no. 3, pp. 352–359, 2011.

[24] H. Lin, M. F. Pantoja, L. D. Angulo, J. Alvarez, R. G. Martin, and S. G. Garcia, "FDTD modeling of graphene devices using complex conjugate dispersion material model," *IEEE Microwave and Wireless Components Letters*, vol. 22, no. 12, pp. 612–614, 2012.

[25] A. Mock, "Padé approximant spectral fit for FDTD simulation of graphene in the near infrared," *Optical Materials Express*, vol. 2, no. 6, pp. 771–781, 2012.

[26] Z. Kancleris, G. Slekas, and A. Matulis, "Modeling of two-dimensional electron gas sheet in FDTD method," *IEEE Transactions on Antennas and Propagation*, vol. 61, no. 2, pp. 994–996, 2013.

[27] P. Harms, R. Mittra, and W. Ko, "Implementation of the periodic boundary condition in the finite-difference time-domain algorithm for fss structures," *IEEE Transactions on Antennas and Propagation*, vol. 42, no. 9, pp. 1317–1324, 1994.

[28] J. B. Schneider, "Plane waves in FDTD simulations and a nearly perfect total-field/scattered-field boundary," *IEEE Transactions on Antennas and Propagation*, vol. 52, no. 12, pp. 3280–3287, 2004.

[29] R. Courant, K. Friedrichs, and H. Lewy, "On the partial difference equations of mathematical physics," *IBM Journal of Research and Development*, vol. 11, no. 2, pp. 215–234, 1967.

[30] G. Lovat, "Equivalent circuit for electromagnetic interaction and transmission through graphene sheets," *IEEE Transactions on Electromagnetic Compatibility*, vol. 54, no. 1, pp. 101–109, 2012.

[31] R. Shimano, G. Yumoto, J. Yoo, R. Matsunaga, S. Tanabe, H. Hibino, T. Morimoto, and H. Aoki, "Quantum Faraday and Kerr rotations in graphene," *Nature Communications*, vol. 4, p. 1841, 2013.

[32] X. Hu, Q. Huang, Y. Zhao, H. Cai, R. J. Knize, and Y. Lu, "Giant frequency tunability enabled by external magnetic and a gate electric fields in graphene devices," *Optics Express*, vol. 24, no. 6, pp. 6606–6618, 2016.

[33] A. Fallahi and J. Perruisseau-Carrier, "Manipulation of giant Faraday rotation in graphene metasurfaces," *Applied Physics Letters*, vol. 101, no. 23, p. 231605, 2012.

[34] B. Wu, H. M. Tuncer, M. Naeem, B. Yang, M. T. Cole, W. I. Milne, and Y. Hao, "Experimental demonstration of a transparent graphene millimetre wave absorber with 28% fractional bandwidth at 140 GHz," *Scientific Reports*, vol. 4, p. 4130, 2014.

[35] J. A. Roden and S. D. Gedney, "Convolution PML (CPML): An efficient FDTD implementation of the CFS–PML for arbitrary media," *Microwave and Optical Technology Letters*, vol. 27, no. 5, pp. 334–339, 2000.

Chapter 4

Finite-Difference Time-Domain Modelling on Nonlinearity of Graphene

This chapter firstly provides the background of FDTD modelling on nonlinear materials. The challenge of modelling on the nonlinearity of graphene is pointed out. To deal with the challenge, a novel modelling method is proposed to simulate the terahertz (THz) nonlinearity of graphene under strong THz radiation. The updating equation is directly obtained from the $J-E$ characteristic formula, hence the explicit expression of graphene conductivity is not required and the complex time-domain convolution is also avoided. The excitation of odd-order harmonics is successfully demonstrated, and the frequency mixing of two THz signals is also presented.

4.1 Introduction

The band structure of graphene exhibits a linear energy dispersion relation near its Dirac points [1]. This linear band structure can theoretically lead to the suppression

of ac electric current in graphene and hence results in the generation of odd harmonics under strong THz radiation [2]. It has been predicted in [3] that a THz field with a peak value of 1 kV/cm is capable of inducing third-order harmonic generation (THG) on monolayer graphene at room temperature. The amplitude of generated third-order harmonic can be tuned by varying the Fermi level of graphene with bias voltage [4]. To maximise THG, the optimised relation between incident field amplitudes and Fermi levels has been discussed in [5]. Further enhancement can also be achieved by utilising appropriate graphene-dielectric-metal structures [6]. The third-order conductivity of graphene with resonant behavior at the THz spectrum has been proposed in [7] to analyse various nonlinear phenomena. As isolated graphene is a centrosymmetric material, the even-order harmonic generation is forbidden, leaving only odd-order harmonic excitations [8]. In addition, the effects of magnetic bias on the nonlinearity of graphene are also investigated [9]. In terms of experiments, high THz field excitations with peak electric fields between 0.2 and 63 kV/cm have been used to explore the nonlinear properties of graphene. The odd-harmonic generation of graphene has been verified experimentally using a 45-layer graphene sample [10]. Moreover, the nonlinear transmission enhancement of photoexcited monolayer graphene has also been reported in [11], enabling the realisation of graphene-based tunable nonlinear devices.

4.2 The state-of-the-art of FDTD Modelling on Nonlinear Properties of Material

FDTD modelling on the non-linearity of graphene is a relatively new topic. To model graphene that has a frequency-dependent conductivity at THz, complex time-domain convolution is required in their FDTD updating equations. Recently, an FDTD method for modelling the THz nonlinearity of graphene was also proposed. The nonlinearity of graphene is represented as a time-domain instantaneous conductivity $\sigma(t) = \mathbf{J}(t)/\mathbf{E}(t)$, however, resulting in even-order harmonic excitation in their simulation results [12]. In

addition, many FDTD methods for simulating magnetic and electric nonlinearities of other materials have been discussed [13–17].

The magnetic nonlinearity is modeled through updating magnetic fields with a differential permeability derived from the $B-H$ characteristic formula [13].

$$\mathrm{d}\mu(H) = \frac{\partial B}{\partial H} = \mu_m + B_s \exp\left(-|H|/H_c\right)/H_c \tag{4.1}$$

where $\mu_m = 1.67 \times 10^{-4}$ H/m, $B_s = 1.53$ T, and $H_c = 120$ A/m. Although this approach has been successfully implemented to simulate the pulse propagation through nonlinear magnetic sheets, the fine mesh required by the geometric details of magnetic sheets leads to very small time steps [14].

In terms of electric nonlinearity, it involves three-times convolutions [15]

$$\begin{aligned} P_{NL}(x,t) = \epsilon_0 \int_{\infty}^{-\infty} \int_{\infty}^{-\infty} \int_{\infty}^{-\infty} \chi^{(3)}(t-t_1, t-t_2, t-t_3) \\ \times E(x,t_1)E(x,t_2)E(x,t_3)\mathrm{d}t_1\mathrm{d}t_2\mathrm{d}t_3 \end{aligned} \tag{4.2}$$

Under the Born-Oppenheimer approximation [18], a single time convolution approach has been used to analyze both Kerr and Raman interactions [19]

$$\begin{aligned} P_{NL}(x,t) = \epsilon_0 \chi^{(3)} E(x,t) \\ \times \int_{\infty}^{-\infty} [\alpha\delta(t-t') + (1-\alpha)g_R(t-t')]E^2(x,t')\mathrm{d}t' \end{aligned} \tag{4.3}$$

where $\chi^{(3)}$ is the nonlinear coefficient, $\delta(t)$ models Kerr nonresonant transitions and $g_R(t) = [(\tau_1^2+\tau_2^2)/\tau_1\tau_2^2]e^{t/\tau_2}\sin(t/\tau_1)$ models transient Raman scattering, and α parameter rises the relative strengths of the Kerr and Raman interactions. As this model considers the case of non-resonant third-order processes [16], it is only suitable for optical spectra where graphene does not exhibit resonant nonlinear behaviour [20]. Using high order FDTD linear response and nonlinear response can be simulated at the same time [17]. In addition, the numerical simulation of anisotropic materials with frequency-independent

nonlinear constants has been discussed in [20] as well.

4.3 Proposed FDTD Modelling on Nonlinear Response of Graphene

In this section, details of proposed FDTD modelling on non-linearity are provided. The modelling method successfully demonstrates odd-harmonic generations and frequency-mixing effects in the nonlinear response of graphene.

In the FDTD modelling, the non-linearity of graphene is expressed by a $J-E$ characteristic formula describing the surface current of graphene $\mathbf{J}_s(t)$ induced by the strong electric filed $\mathbf{E}(t)$ at THz frequency.

Assuming the thermal energy is much less than the chemical potential of graphene ($k_BT \ll \mu_c$), the $J-E$ characteristic formula of graphene derived from the quasi-classical kinetic theory, which ignores the interband transitions, can be expressed as [2]

$$\mathbf{J}_s(t) = \frac{ev_F p_F^2 \mathbf{P}(t)}{\pi\hbar^2\sqrt{1+P^2(t)}} G\left(Q(t)\right) \tag{4.4}$$

where e is the charge of an electron, v_F is the Fermi velocity of graphene, $p_F = \mu_c/v_F$ is the Fermi momentum, μ_c is the chemical potential, $\mathbf{P}(t) = e\mathbf{A}(t)/p_F$ is a dimensionless vector variable, $P(t)$ is the magnitude of $\mathbf{P}(\mathbf{t})$, i.e. $P(t) = |\mathbf{P}(\mathbf{t})|$, $\mathbf{A}(t) = \int_0^t \mathbf{E}(t')dt'$ is a vector potential depending on electric fields, $\mathbf{E}(t)$ is the in-plane electric field, $\hbar$ is the reduced Planck constant and $G\left(Q(t)\right)$ can be approximated as

$$G\left(Q(t)\right) \approx 1 + \frac{3}{32}Q^2(t) + \frac{35}{1024}Q^4(t) \tag{4.5}$$

where $Q(t) = 2P(t)/(1+P^2(t))$. Compared to the work [21, 22] where only the first expansion term has been used, the equation (4.5) owns better accuracy by taking the second expansion term $Q^2(t)$ and the third expansion term $Q^4(t)$.

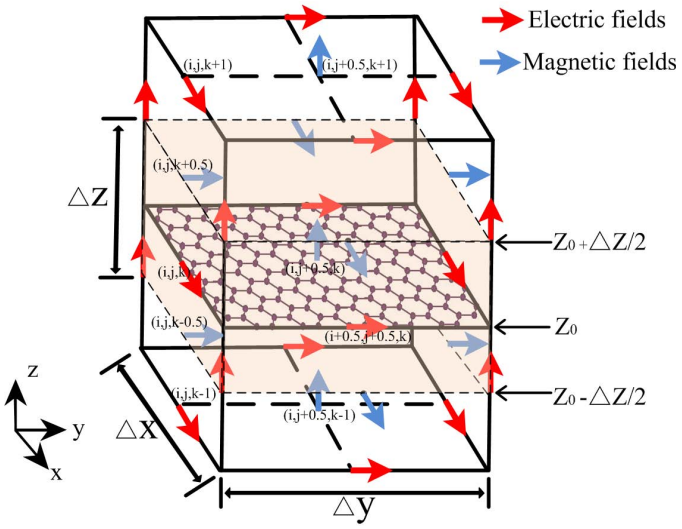

Figure 4.1: Yee cells in FDTD with a graphene sheet in $x-y$ plane. The Yee cell where the graphene sheet exists is filled with light colour. Red (blue) arrows represent electric (magnetic) fields. Δx, Δy and Δz are cell sizes in the three directions.

Figure 4.1 shows the Yee cells used in FDTD modelling of a continuous graphene oriented in the $x-y$ plane. In the modelling, the two-dimensional surface current of graphene is given by $\mathbf{J}_s(t)\delta(z)$, where $\delta(z)$ is the Dirac delta function. The time-domain Maxwell's equation including the surface current can be expressed as

$$\varepsilon\frac{\partial \mathbf{E}(t)}{\partial t} = \nabla \times \mathbf{H}(t) - \mathbf{J}_s(t)\delta(z-z_0) \tag{4.6}$$

where ε is the average permittivity of materials surrounding graphene and z_0 representing the position of graphene.

By taking the difference between time step n and $n+1$ on the $E_x(t;i,j,k)$ component, the following updating equation can be obtained

$$\begin{aligned} E_x^{n+1}(i,j,k) &= E_x^n(i,j,k) \\ &+ \frac{\Delta t}{\varepsilon}\left[\frac{H_z^{n+0.5}(i,j+0.5,k) - H_z^{n+0.5}(i,j-0.5,k)}{\Delta y}\right. \\ &\left. - \frac{H_y^{n+0.5}(i,j,k+0.5) - H_y^{n+0.5}(i,j,k-0.5)}{\Delta z} - J_{sx}^{n+0.5}(i,j,k)\delta(z-z_0)\right] \end{aligned} \tag{4.7}$$

where (i, j, k) represent the position index of a field variable, Δt is the time step and n is a non-negative integer representing the number of time step. The $\delta(z - z_0)$ can be removed by taking spatial integration both sides of equation (4.7) from $z_0 - \Delta z/2$ to $z_0 + \Delta z/2$ [23], and the updating equation can be written as

$$\begin{aligned} E_x^{n+1}(i,j,k) &= E_x^n(i,j,k) \\ &+ \frac{\Delta t}{\varepsilon}\left[\frac{H_z^{n+0.5}(i,j+0.5,k) - H_z^{n+0.5}(i,j-0.5,k)}{\Delta y}\right. \\ &- \frac{H_y^{n+0.5}(i,j,k+0.5) - H_y^{n+0.5}(i,j,k-0.5)}{\Delta z} \\ &\left. - \frac{J_{sx}^{n+0.5}(i,j,k)}{\Delta z}\right] \end{aligned} \tag{4.8}$$

where magnetic field components (i.e. H_y and H_z) follow the normal FDTD updating equations and the expression of $J_{sx}^{n+0.5}(i,j,k)$ is given by

$$\begin{aligned} J_{sx}^{n+0.5}(i,j,k) =& \frac{e v_F p_F^2}{\pi \hbar^2} \times \frac{P_x^{n+0.5}(i,j,k)}{\sqrt{1 + \left(P_x^{n+0.5}(i,j,k)\right)^2}} \\ &\times \left[1 + \frac{3}{32}\left(\frac{2P_x^{n+0.5}(i,j,k)}{1 + \left(P_x^{n+0.5}(i,j,k)\right)^2}\right)^2\right. \\ &\left. + \frac{35}{1024}\left(\frac{2P_x^{n+0.5}(i,j,k)}{1 + \left(P_x^{n+0.5}(i,j,k)\right)^2}\right)^4\right]. \end{aligned} \tag{4.9}$$

By assuming that the incident plane wave is linearly polarised with the electric field in the $x-$direction and the magnetic field in the $y-$direction, a simplified scenario of $\mathbf{P}(t) = P_x(t)$ can be obtained. According to the definitions used in equation (4.4), $P_x^{n+0.5}$ is calculated as

$$\begin{aligned} P_x^{n+0.5} &= \frac{e}{p_F} A_x^{n+0.5} = \frac{e}{p_F} \int_{0.5\Delta t}^{(n+0.5)\Delta t} E_x(t') \mathrm{d}t' \\ &= \frac{e}{p_F} \Delta t \sum_{m=0.5}^{n+0.5} E_x^m \end{aligned} \tag{4.10}$$

where m represents a half-integer step time.

It is noted that equation (4.10) requires electric fields at half-integer time steps. However, the values of electric fields are only calculated at integer time steps in equation (4.8). To deal with this issue, the information of electric fields at half-integer time steps is required.

Electric fields at half-integer time steps can be approximated as the average value of its nearest two integer time steps, and the summation term $\sum_{m=0.5}^{n+0.5} E_x^m$ in equation (4.10) can be expressed as

$$\sum_{m=0.5}^{n+0.5} E_x^m = \frac{1}{2}\left(\sum_{m=0}^{n} E_x^m + \sum_{m=1}^{n+1} E_x^m\right). \tag{4.11}$$

If the auxiliary element B_x^n is defined as

$$B_x^n = \sum_{m=0}^{n} E_x^m, \tag{4.12}$$

then it is easy to achieve the following updating equation by substituting equation (4.12) into (4.11)

$$B_x^{n+1} = B_x^n + E_x^{n+1}. \tag{4.13}$$

According to equations (4.11), (4.12) and (4.13), the updating equation of $P_x^{n+0.5}$ can be written as

$$P_x^{n+0.5} = \frac{e\Delta t}{2p_F}\left(2B_x^n + E_x^{n+1}\right). \tag{4.14}$$

Finally, by substituting equation (4.9) into equaton (4.8), the updating equation of E_x can be expressed as

$$
\begin{aligned}
{E_x}^{n+1}(i,j,k) &= E_x^n(i,j,k) \\
&+ \frac{\Delta t}{\varepsilon}\left[\frac{H_z^{n+0.5}(i,j+0.5,k) - H_z^{n+0.5}(i,j-0.5,k)}{\Delta y}\right. \\
&\left. - \frac{H_y^{n+0.5}(i,j,k+0.5) - H_y^{n+0.5}(i,j,k-0.5)}{\Delta z}\right] \\
&- \frac{\Delta t}{\varepsilon \Delta z}\frac{e v_F p_F^2}{\pi \hbar^2} \times \frac{P_x^{n+0.5}(i,j,k)}{\sqrt{1+\left(P_x^{n+0.5}(i,j,k)\right)^2}} \\
&\times \left[1 + \frac{3}{32}\left(\frac{2P_x^{n+0.5}(i,j,k)}{1+\left(P_x^{n+0.5}(i,j,k)\right)^2}\right)^2\right. \\
&\left. + \frac{35}{1024}\left(\frac{2P_x^{n+0.5}(i,j,k)}{1+\left(P_x^{n+0.5}(i,j,k)\right)^2}\right)^4\right].
\end{aligned}
\tag{4.15}
$$

However, it is noticed that the updating equation (4.14) of $P_x^{n+0.5}$ includes the unknown electric filed component E_x^{n+1}. Thus, to solve the updating equation (4.15), the Newton-Raphson method is adopted, which is explained in the next section.

4.4 The Newton-Raphson Method

In this section, the explanations and details of the Newton-Raphson method used in this chapter are provided.

The Newton-Raphon method, also known as the Newton's method, is a numerical method for finding approximations to the roots of real-valued functions [24]. The features of continuity and real values of time-domain Maxwell's equations makes the Newton's method suitable for the related root-finding problems.

Suppose that a function $f(x)$ has a derivation $f'(x)$ where x is a real number and x_0 is a initial guess for a root of $f(x)$, then a better root x_1 can be calculated as

$$
x_1 = x_0 - \frac{f(x_0)}{f'(x_0)} \tag{4.16}
$$

Such process is repeated as

$$x_{n+1} = x_n - \frac{f(x_n)}{f'(x_n)} \tag{4.17}$$

where n represents the iteration time, until the desired accuracy of $f(x_{n+1})$ is obtained.

The equation (4.15) can be written as

$$\begin{aligned} f(E_x^{n+1}(i,j,k)) &= E_x^n(i,j,k) \\ &+ \frac{\Delta t}{\varepsilon}\left[\frac{H_z^{n+0.5}(i,j+0.5,k) - H_z^{n+0.5}(i,j-0.5,k)}{\Delta y}\right. \\ &\left. - \frac{H_y^{n+0.5}(i,j,k+0.5) - H_y^{n+0.5}(i,j,k-0.5)}{\Delta z}\right] \\ &- E_x^{n+1}(i,j,k) - \frac{\Delta t}{\varepsilon \Delta z}\frac{e v_F p_F^2}{\pi \hbar^2} \times \frac{P_x^{n+0.5}(i,j,k)}{\sqrt{1 + \left(P_x^{n+0.5}(i,j,k)\right)^2}} \\ &\times \left[1 + \frac{3}{32}\left(\frac{2P_x^{n+0.5}(i,j,k)}{1 + \left(P_x^{n+0.5}(i,j,k)\right)^2}\right)^2\right. \\ &\left. + \frac{35}{1024}\left(\frac{2P_x^{n+0.5}(i,j,k)}{1 + \left(P_x^{n+0.5}(i,j,k)\right)^2}\right)^4\right] \\ &= 0 \end{aligned} \tag{4.18}$$

which is a root-searching problem of the unknown electric component $E_x^{n+1}(i,j,k)$.

For convenience, $E_x^{n+1}(i,j,k)$ is defined as x, i.e. $E_x^{n+1}(i,j,k) = x$. To obtain the expression of $f'(x)$, many symbols are defined as follows

$$\begin{aligned} M &= E_x^n(i,j,k) \\ &+ \frac{\Delta t}{\varepsilon}\left[\frac{H_z^{n+0.5}(i,j+0.5,k) - H_z^{n+0.5}(i,j-0.5,k)}{\Delta y}\right. \\ &\left. - \frac{H_y^{n+0.5}(i,j,k+0.5) - H_y^{n+0.5}(i,j,k-0.5)}{\Delta z}\right] \end{aligned} \tag{4.19}$$

which is the fields independent on x,

$$C = \frac{\Delta t}{\varepsilon \Delta z}\frac{e v_F p_F^2}{\pi \hbar^2} \tag{4.20}$$

which is the coefficient of current term, and

$$J = \frac{P(64 + 280P^2 + 467P^4 + 280P^6 + 64P^8)}{64(1 + P^2)^{9/2}} \tag{4.21}$$

is the current term where $P = D(2q + x)$ with D representing $0.5 \times e\Delta t/p_F$ and q representing B_x^n.

The equation (4.18) is rewritten as

$$f(x) = M - x - C \times J. \tag{4.22}$$

With the assistance of a commercial software Mathematica, the $f'(x)$ can be expressed as

$$\begin{aligned}\frac{\partial f}{\partial x} =& -1 + \frac{CD^3(2q+x)^2}{16(1+D^2(2q+x)^2)^{11/2}} \times \Big[-12 - 47D^2(2q+x)^2 \\ &+ 47D^4(2q+x)^4 + 12D^6(2q+x)^6 \Big] + \frac{CD^3(2q+x)^2}{(1+D^2(2q+x)^2)^{3/2}} \\ &\times \left[1 + \frac{35D^4(2q+x)^4}{64(1+D^2(2q+x)^2)^4} + \frac{3D^2(2q+x)^2}{8(1+D^2(2q+x)^2)^2}\right] \\ &- \frac{CD}{\sqrt{1+D^2(2q+x)^2}} \times \left[1 + \frac{35D^4(2q+x)^4}{64(1+D^2(2q+x)^2)^4} \right. \\ &\left. + \frac{3D^2(2q+x)^2}{8(1+D^2(2q+x)^2)^2}\right].\end{aligned} \tag{4.23}$$

The initial guess of root is set as the value of previous electric field $E_x^n(i, j, k)$ and the process of root searching repeats until an accuracy of 10^{-8} is obtained.

4.5 Simulation Results and Validation

Because odd-harmonic generation and frequency-mixing effect are two important nonlinear phenomena, the proposed FDTD modelling method is used to simulate the nonlinear response of graphene on these two phenomena.

In the simulations, a continuous graphene layer, as shown in Figure 4.1, is modelled with periodic boundary conditions in x- and y-directions to analyse the nonlinearity of large-area graphene. Perfectly matched layers are employed in the propagation (z) direction of incident waves. For simplicity, it is assumed that graphene is suspended in air.

The dimensions of Yee cells are set as $\Delta x = \Delta y = \Delta z = 0.1$ μm corresponding to 1/250 of the wavelength of highest simulation frequency (12 THz). This small cell size is capable of providing converged simulation results and the time step is defined according to Courant's stability condition as [25]

$$\Delta t \leq \frac{1}{c\sqrt{\frac{1}{(\Delta x)^2} + \frac{1}{(\Delta y)^2} + \frac{1}{(\Delta z)^2}}}. \tag{4.24}$$

Uniform plane waves with normal incidence in the z-direction are used in simulations. In the simulation of odd-harmonic generation, a sine-modulated Gaussian signal $S_1(t)$ is used as the incident signal. An additional sine-modulated Gaussian signal $S_2(t)$ at a different frequency is used in the simulation of frequency-mixing effect. The two sine-modulated Gaussian signals $S_{1,2}(t)$ are expressed as

$$S_{1,2}(t) = E_0 \sin\left(2\pi f_{c1,2}(t - t_0)\right) \mathrm{e}^{-\left(\frac{t-t_0}{\tau}\right)^2} \tag{4.25}$$

where E_0 is the temporal peak of the Gaussian pulse, $f_{c1,2}$ are the carrier frequencies ($f_{c1} = 2$ THz and $f_{c2} = 3$ THz), $t_0 = 4.8$ ps and $\tau = 1$ ps. Figure 4.2 presents the two signals in both frequency and time domains.

4.5.1 Case One: Odd-harmonic Generation

For the simulations of odd-harmonic generation, the plane wave consisting of only $S_1(t)$ is used. Due to the odd harmonic generation, the primary 2 THz component should not be exclusively excited; the higher-order 6 THz and 10 THz components are also expected

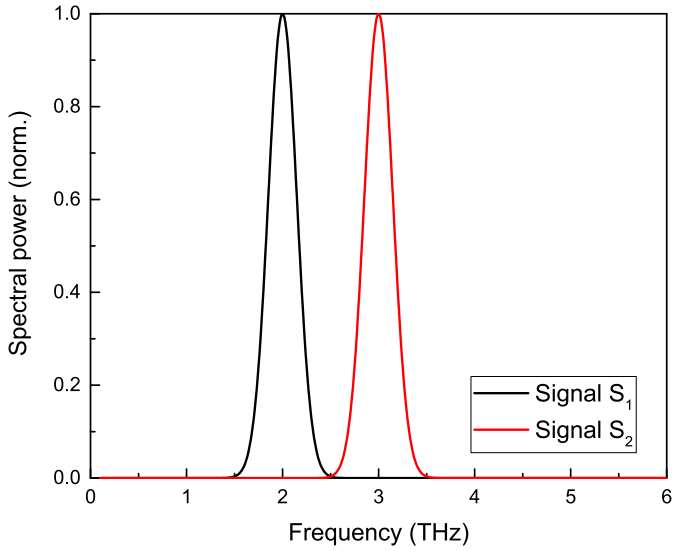

(a)

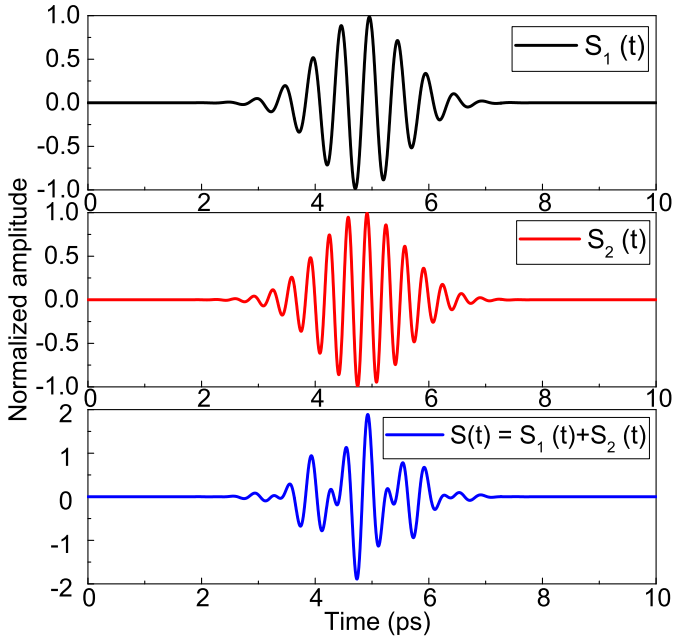

(b)

Figure 4.2: The normalised spectral power of two incident signals S_1 and S_2. The inset is the temporal amplitudes of S_1, S_2 and $S_1 + S_2$, which are normalised to E_0.

in the transmitted spectrum.

The power spectrum of the transmitted waves, plotted in Figure 4.3, is defined as

$$P_{dBc} = 20 \log_{10} \frac{E_{trans}(\omega)}{E_{inc}(2\text{THz})} \tag{4.26}$$

where $E_{trans}(\omega)$ is the amplitude of transmitted waves and $E_{inc}(2\text{THz})$ is the amplitude of incident waves at the carrier frequency 2 THz. The power spectrum clearly shows the generation of the third and the fifth harmonics.

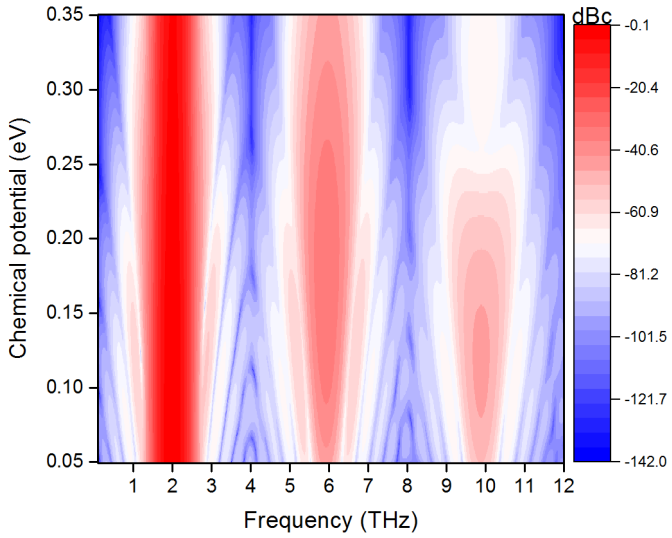

Figure 4.3: The normalised spectral power of the transmitted wave which demonstrates odd harmonic generation. The incidence has a 2 THz central frequency. The generated fundamental, third and fifth harmonics are emphasised by the red colour with darkness representing their strength. Various chemical potentials of graphene are taken into account.

Figure 4.4 shows the spectral amplitudes of the third-order (6 THz) and fifth-order (10 THz) harmonics against the chemical potential of graphene under various incident signal strengths. It can be found that there are optimised chemical potentials for THG and fifth-order harmonic generations (FHG) which vary with the strength of the incident signals, as summarised in Table 4-A.

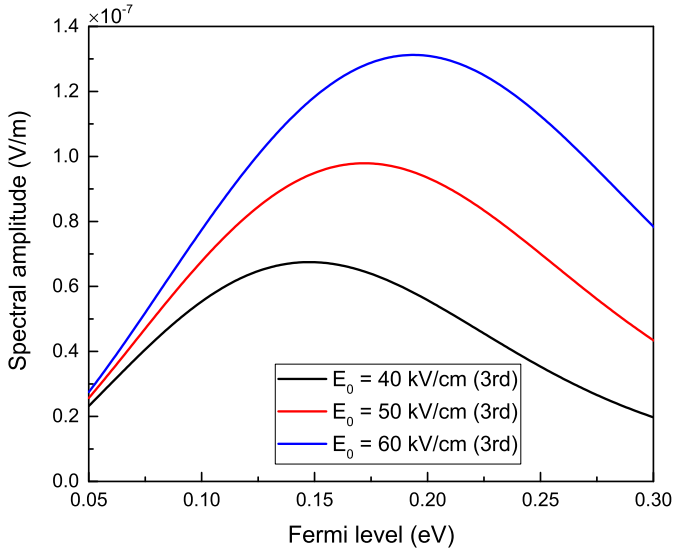

(a)

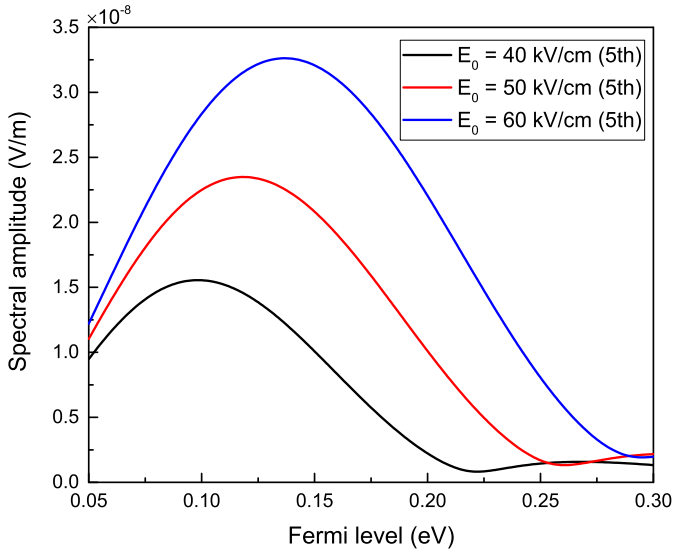

(b)

Figure 4.4: The spectral amplitudes of third-harmonic generation at 6 THz and fifth-harmonic generation at 10 THz under three incidences with different values of E_0: 40 kV/cm, 50 kV/cm and 60 kV/cm.

4.5.2 Case Two: Frequency-mixing Effect

Another nonlinear phenomenon, the frequency-mixing effect, is also demonstrated with the proposed FDTD simulation. Two linearly $x-$polarised plane waves, as shown in Figure 4.2, are used to explore the frequency-mixing effect. The two incident signals are

Table 4-A: Optimised Chemical Potentials for Odd-harmonic Generation

E_0 (kV/cm)	μ(meV) in THG	μ(meV) in FHG
40	148	106
50	172	124
60	195	140

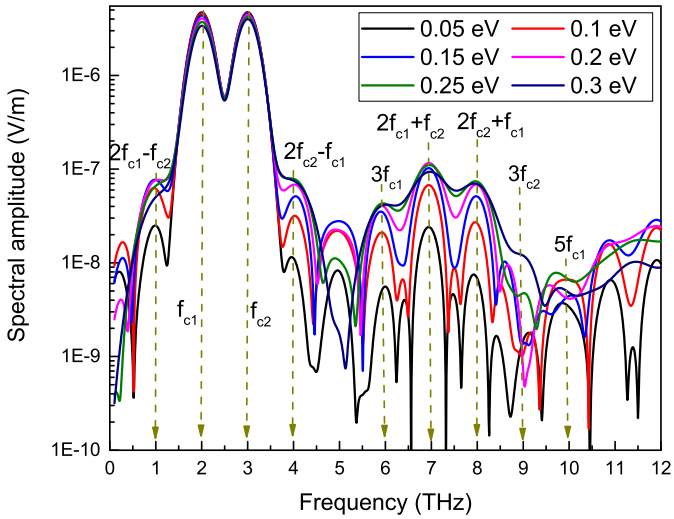

Figure 4.5: The spectral amplitudes of transmitted signal through graphene for frequency-mixing effect. The incidence consists of two signals with central frequency at $f_{c1} = 2$ THz and $f_{c2} = 3$ THz, which is anticipated to generate third-order intermodulation harmonics (i.e. 1 THz, 4 THz, 7 THz and 8 THz) and other high-order harmonics due to mixing effect. Without loss of generality, odd-harmonic generations, such as 6 THz, 9 THz and 10 THz, have also been shown in the figure. Chemical potential of graphene is tuned from 0.05 eV to 0.3 eV with the step 0.05 eV.

summed up directly in the time domain (i.e. $S_{tot}(t) = S_1(t)+S_2(t)$) [26] and the spectral amplitudes of waves transmitted through graphene for various chemical potentials are illustrated in Figure 4.5.

As graphene is a centrosymmetric material, the second order response in graphene is absent. In the third order, under THz radiation consisting of two signals with central frequency f_{c1} and f_{c2} respectively, THz transmission through graphene should have the following resultant Fourier harmonics: f_{c1}, f_{c2}, $3f_{c1}$, $3f_{c2}$, $2f_{c1} \pm f_{c2}$ and $2f_{c2} \pm f_{c1}$ which are clearly shown in Figure 4.5. Meanwhile, other high-order harmonics due to mixing effects can also be seen in Figure 4.5. In addition, the frequency components indicated

by dashed arrows in Figure 4.5 are summarised in Table 4-B.

Table 4-B: Frequency Components in Frequency-mixing Effect

Frequency component	Expression	Value (THz)
Central frequency	f_{c1}	2
	f_{c2}	3
Third-order harmonic	$3f_{c1}$	6
	$3f_{c2}$	9
Fifth-order harmonic	$5f_{c1}$	10
Third-order intermodulation harmonic	$2f_{c1} - f_{c2}$	1
	$2f_{c2} - f_{c1}$	4
	$2f_{c1} + f_{c2}$	7
	$2f_{c2} + f_{c2}$	8

4.6 Summary

The background of FDTD modeeling on nonlinear material is reviewed in this chapter. A novel FDTD modelling method has been proposed to model the nonlinear electrodynamic properties of graphene at THz frequencies. FDTD results successfully demonstrate odd-harmonic generations as well as frequency-mixing effects in wave transmission through graphene. The effects of chemical potential are also investigated. The proposed modelling methods are expected to support the design of graphene-based devices.

References

[1] M. Sprinkle, D. Siegel, Y. Hu, J. Hicks, A. Tejeda, A. Taleb-Ibrahimi, P. Le Fevre, F. Bertran, S. Vizzini, H. Enriquez *et al.*, "First direct observation of a nearly ideal graphene band structure," *Physical Review Letters*, vol. 103, no. 22, p. 226803, 2009.

[2] S. Mikhailov and K. Ziegler, "Nonlinear electromagnetic response of graphene: frequency multiplication and the self-consistent-field effects," *Journal of Physics: Condensed Matter*, vol. 20, no. 38, p. 384204, 2008.

[3] A. Wright, X. Xu, J. Cao, and C. Zhang, "Strong nonlinear optical response of graphene in the terahertz regime," *Applied Physics Letters*, vol. 95, no. 7, p. 072101, 2009.

[4] V. A. Margulis, E. Muryumin, and E. Gaiduk, "Frequency dependence of optical third-harmonic generation from doped graphene," *Physics Letters A*, vol. 380, no. 1, pp. 304–310, 2016.

[5] I. Al-Naib, M. Poschmann, and M. M. Dignam, "Optimizing third-harmonic generation at terahertz frequencies in graphene," *Physical Review B*, vol. 91, no. 20, p. 205407, 2015.

[6] N. Savostianova and S. Mikhailov, "Giant enhancement of the third harmonic in graphene integrated in a layered structure," *Applied Physics Letters*, vol. 107, no. 18, p. 181104, 2015.

[7] S. Mikhailov, "Quantum theory of the third-order nonlinear electrodynamic effects of graphene," *Physical Review B*, vol. 93, no. 8, p. 085403, 2016.

[8] E. Hendry, P. J. Hale, J. Moger, A. Savchenko, and S. Mikhailov, "Coherent nonlinear optical response of graphene," *Physical Review Letters*, vol. 105, no. 9, p. 097401, 2010.

[9] X. Yao and A. Belyanin, "Nonlinear optics of graphene in a strong magnetic field," *Journal of Physics: Condensed Matter*, vol. 25, no. 5, p. 054203, 2013.

[10] P. Bowlan, E. Martinez-Moreno, K. Reimann, T. Elsaesser, and M. Woerner, "Ultrafast terahertz response of multilayer graphene in the nonperturbative regime," *Phys-*

ical Review B, vol. 89, no. 4, p. 041408, 2014.

[11] H. A. Hafez, I. Al-Naib, M. M. Dignam, Y. Sekine, K. Oguri, F. Blanchard, D. G. Cooke, S. Tanaka, F. Komori, H. Hibino *et al.*, "Nonlinear terahertz field-induced carrier dynamics in photoexcited epitaxial monolayer graphene," *Physical Review B*, vol. 91, no. 3, p. 035422, 2015.

[12] A. M. Attiya, "Modeling nonlinear electrical conductivity of graphene by using finite difference time domain," in *The 33rd National Radio Science Conference (NRSC)*. IEEE, 2016, pp. 340–347.

[13] R. Luebbers, K. Kumagai, S. Adachi, and T. Uno, "FDTD calculation of transient pulse propagation through a nonlinear magnetic sheet," *IEEE Transactions on Electromagnetic Compatibility*, vol. 35, no. 1, pp. 90–94, 1993.

[14] R. Holland, "FDTD analysis of nonlinear magnetic diffusion by reduced c," *IEEE Transactions on Antennas and Propagation*, vol. 43, no. 7, pp. 653–659, 1995.

[15] P. M. Goorjian and A. Taflove, "Direct time integration of Maxwell's equations in nonlinear dispersive media for propagation and scattering of femtosecond electromagnetic solitons," *Optics Letters*, vol. 17, no. 3, pp. 180–182, 1992.

[16] R. M. Joseph and A. Taflove, "FDTD Maxwell's equations models for nonlinear electrodynamics and optics," *IEEE Transactions on Antennas and Propagation*, vol. 45, no. 3, pp. 364–374, 1997.

[17] M. Fujii, M. Tahara, I. Sakagami, W. Freude, and P. Russer, "High-order FDTD and auxiliary differential equation formulation of optical pulse propagation in 2-D Kerr and Raman nonlinear dispersive media," *IEEE Journal of Quantum Electronics*, vol. 40, no. 2, pp. 175–182, 2004.

[18] R. Hellwarth, "Third-order optical susceptibilities of liquids and solids," *Progress in Quantum Electronics*, vol. 5, pp. 1–68, 1977.

[19] K. J. Blow and D. Wood, "Theoretical description of transient stimulated raman scattering in optical fibers," *IEEE Journal of Quantum Electronics*, vol. 25, no. 12, pp. 2665–2673, 1989.

[20] C. M. Reinke, A. Jafarpour, B. Momeni, M. Soltani, S. Khorasani, A. Adibi, Y. Xu, and R. K. Lee, "Nonlinear finite-difference time-domain method for the simulation of

anisotropic, $\chi^{(2)}$, and $\chi^{(3)}$ optical effects," *Journal of Lightwave Technology*, vol. 24, no. 1, pp. 624–634, 2006.

[21] H. Dong, C. Conti, A. Marini, and F. Biancalana, "Terahertz relativistic spatial solitons in doped graphene metamaterials," *Journal of Physics B: Atomic, Molecular and Optical Physics*, vol. 46, no. 15, p. 155401, 2013.

[22] Y. Rapoport, V. Grimalsky, I. Iorsh, N. Kalinich, S. Koshevaya, C. Castrejon-Martinez, and Y. S. Kivshar, "Nonlinear reshaping of terahertz pulses with graphene metamaterials," *JETP Letters*, vol. 98, no. 8, pp. 503–506, 2013.

[23] Z. Kancleris, G. Slekas, and A. Matulis, "Modeling of two-dimensional electron gas sheet in FDTD method," *IEEE Transactions on Antennas and Propagation*, vol. 61, no. 2, pp. 994–996, 2013.

[24] C.-N. Kuo, B. Houshmand, and T. Itoh, "Full-wave analysis of packaged microwave circuits with active and nonlinear devices: An FDTD approach," *IEEE Transactions on Microwave Theory and Techniques*, vol. 45, no. 5, pp. 819–826, 1997.

[25] A. Taflove and S. C. Hagness, *Computational electrodynamics*. Artech House, 2005.

[26] S. Mikhailov, "Theory of the nonlinear optical frequency mixing effect in graphene," *Physica E: Low-dimensional Systems and Nanostructures*, vol. 44, no. 6, pp. 924–927, 2012.

Chapter 5

Graphene-based Reflector under Magnetostatic Bias

In the terahertz spectrum, the 2D material graphene owns diagonal and Hall conductivities in the presence of a magnetic field. These peculiar properties provide graphene-based structures with magnetically tunable response to electromagnetic waves. In this chapter, the absolute reflection intensity was measured for a graphene-based reflector illuminated by linearly polarised incident waves at room temperature, which demonstrated the intensity modulation depth (IMD) under different magnetostatic bias by up to 15%. Experimental data were fitted and analysed by a modified equivalent circuit model. In addition, as an important phenomenon of graphene's gyrotropic response, Kerr rotation is discussed according to results achieved from full-wave simulations.

5.1 Introduction

At the terahertz (THz) spectrum, graphene exhibits nonreciprocal and gyrotropic responses due to graphene magnetoplasmons (GMPs) [1–4]. This can be characterised by the anisotropic conductivity with a two-dimensional tensor derived from Kubo formula [5].

The electrostatic tunable conductivity and carrier-density-dependent cyclotron mass of graphene make it different from conventional gyromagnetic materials. In recent years, applications in health, security, astronomy and communication operating in the THz spectrum have begun to emerge [6]. Graphene has shown potential to be employed in novel magneto-optical devices for THz applications [7]. To provide a roadmap for various graphene-based modulators and non-reciprocal devices, researchers have proposed fundamental limits to estimate their optimal performance [8].

In terms of nonreciprocal performance at THz spectrum, graphene-based isolators, demonstrating up to 20 dB isolation, have been experimentally demonstrated for circularly polarized wave incidence [9]. Tunable isolation performance can be achieved by changing the carrier density of graphene [10]. Moreover, the gyrotropic properties of GMPs have also been demonstrated for Faraday rotations (FRs) at room temperature [11]. The FR angle can be enhanced through the effects ofF Fabry–Pérot resonances [12]. However, the tradeoff between the FR angle and the transmission coefficient needs to be considered in such enhancement [13]. Except for the FRs, Kerr rotations (KRs) in reflected waves from graphene have also been measured at low temperature (5K) [14]. It is noticed that graphene's conductivity is temperature-dependent with higher resistivity at higher temperature [15, 16]. However, related applications of GMPs on reflection configuration under linearly polarised illuminations at room temperature have not been reported in great detail.

5.2 Sample Fabrication

The schematic view of a bi-layer graphene-based reflector presented in this work is shown in Figure 5.1. The sample was provided by Dr Jingbo Wu at University of Cambridge. Monolayer graphene was grown on Cu foil (99.8% purity) by chemical vapour deposition (CVD) [17]. Once the Cu foil was loaded into the tube furnace (Graphene Square), it was annealed in H_2 (flow: 20 sccm) at 940 °C for 30 minutes. After annealing, a

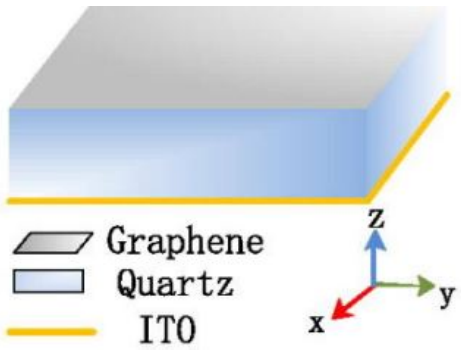

Figure 5.1: Graphene-based reflector. The top reflective surface is stacked-bilayer graphene. The thickness of quartz glass substrate is 0.14 mm. The ground reflector is the ITO film.

uniform layer of graphene was grown on the Cu surface using a mixture of CH_4 and H_2 (flow: 4.6 and 20 sccm) for 30 minutes while keeping the temperature at 940 °C. Graphene was then transferred onto the glass/ indium tin oxide (ITO) substrate with thickness $h = 0.14$ mm by wet transfer [18]. Ammonium persulfate solution was used for the chemical etching of Cu and polymethyl methacrylate (PMMA) was used as a sacrificial layer to support graphene during the etching process. After transfer, PMMA was dissolved in acetone. The transfer process was repeated once for the transfer of the second graphene layer onto glass/ITO substrate.

5.3 FDTD Modelling and Equivalent Circuit Model

FDTD modelling method proposed in chapter 3 is used to obtain full-wave simulation results especially on the Kerr rotation performance, which can also be regarded as the reflection version of Faraday rotation. Moreover, a modified equivalent circuit model is derived to extract parameters of graphene's conductivity,

5.3.1 The Conductivity of Bilayer CVD Graphene

The conductivity of two-stacked monolayer CVD graphene (i.e. bilayer CVD graphene) can be 2-10 times larger than monolayer graphene when positioned on a glass substrate,

as the top layer of the bilayer graphene does not make contact with the underlying substrate [19]. Thus, assuming the interaction between each layer is weak, the conductivity tensor σ_b characterising the bilayer graphene in the $x-y$ plane can be expressed as

$$\sigma_b = N \times \sigma_m = N \times \begin{bmatrix} \sigma_{xx} & \sigma_{xy} \\ \sigma_{yx} & \sigma_{yy} \end{bmatrix} = N \times \begin{bmatrix} \sigma_d & \sigma_o \\ -\sigma_o & \sigma_d \end{bmatrix} \tag{5.1}$$

where N is a value within the range of 2 to 10 representing the increment of overall conductivity compared with monolayer graphene and σ_d (σ_o) is the diagonal (off-diagonal) element in the conductivity tensor σ_m of monolayer graphene. At room temperature σ_d and σ_o can be expressed respectively as [20, 21]

$$\sigma_d = \frac{-j2D}{\pi} \times \frac{\omega - j\Gamma}{(\omega - j\Gamma)^2 - \omega_c^2} \tag{5.2a}$$

$$\sigma_o = \frac{2D}{\pi} \times \frac{\omega_c}{(\omega - j\Gamma)^2 - \omega_c^2} \tag{5.2b}$$

where $D = e^2|\mu_c|/\hbar^2$ is the plasmon spectral weight, e is the charge of an electron, $\hbar$ is the reduced Plank's constant, μ_c is the chemical potential, Γ is the effective scattering rate of electrons, $\omega_c = eB_0v_F^2/\mu_c$ is the cyclotron frequency, B_0 is the strength of the static magnetic field and $v_F = 1.0 \times 10^6$ m/s is the Fermi velocity.

5.3.2 The Permittivity of Glass Substrate

According the literature [22], the relative permittivity of glass substrate takes the value of $4.5 - j0.45$ from 2.5 to 6 THz. To use FDTD method model the complex permittivity, the permittivity is fitted by the Debye model with P poles expressed as [23]

$$\epsilon(\omega) = \epsilon_\infty + \sum_{p=1}^{P} \frac{\Delta\epsilon_p}{1 + j\omega\tau_p} \tag{5.3}$$

where $\epsilon_\infty = 2.53$ is the infinite frequency permittivity, τ_p is the relaxation time of the p^{th} Debye pole and $\Delta\epsilon_p$ is the change in relative permittivity of the p^{th} Debye pole.

Table 5-A: Parameters Used in the Debye Model of Glass Substrate

p	1	2	3	4
$\Delta\epsilon_p$	16985.2	6.60488	-34.7034	30.1338
τ_p (s)	3.789e-9	2.105e-14	1.5245e-14	1.34e-14

Figure 5.2 shows that a four-pole Debye model can fit the permittivity well, and related fitting parameters are summarised in Table 5-A. The FDTD updating equations of glass substrate [24] are provided in the appendix B.

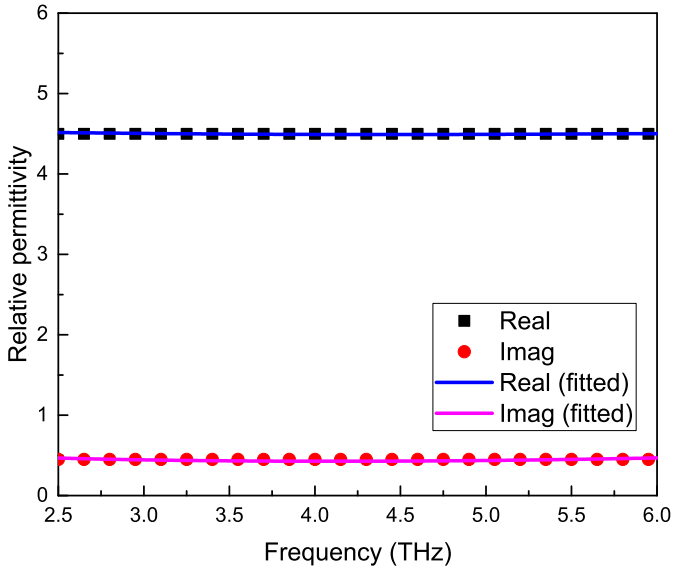

Figure 5.2: The complex relative permittivity of glass substrate is fitted by the Debye model with 4 poles.

5.3.3 The Permittivity of ITO Ground

The complex permittivity of ITO can be expressed as the Drude model taking into account both bound electrons and conduction band electrons [25]

$$\epsilon(\omega) = \epsilon_\infty - \frac{\omega_p^2}{\omega^2 - j\omega\tau^{-1}} \tag{5.4}$$

where $\epsilon_\infty = 4$ is the infinite frequency permittivity, ω_p is the plasma frequency and τ is the relaxation time.

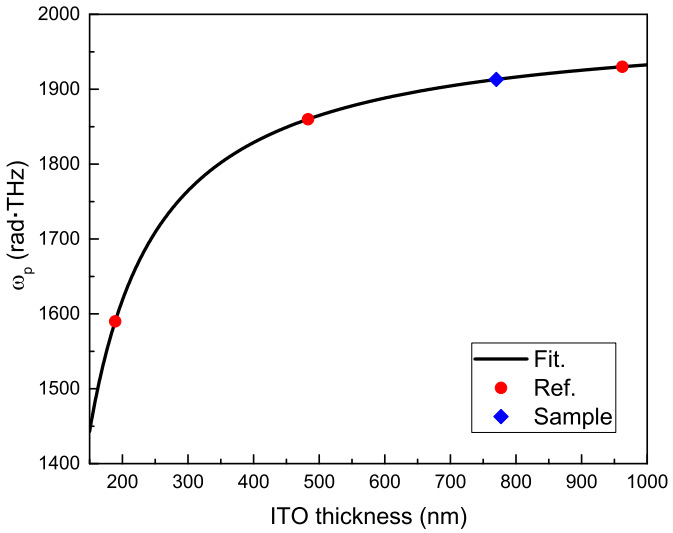

(a)

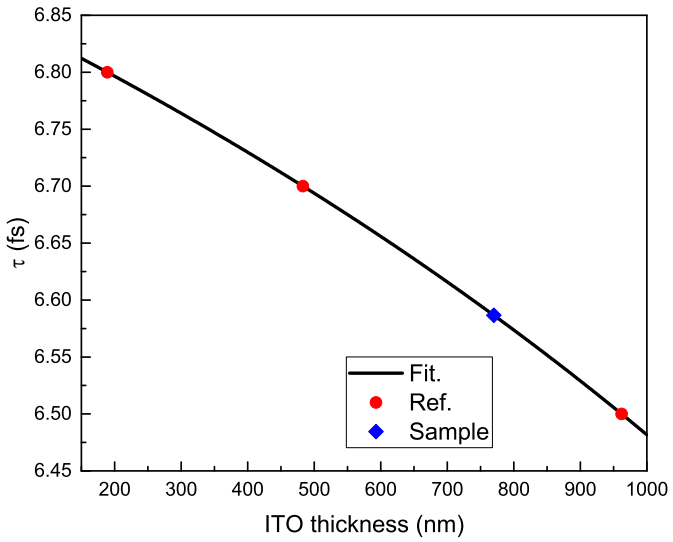

(b)

Figure 5.3: The values of ω_p and τ in the reference [26], represented by red circle, are fitted as functions of ITO thickness. The values of the sample, represented by blue rhombus, are obtained from the fitted curves

The experimental work in [26] has demonstrated that the parameters of ITO films from 189 nm to 962 nm are dependent on the thickness. The scanning electron microscope (SEM) image in the appendix C shows that the thickness of ITO used in our samples is about 770 nm. The $\omega_p = 1913$ rad $\cdot$ THz and $\tau = 6.58$ fs are obtained from the curve fitting as demonstrated in Figure 5.3.

Figure 5.4 shows the relative permittivity used for the ITO film. In addition, the FDTD updating equations of ITO can be derived from the equation (5.4) by the auxiliary differential equation method [27] as provided in the appendix B.

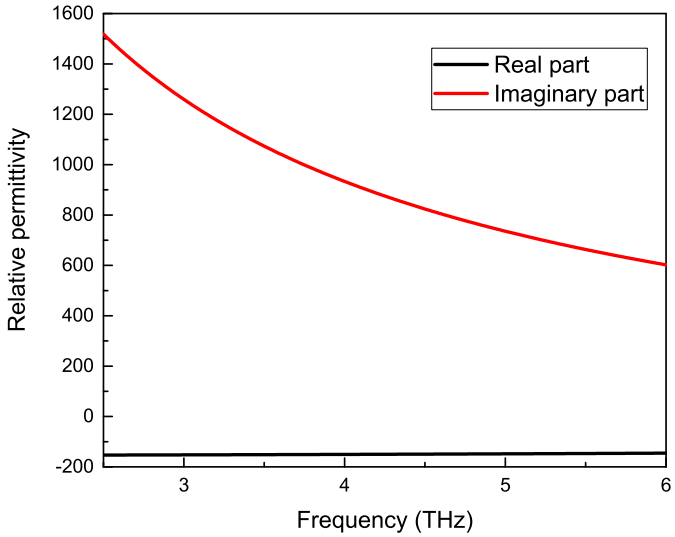

Figure 5.4: Calculated complex relative permittivity of ITO film

5.3.4 The Setup of FDTD Modelling

The FDTD modelling method, which has been proposed in chapter 3, is used to implement the conductivity tensor expressed as the equation (5.1) and the equation (5.2). The structure shown in Figure 5.1 is treated as infinite in the x- and y-directions, thus PBCs are employed in these two directions [28]. CPMLs are employed in the z-direction as absorbing boundaries to terminate simulation domains [29]. The TF/SF boundary is used to generate the x-polarised plane waves propagating in the z-direction [30]. Uniform cubic Yee cells with $\Delta x = \Delta y = \Delta z = 60$ nm are employed. The size of time step $\Delta t = 0.05$ fs is set due to the Courant–Friedrich–Levy stability with a courant factor 0.9.

The calculation of Kerr rotation follows the equation (3.30). The reflection coefficient is calculated by

$$R = \frac{\sqrt{|E_{x,refl}(\omega)|^2 + |E_{y,refl}(\omega)|^2}}{|E_{inc}(\omega)|} \tag{5.5}$$

where $E_{x,refl}(\omega)$, $E_{y,refl}(\omega)$ and $E_{inc}(\omega)$ are frequency-domain values reprenting x-component of transmitted fields, y-component of reflected fields and incidence fields respectively.

5.3.5 Equivalent Circuit Model

In terms of a continuous isotropic graphene sheet, its ECM can be described by a series R-L circuit. The admittance of the R-L circuit equals to the surface conductivity of graphene [31]. The work in [32] has adopted this method to explain the performance of graphene-based absorbers. In comparison with the R-L circuit model, finite graphene with specific geometries owns an extra capacitance element to characterise resonance behaviours. The ECM of graphene patch has been proposed in [33] which is based on a quasi-static approximation [34]. Even through the approximation works well with perfect electric conductor [35, 36], the imperfect conductivity of graphene makes ECM results inaccuracy [37]. Due to the lack of close-form formulas, researchers have proposed numerical approaches to obtain the admittance of graphene-based structures, such as ribbon arrays [38, 39], patch arrays [40] and disk arrays [41].

By using two coupled voltage-control current generators, a close-form formula has been proposed for a continuous graphene sheet under magnetic bias to calculate wave transmission through anisotrpic graphene [42]. According to this model, a modified ECM, as shown in Figure 5.5, is utilised to calculate the reflection performance of graphene-based reflector. In the modified ECMs, the glass substrate is described by its characteristic admittance Y_d and propagation constant γ_d which are calculated according to published data in literature [22]. The ground ITO film is modelled as an equivalent sheet admittance Y_{ITO} [26].

The coupling relation between the voltage V_1 and V_2 in Figure 5.5 can be expressed as

$$V_2 Y_{bo} = \left(\frac{Y_{bo}^2}{Y_0 + Y_{bd} + Y_{sub}} \right) V_1 \tag{5.6}$$

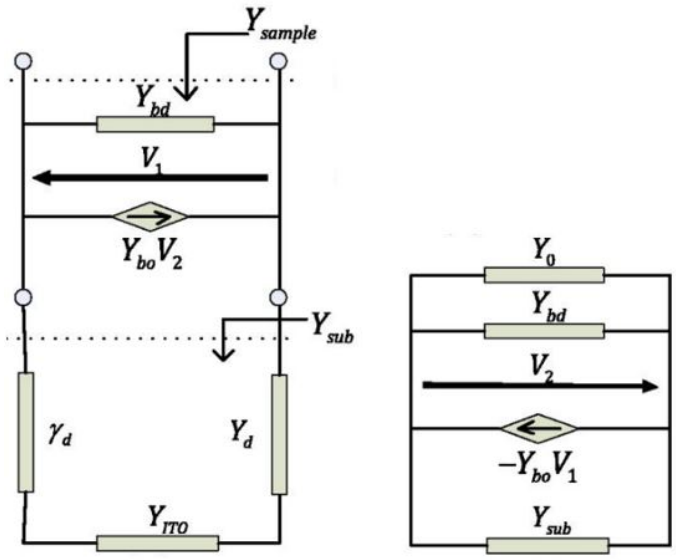

Figure 5.5: Equivalent circuit model for the graphene-based reflector.

where $Y_{bd} = N \times \sigma_d$ ($Y_{bo} = N \times \sigma_o$) is diagonal (off-diagonal) admittance of the bilayer graphene, $Y_0 \approx 1/377$ S is the intrinsic admittance of free space and Y_{sub} is the input admittance of substrate expressed as

$$Y_{sub} = Y_d \times \frac{Y_{ITO} + Y_d \tanh(\gamma_d h)}{Y_d + Y_{ITO} \tanh(\gamma_d h)}. \tag{5.7}$$

According to Eqs.(5.2)(5.6) and (5.7), the sample input admittance Y_{sample} in Figure 5.5 can be written as

$$Y_{sample} = Y_{bd} + Y_{sub} + \frac{Y_{bo}^2}{Y_0 + Y_{bd} + Y_{sub}}. \tag{5.8}$$

Finally, the reflection coefficient of the graphene-based reflector is defined as

$$R_{ECM} = \frac{Y_0 - Y_{sample}}{Y_0 + Y_{sample}}. \tag{5.9}$$

5.3.6 The Validation of the ECM

The ECM is used to extract graphene parameters by fitting techniques. To validate the ECM, the reflection coefficients ordained from FDTD and ECM are compared in Figure 5.6. The parameters of graphene are randomly set as $N = 7$, $\mu_c = 0.2$ eV and $\Gamma = 140$ meV. Figure 5.6 demonstrates that the models can well describe the reflection of the graphene-based structure as shown in Figure 5.1.

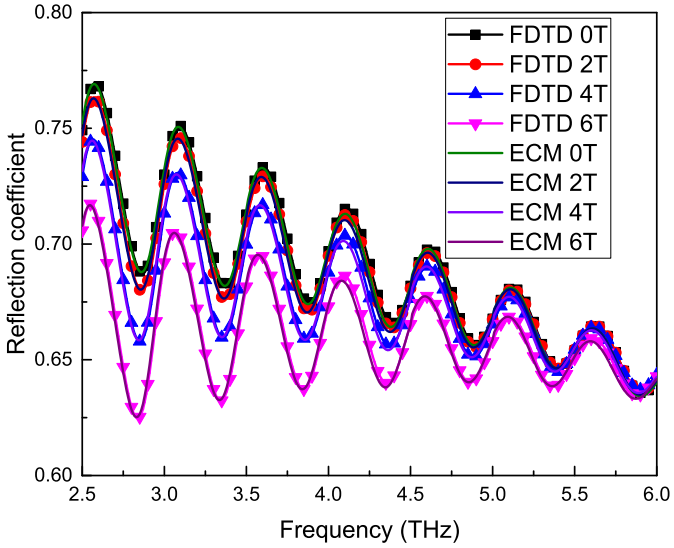

Figure 5.6: Comparison on reflection coefficients ordained from FDTD and ECM. Magnetic bias takes the value of 0 T, 2 T, 4 T and 6 T.

5.4 Measurement Setup and Results

In the measurements, a Fourier-transform infrared spectroscopy (FTIR) setup with magnetostatic bias was employed as shown in Figure 5.7. The measurements were performed with the help from Dr Jean-Marie Pomerol and Prof. Alexey B. Kuzmenko at University of Geneva.

A Michelson interferometer is adapted for the FTIR setup. The light is collimated and directed to a beam splitter. Ideally 50% of the light is refracted towards the fixed

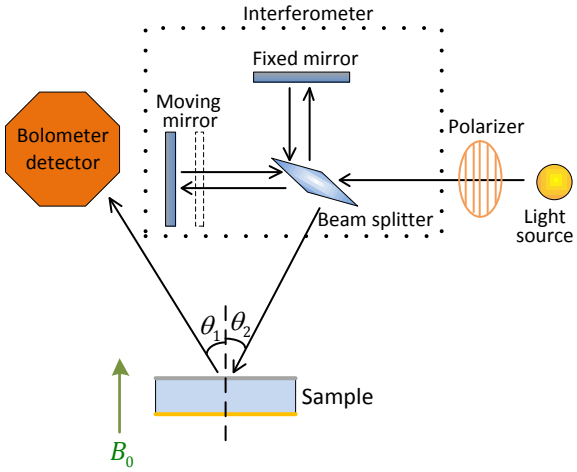

Figure 5.7: The schematic diagram of the measurement setup. A grid-wire gold polarizer is used to convert randomly polarised light generated by Globar light source to linear polarised light. The linear polarised light passes through a Michelson interferometer configuration and illuminates a graphene-based reflector. The reflection from the sample is detected by a He-cooled bolometer detector. The detector and source are tilted by $\theta_1 = \theta_2 = 2.5^{\circ}$. The static magnetic biasing field B_0 in the direction vertical to the sample is generated by a split-coil superconducting magnet, which is not drawn in the diagram.

mirror and 50% is transmitted towards the moving mirror. Light is reflected from the two mirrors back to the beam splitter and some fraction of the original light passes into the sample compartment. The difference in optical path length between the two arms to the interferometer is known as the retardation. An interferogram is obtained by varying the retardation and recording the signal from the detector for various values of the retardation. The form of the interferogram when no sample is present depends on factors such as the variation of source intensity and splitter efficiency with wavelength. When a sample is present, the background interferogram is modulated by the presence of the sample.

Linear incidence was generated by a randomly polarised Globar light source with a grid-wire gold polariser positioned in front of it. The incidence illuminated the sample through a Michelson interferometer configuration. The spectrum was swept from 2.5 THz to 6 THz. The absolute intensity of reflection I_R from the sample was measured

by a He-cooled bolometer detector. The detector and source were tilted by 2.5 degrees from the normal to allow for the positioning of both instruments. Considering the fact that the angles were quite small, the experimental results can be treated as the reflection of a normal incidence. A split-coil superconducting magnet at low temperature generated a static magnetic bias in the direction vertical to the sample which was at room temperature.

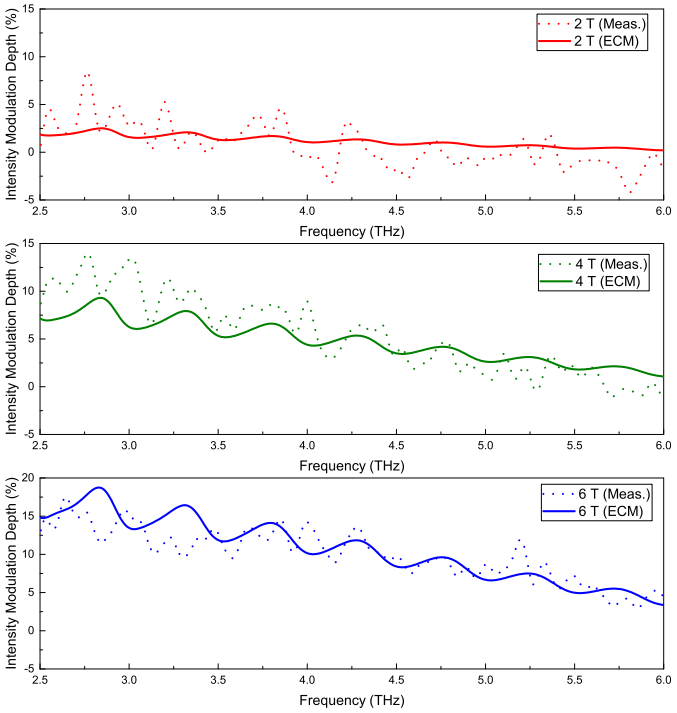

Figure 5.8: Intensity modulation depth. Measurement results are plotted in dots and the fitting results from ECM are plotted in solid lines. Three values of magnetostatic bias are taken: 2 T, 4 T and 6 T. It can be seen that lower spectrum has larger modulation depth. In the case of 6 T, 15% modulation depth at lower spectrum can be obtained around 3 THz.

To demonstrate the intensity variation induced by the statically magnetic bias, the intensity modulation depth (IMD) can be calculated as $1 - I_R(B_0 \neq 0)/I_R(B_0 = 0)$. However, the formula, $1 - [I_R(B_0 \neq 0)/I_{ref}(B_0 \neq 0)]/[I_R(B_0 = 0)/I_{ref}(B_0 = 0)]$, which divides by the reflection intensity of a gold mirror $I_{ref}(B_0)$ as a reference measured under the same experimental conditions, is taken to remove any variation in the measurement system due to the generation of the magnetic field. The experimental results of IMD

based on the formula mentioned above are shown in Figure 5.8. The spectra in Figure 5.8 do not clearly show Fabry–Pérot resonance behaviour due to the loss of the substrate. However, the tunability of graphene and the effect on the IMD is still visible from the measured data.

In the ECM, the IMD is defined as

$$IMD_{ECM} = 1 - \frac{R^2_{ECM}(B_0 \neq 0)}{R^2_{ECM}(B_0 = 0)} \tag{5.10}$$

where R_{ECM} has been defined in the equation (5.9).

The experimental results are fitted according to the ECM. The relevant ECM parameters are as follows: $N = 8$, $\mu_c = 0.21$ eV and $\Gamma = 50$ meV, corresponding to the mobility of 3923 cm^2(V·s)[43]. This is consistent with the mobility of graphene (4050 cm^2(V·s)) fabricated with the same method [17]. It can be found that the variation of IMD in Figure 5.8 is larger at lower frequencies, consistent with the fact that Dirac fermions in continuous graphene have stronger magneto response at lower THz frequencies. At around 3 THz, a 15% IMD was measured with $B_0 = 6$ T.

5.5 Further Discussion

As shown in Figure 5.9, the IMD increases with the increase of magnetostatic bias. According to Eq. (5.2), the magneto-conductivity of graphene is affected by B_0 through the cyclotron frequency ω_c. Because B_0 and μ_c plays inverse roles on the value of ω_c, the MD can be increased by reducing μ_c. Figure 5.10 shows the IMD obtained with ECM for $\mu_c = 0.1$ - 0.4 eV and $B_0 = 6$ T. It can be found that higher IMD can be achieved with lower chemical potential. The maximum IMD of 69% is achieved at $\mu_c = 0.1$ eV. Although the reflector is demonstrated under $B_0 = 6$ T. The required magnetostatic bias is expected to be reduced utilising patterned graphene [44]. The work is useful for potential graphene-based applications at room temperature.

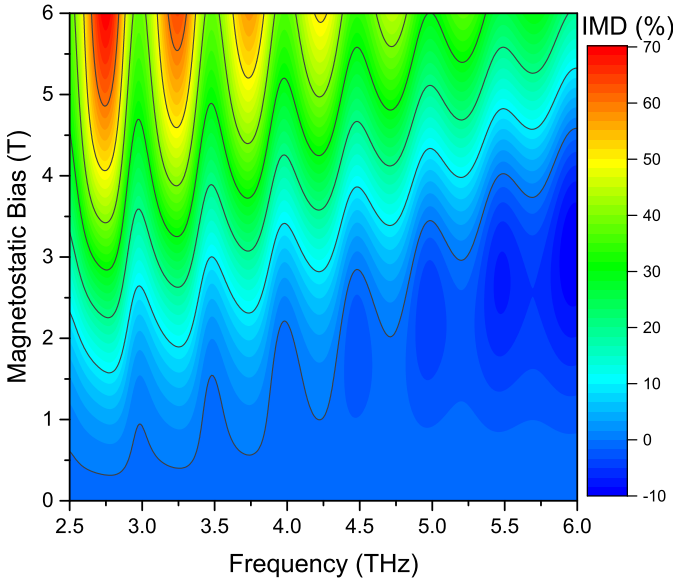

Figure 5.9: Intensity modulation depth (IMD) vs. magnetostatic bias (B_0) at 2.5-6 THz. Chemical potential μ_c is 0.1 eV. B_0 is swept from 0 to 6 T. As B_0 is increased, the tunability increases.

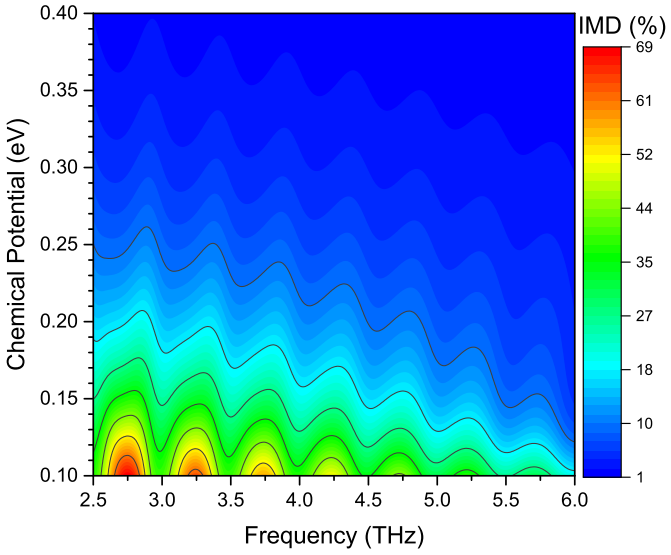

Figure 5.10: Intensity modulation depth (IMD) vs. chemical potential (μ_c) at 2.5 - 6 THz. Magnetostatic bias B_0 is 6 T. μ_c is swept from 0.1 to 0.4 eV. As μ_c is decreased, the tunability generated by magnetostatic bias increases.

The Kerr rotation caused by magnetostatic response of graphene in the structure can be obtained from FDTD simulations as mentioned in the section 5.3.4. The figure-of-merit (FOM) of Kerr rotation can be defined as $\theta\sqrt{R}$, where θ is the Kerr rotation angle

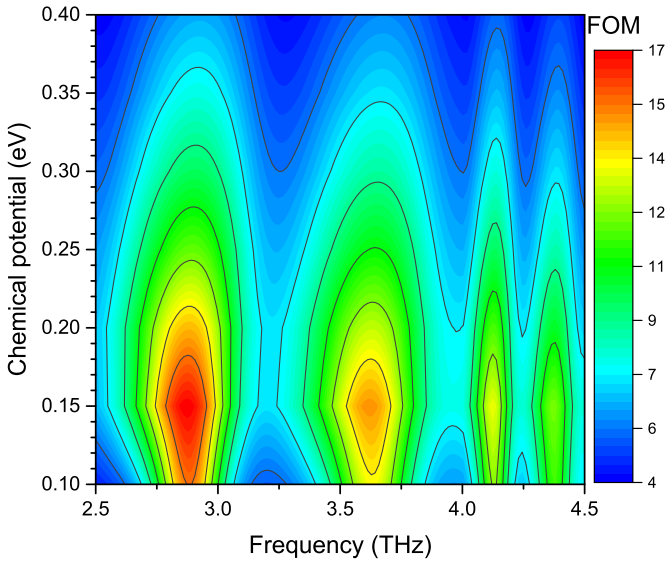

Figure 5.11: Figure-of-merit of Kerr rotation vs. chemical potential for $B_0 = 6$ T

and R is the reflection coefficient[45] and the calculation results are plotted in Figure 5.11 for $B_0 = 6$ T. It is easy to see the highest FOM is achieved with $\mu_c = 0.15$ eV at 2.875 THz. However, the corresponding IMD, as shown in Figure 5.10, is only 40%. Hence, the maximum IMD and FOM cannot be obtained at the same time.

5.6 Summary

In this chapter, the reflection performance of a graphene-based reflector under magnetostatic bias at room temperature is presented. The measurement results show the maximum variation of 15% in IMD when tuning the magnetostatic bias. In order to analyse the reflection performance, a modified ECM in its closed form was derived, and it was shown how the tunability of graphene under magnetostatic bias is highly dependent on the chemical potential. However, further investigations on substrate loss and Kerr rotation are required in the future work.

References

[1] F. H. Koppens, D. E. Chang, and F. J. Garcia de Abajo, "Graphene plasmonics: a platform for strong light–matter interactions," *Nano Letters*, vol. 11, no. 8, pp. 3370–3377, 2011.

[2] L. Ju, B. Geng, J. Horng, C. Girit, M. Martin, Z. Hao, H. A. Bechtel, X. Liang, A. Zettl, Y. R. Shen *et al.*, "Graphene plasmonics for tunable terahertz metamaterials," *Nature Nanotechnology*, vol. 6, no. 10, p. 630, 2011.

[3] M. Tymchenko, A. Y. Nikitin, and L. Martín-Moreno, "Faraday rotation due to excitation of magnetoplasmons in graphene microribbons," *ACS Nano*, vol. 7, no. 11, pp. 9780–9787, 2013.

[4] D. L. Sounas and C. Caloz, "Electromagnetic nonreciprocity and gyrotropy of graphene," *Applied Physics Letters*, vol. 98, no. 2, p. 021911, 2011.

[5] V. Gusynin and S. Sharapov, "Transport of Dirac quasiparticles in graphene: Hall and optical conductivities," *Physical Review B*, vol. 73, no. 24, p. 245411, 2006.

[6] B. Ferguson and X.-C. Zhang, "Materials for terahertz science and technology," *Nature Materials*, vol. 1, no. 1, p. 26, 2002.

[7] F. Fan, S. Chen, and S.-J. Chang, "A review of magneto-optical microstructure devices at terahertz frequencies," *IEEE Journal of Selected Topics in Quantum Electronics*, 2016.

[8] M. Tamagnone, A. Fallahi, J. R. Mosig, and J. Perruisseau-Carrier, "Fundamental limits and near-optimal design of graphene modulators and non-reciprocal devices," *Nature Photonics*, vol. 8, no. 7, p. 556, 2014.

[9] M. Tamagnone, C. Moldovan, J.-M. Poumirol, A. B. Kuzmenko, A. M. Ionescu, J. R. Mosig, and J. Perruisseau-Carrier, "Near optimal graphene terahertz non-reciprocal isolator," *Nature Communications*, vol. 7, p. 11216, 2016.

[10] J.-M. Poumirol, P. Q. Liu, T. M. Slipchenko, A. Y. Nikitin, L. Martin-Moreno, J. Faist, and A. B. Kuzmenko, "Electrically controlled terahertz magneto-optical phenomena in continuous and patterned graphene," *Nature Communications*, vol. 8, p. 14626, 2017.

[11] I. Crassee, J. Levallois, A. L. Walter, M. Ostler, A. Bostwick, E. Rotenberg, T. Seyller, D. Van Der Marel, and A. B. Kuzmenko, "Giant Faraday rotation in single-and multilayer graphene," *Nature Physics*, vol. 7, no. 1, p. 48, 2011.

[12] N. Ubrig, I. Crassee, J. Levallois, I. O. Nedoliuk, F. Fromm, M. Kaiser, T. Seyller, and A. B. Kuzmenko, "Fabry-Perot enhanced Faraday rotation in graphene," *Optics Express*, vol. 21, no. 21, pp. 24 736–24 741, 2013.

[13] H. Da, Q. Bao, R. Sanaei, J. Teng, K. P. Loh, F. J. Garcia-Vidal, and C.-W. Qiu, "Monolayer graphene photonic metastructures: Giant Faraday rotation and nearly perfect transmission," *Physical Review B*, vol. 88, no. 20, p. 205405, 2013.

[14] R. Shimano, G. Yumoto, J. Yoo, R. Matsunaga, S. Tanabe, H. Hibino, T. Morimoto, and H. Aoki, "Quantum Faraday and Kerr rotations in graphene," *Nature Communications*, vol. 4, p. 1841, 2013.

[15] J.-H. Chen, C. Jang, S. Xiao, M. Ishigami, and M. S. Fuhrer, "Intrinsic and extrinsic performance limits of graphene devices on SiO_2," *Nature Nanotechnology*, vol. 3, no. 4, p. 206, 2008.

[16] J. Schiefele, F. Sols, and F. Guinea, "Temperature dependence of the conductivity of graphene on boron nitride," *Physical Review B*, vol. 85, no. 19, p. 195420, 2012.

[17] X. Li, W. Cai, J. An, S. Kim, J. Nah, D. Yang, R. Piner, A. Velamakanni, I. Jung, E. Tutuc *et al.*, "Large-area synthesis of high-quality and uniform graphene films on copper foils," *Science*, vol. 324, no. 5932, pp. 1312–1314, 2009.

[18] R.-H. Kim, M.-H. Bae, D. G. Kim, H. Cheng, B. H. Kim, D.-H. Kim, M. Li, J. Wu, F. Du, H.-S. Kim *et al.*, "Stretchable, transparent graphene interconnects for arrays of microscale inorganic light emitting diodes on rubber substrates," *Nano Letters*, vol. 11, no. 9, pp. 3881–3886, 2011.

[19] A. Dimiev, D. V. Kosynkin, A. Sinitskii, A. Slesarev, Z. Sun, and J. M. Tour, "Layer-by-layer removal of graphene for device patterning," *Science*, vol. 331, no. 6021, pp. 1168–1172, 2011.

[20] H. Yan, Z. Li, X. Li, W. Zhu, P. Avouris, and F. Xia, "Infrared spectroscopy of tunable dirac terahertz magneto-plasmons in graphene," *Nano Letters*, vol. 12, no. 7, pp. 3766–3771, 2012.

[21] I. Crassee, M. Orlita, M. Potemski, A. L. Walter, M. Ostler, T. Seyller, I. Gaponenko, J. Chen, and A. Kuzmenko, "Intrinsic terahertz plasmons and magnetoplasmons in large scale monolayer graphene," *Nano Letters*, vol. 12, no. 5, pp. 2470–2474, 2012.

[22] R. Kitamura, L. Pilon, and M. Jonasz, "Optical constants of silica glass from extreme ultraviolet to far infrared at near room temperature," *Applied Optics*, vol. 46, no. 33, pp. 8118–8133, 2007.

[23] R. J. Luebbers and F. Hunsberger, "FDTD for nth-order dispersive media," *IEEE Transactions on Antennas and Propagation*, vol. 40, no. 11, pp. 1297–1301, 1992.

[24] M. Okoniewski, M. Mrozowski, and M. Stuchly, "Simple treatment of multi-term dispersion in FDTD," *IEEE Microwave and Guided Wave Letters*, vol. 7, no. 5, pp. 121–123, 1997.

[25] M. Born and E. Wolf, *Principles of optics: electromagnetic theory of propagation, interference and diffraction of light*. Elsevier, 2013.

[26] C.-W. Chen, Y.-C. Lin, C.-H. Chang, P. Yu, J.-M. Shieh, and C.-L. Pan, "Frequency-dependent complex conductivities and dielectric responses of indium tin oxide thin films from the visible to the far-infrared," *IEEE Journal of Quantum Electronics*, vol. 46, no. 12, pp. 1746–1754, 2010.

[27] Y. Takayama and W. Klaus, "Reinterpretation of the auxiliary differential equation method for FDTD," *IEEE Microwave and Wireless Components Letters*, vol. 12, no. 3, pp. 102–104, 2002.

[28] P. Harms, R. Mittra, and W. Ko, "Implementation of the periodic boundary condition in the finite-difference time-domain algorithm for fss structures," *IEEE Transactions on Antennas and Propagation*, vol. 42, no. 9, pp. 1317–1324, 1994.

[29] J. A. Roden and S. D. Gedney, "Convolution PML (CPML): An efficient FDTD implementation of the CFS–PML for arbitrary media," *Microwave and Optical Technology Letters*, vol. 27, no. 5, pp. 334–339, 2000.

[30] J. B. Schneider, "Plane waves in FDTD simulations and a nearly perfect total-field/scattered-field boundary," *IEEE Transactions on Antennas and Propagation*, vol. 52, no. 12, pp. 3280–3287, 2004.

[31] D. Correas-Serrano, J. S. Gomez-Diaz, J. Perruisseau-Carrier, and A. Álvarez-Melcón, "Spatially dispersive graphene single and parallel plate waveguides: Analysis and circuit model," *IEEE Transactions on Microwave Theory and Techniques*, vol. 61, no. 12, pp. 4333–4344, 2013.

[32] B. Wu, H. M. Tuncer, M. Naeem, B. Yang, M. T. Cole, W. I. Milne, and Y. Hao, "Experimental demonstration of a transparent graphene millimetre wave absorber with 28% fractional bandwidth at 140 GHz," *Scientific Reports*, vol. 4, p. 4130, 2014.

[33] Y. R. Padooru, A. B. Yakovlev, C. S. Kaipa, G. W. Hanson, F. Medina, and F. Mesa, "Dual capacitive-inductive nature of periodic graphene patches: Transmission characteristics at low-terahertz frequencies," *Physical Review B*, vol. 87, no. 11, p. 115401, 2013.

[34] S. Tretyakov, *Analytical modeling in applied electromagnetics*. Artech House, 2003.

[35] O. Luukkonen, C. Simovski, G. Granet, G. Goussetis, D. Lioubtchenko, A. V. Raisanen, and S. A. Tretyakov, "Simple and accurate analytical model of planar grids and high-impedance surfaces comprising metal strips or patches," *IEEE Transactions on Antennas and Propagation*, vol. 56, no. 6, pp. 1624–1632, 2008.

[36] A. B. Yakovlev, Y. R. Padooru, G. W. Hanson, A. Mafi, and S. Karbasi, "A generalized additional boundary condition for mushroom-type and bed-of-nails-type wire media," *IEEE Transactions on Microwave Theory and Techniques*, vol. 59, no. 3, pp. 527–532, 2011.

[37] X. Huang, X. Zhang, Z. Hu, M. Aqeeli, and A. Alburaikan, "Design of broadband and tunable terahertz absorbers based on graphene metasurface: equivalent circuit model approach," *IET Microwaves, Antennas & Propagation*, vol. 9, no. 4, pp. 307–312, 2014.

[38] A. Khavasi and B. Rejaei, "Analytical modeling of graphene ribbons as optical circuit elements," *IEEE Journal Of Quantum Electronics*, vol. 50, no. 6, pp. 397–403, 2014.

[39] E. Carrasco, M. Tamagnone, and J. Perruisseau-Carrier, "Tunable graphene reflective cells for THz reflectarrays and generalized law of reflection," *Applied Physics*

Letters, vol. 102, no. 10, p. 104103, 2013.

[40] S. Barzegar-Parizi, M. R. Tavakol, and A. Khavasi, "Deriving surface impedance for 2-D arrays of graphene patches using a variational method," *IEEE Journal of Quantum Electronics*, vol. 53, no. 1, pp. 1–6, 2017.

[41] S. Barzegar-Parizi, B. Rejaei, and A. Khavasi, "Analytical circuit model for periodic arrays of graphene disks," *IEEE Journal of Quantum Electronics*, vol. 51, no. 9, pp. 1–7, 2015.

[42] G. Lovat, "Equivalent circuit for electromagnetic interaction and transmission through graphene sheets," *IEEE Transactions on Electromagnetic Compatibility*, vol. 54, no. 1, pp. 101–109, 2012.

[43] D. L. Sounas and C. Caloz, "Gyrotropy and nonreciprocity of graphene for microwave applications," *IEEE Transactions on Microwave Theory and Techniques*, vol. 60, no. 4, pp. 901–914, 2012.

[44] M. Tamagnone, T. M. Slipchenko, C. Moldovan, P. Q. Liu, A. Centeno, H. Hasani, A. Zurutuza, A. M. Ionescu, L. Martin-Moreno, J. Faist *et al.*, "Magnetoplasmonic enhancement of Faraday rotation in patterned graphene metasurfaces," *Physical Review B*, vol. 97, no. 24, p. 241410, 2018.

[45] J. Qin, S. Xia, K. Jia, C. Wang, T. Tang, H. Lu, L. Zhang, P. Zhou, B. Peng, L. Deng *et al.*, "Enhanced Faraday rotation and magneto-optical figure of merit in gold grating/graphene/silicon hybrid magneto-plasmonic devices," *APL Photonics*, vol. 3, no. 1, p. 016103, 2018.

Chapter 6

Graphene-based Reflectarray Antennas

In this chapter, two graphene enabled reflectarray antennas are presented. The first one is based on the phase distribution on reflecting surfaces [1], where the phase variation is achieved by tuning the chemical potential of graphene patches. The second one is based on the generalised Snell's Law [2], where the phase gradient of the EM surface is achieved by an aperiodic array of split-ring resonator (SRR) structures.

6.1 Introduction

In recent years, infrared (IR) spectrum has gained the interest of a number of industries for applications such as wireless communications, imaging and remote sensing [3, 4]. Many of these systems require beam steering so as to increase communication capacity and minimise the interference from other sources. One way to achieve beam steering of EM radiation is through a reflective surface with a spatial phase distribution, otherwise known as a reflectarray antenna [5].

The 2D material graphene, possesses a chemical-potential-dependent complex conductivity which can be tuned under electrostatic bias [6, 7]. This unique property has motivated researchers to investigate various graphene-based applications [8]. Moreover, at mid-IR spectrum, graphene exhibits low-loss plasmonic-like complex surface conductivity [9], which provides great potential on novel tunable mid-IR reflectarray antennas.

6.2 Graphene-based Reflectarray Antenna using Graphene Patch Array

Reflectarray antennas have been investigated by the research community for applications at frequencies spanning microwaves to optics [2, 10, 11].

Ideally, the unit-cell elements of a reflectarray antenna should be capable to cover a full phase-variation region of 360°. However, at IR spectrum, loss effects of metal and dielectric can restrict the phase variation to a narrow range in some cases [12]. By using low-loss materials at IR spectrum, the design of gold square-patch elements has been able to obtain 292° phase shift at 28.3 THz [13]. A reflection efficiency has been achieved as high as 92% [14].

Moreover, graphene plasmonic structures have also been exploited to manipulate the phase variation at the vicinity of the resonant frequency. Graphene ring structures [15] and graphene nanoribbons with engineered sizes have been investigated to produce a spatially varying reflection phase profile [16]. However, the phase variation of these designs depends on the physical dimensions of the unit cell elements, which cannot be dynamically tuned after fabrication. This issues can potentially be solved by using electrical tuning of the conductivity of graphene plasmonic structure [17]. In this section, the concept of a graphene patch array is presented.

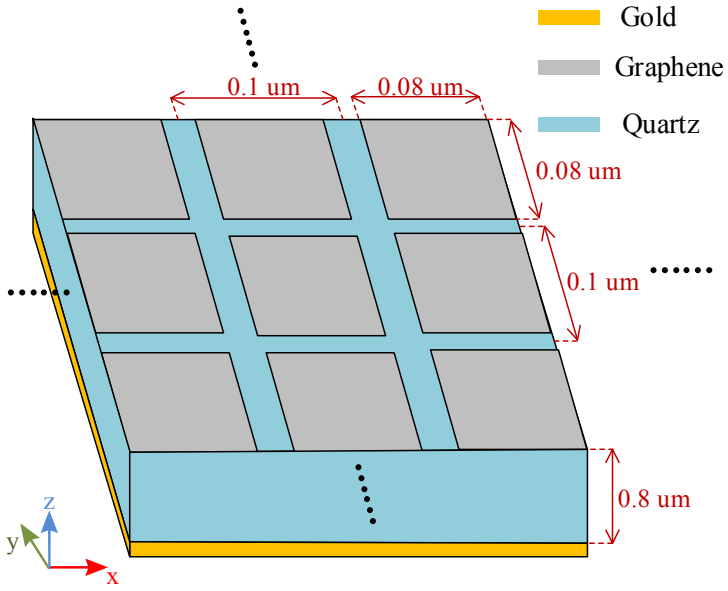

Figure 6.1: Schematic of a graphene reflectarray with graphene patches.

6.2.1 Unit Cell Design

The unit cell of the proposed antenna array consists of a square graphene patch, a SiO_2 substrate and a metallic ground plane, as shown in Figure 6.1. Similar concept has been used at low THz [18]. According to the results of the parameter sweep, the selected unit cell working at 24.5 THz has x-y dimensions of 0.1×0.1 μm^2. By changing the chemical potential of the graphene patch (0.08×0.08 μm^2), the reflection phase of the unit cell can be modified. The thickness of substrate is 0.8 μm.

In the FDTD simulations, the graphene patch is modelled by the method proposed in chapter 3. Graphene's relaxation time is set as 0.1 ps. A unit cell of the structure shown in Figure 6.1 is simulated with PBCs in the x- and y-directions. CPMLs are employed in the z-direction as absorbing boundaries to terminate simulation domains. The TF/SF boundary is used to generate the x-polarised plane waves propagating in the z-direction. Uniform cubic Yee cells with $\Delta x = \Delta y = \Delta z = 3$ nm are employed. The size of time step $\Delta t = 0.005$ fs is set. Reflection amplitude and phase of the unit cell as a function of graphene's chemical potential at 24.5 THz are plotted in Figure 6.2. The

resonant behaviour at 0.5 eV chemical potential leads to a sharp phase change. Thus, the unwrapped phase is plotted in Figure 6.2(a) to show to a continuous curve.

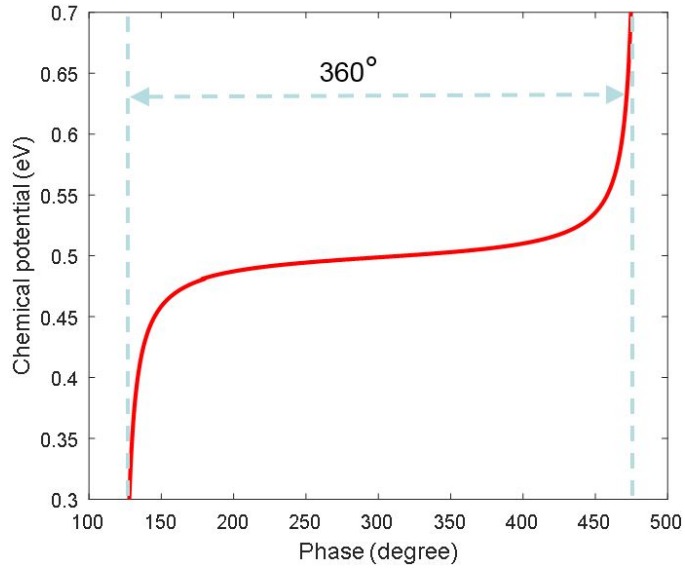

(a)

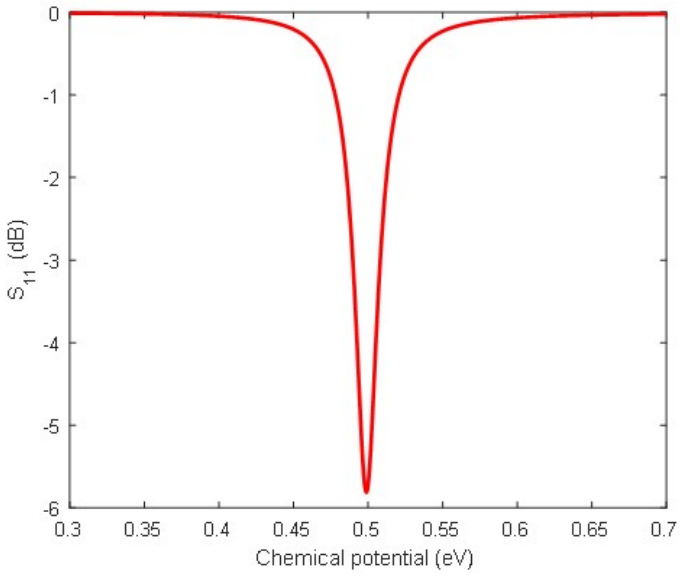

(b)

Figure 6.2: (a) A phase-versus-potential design curve for a unit-cell of graphene-based reflectarray antenna.(b) A potential-versus-S_{11} design curve for a unit-cell of graphene-based reflectarray antenna.

6.2.2 Radiation Pattern

If the reflection coefficient of each element is identical, the phase shift between the elements in x-direction and y-direction need to satisfy [19]

$$\beta_x = -kd_x \sin\theta \cos\phi \tag{6.1a}$$

$$\beta_y = -kd_y \sin\theta \sin\phi \tag{6.1b}$$

where k is the wave number, d_x is the space between the elements in the x-direction, d_y is the space between the elements in the y-direction, θ is the angle between the main beam and the x-axis, and ϕ is the angle between the main beam and the z-axis.

The far-field radiation patterns of an array of spatially distributed unit cell elements can be computed using the array theory approach [19]. The unit-cell far field pattern is calculated from the numerical simulations by considering the scattered fields in all directions above the array surface. The total radiation pattern, shown in Figure 6.3, is computed for an array of 200×200 elements and an array of 400×400 elements. The increment of element number enhance the antenna's directivity.

In addition, the UV plots of an array of 400×400 elements are shown in Figure 6.4. It is assumed that the reflection coefficient of each element is identical in Figure 6.4(a). The main beam directs to the desired direction well. However, it can be seen from Figure 6.2(b) that the reflection coefficient varies for the elements with chemical potentials between 0.4 eV and 0.6 eV. Taking the actual amplitude of reflection into account, Figure 6.4(b) demonstrates that the non-uniform reflection strength can shift away the direction of main beam.

6.2.3 Further Discussion

The nano-scaled graphene meta-surface requires a large number of graphene nano-patch resonators. By tuning the chemical potential of graphene resonators, the reflectarray is

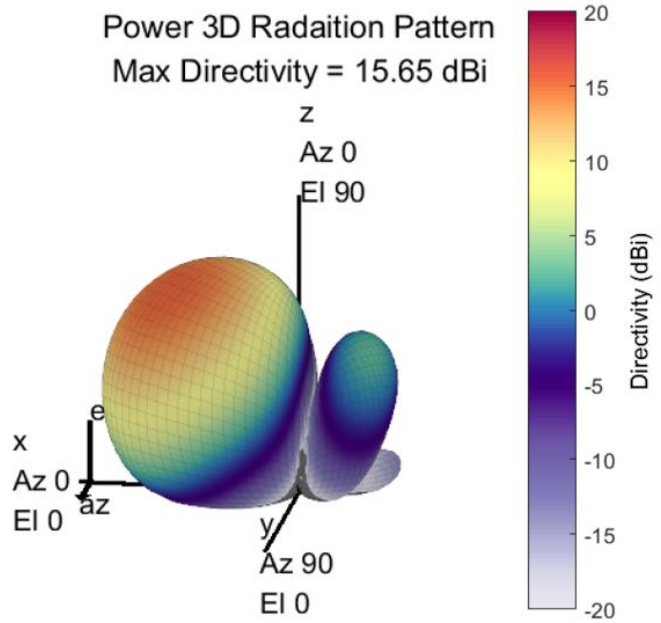

(a)

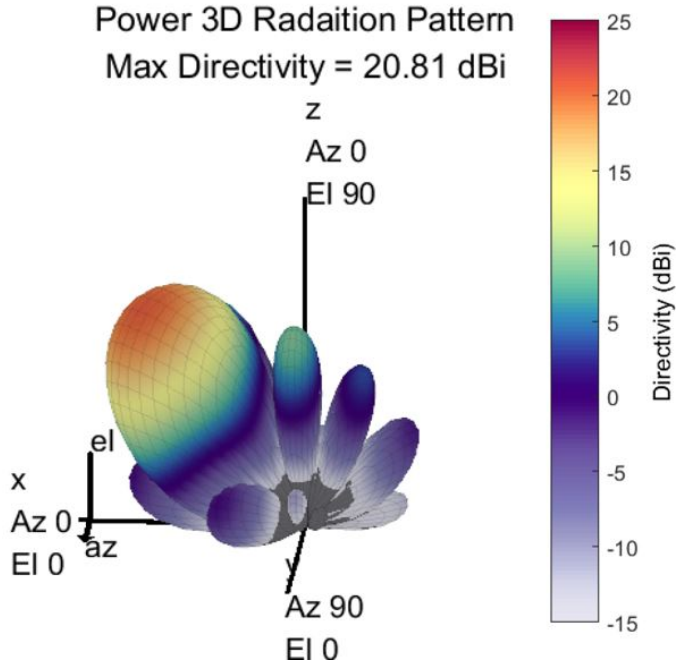

(b)

Figure 6.3: Radiation pattern ($\theta = 40°$ and $\phi = 45°$). (a) The graphene-based reflectarray consisting of 200×200 unit cells (b) The graphene-based reflectarray consisting of 400×400 unit cells

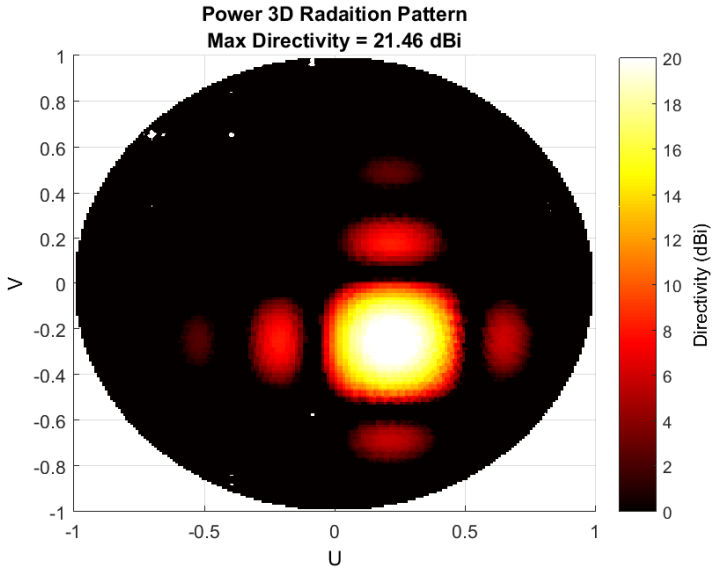

(a)

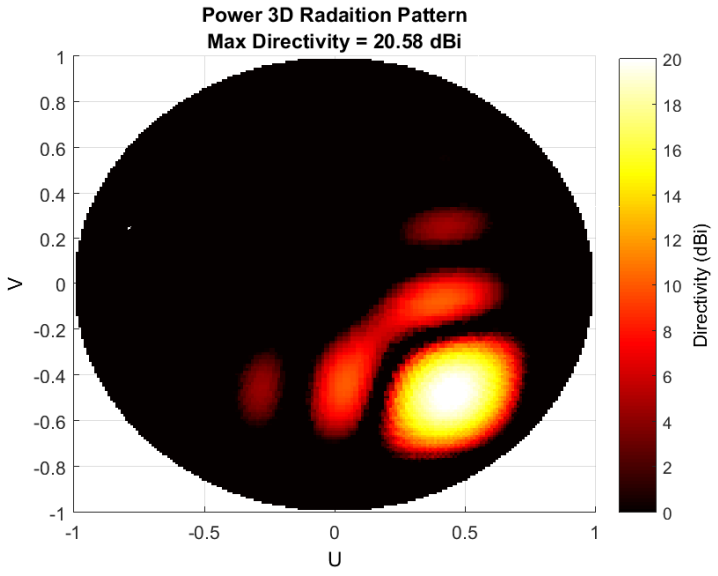

(b)

Figure 6.4: UV plot of the graphene-based reflectarray consisting of 400×400 unit cells ($\theta = 20°$ and $\phi = 40°$) (a) each element owns assumed identical reflection coefficient (b) each element owns the actual reflection coefficient as shown in the figure 6.2

able to steer an incident light beam towards different directions. However, this design requires nano-scale patterning of a large number of graphene nano-patches, which is difficult to achieve in practice. Moreover, the design require an extremely complex

voltage-bias system because each graphene patch own a unique chemical potential.

6.3 Graphene-based Reflectarray Antenna using Continuous Graphene Sheet

An electromagnetic surface with a reconfigurable phase gradient is able to steer reflected light in multiple directions. A planar array of near-resonant electromagnetic structures can be engineered to reflect an incoming beam of light to a given angle according to the Snell's Law [2]. Using the technique of array synthesis, the desired phase-gradient between adjacent array elements can be calculated through

$$\frac{\mathrm{d}\Phi}{\mathrm{d}x} = \sin\theta \times \frac{2\pi}{\lambda} \tag{6.2}$$

where $\mathrm{d}\Phi$ represents the phase difference between elements, $\mathrm{d}x$ is the dimension of a single element in the x-direction, and θ is the angle of the reflected beam of light with respect to the incident wave. By utilising tunable conductivity properties of graphene, a reconfigurable phase gradient surface has been designed where the direction of the reflected light can be controlled.

6.3.1 Unit Cell Design

The unit cell of the proposed antenna array consists of a near-resonant split-ring metallic structure deposited onto a continuous layer of graphene. Figure 6.5 (a) shows the structure of the unit cell, which consists of a continuous graphene sheet deposited onto a SiO_2 substrate with $\epsilon_r = 3$ at the relevant wavelengths [20, 21], which is backed by a metallic ground plane. A split-ring resonator structure is patterned onto the graphene layer, and the inner tooth length (L) is varied across the x-dimension of the array. The design dimensions of the SRR structure are well within the limitations of modern photolithographic techniques [20]. These SRR structures have been previously used

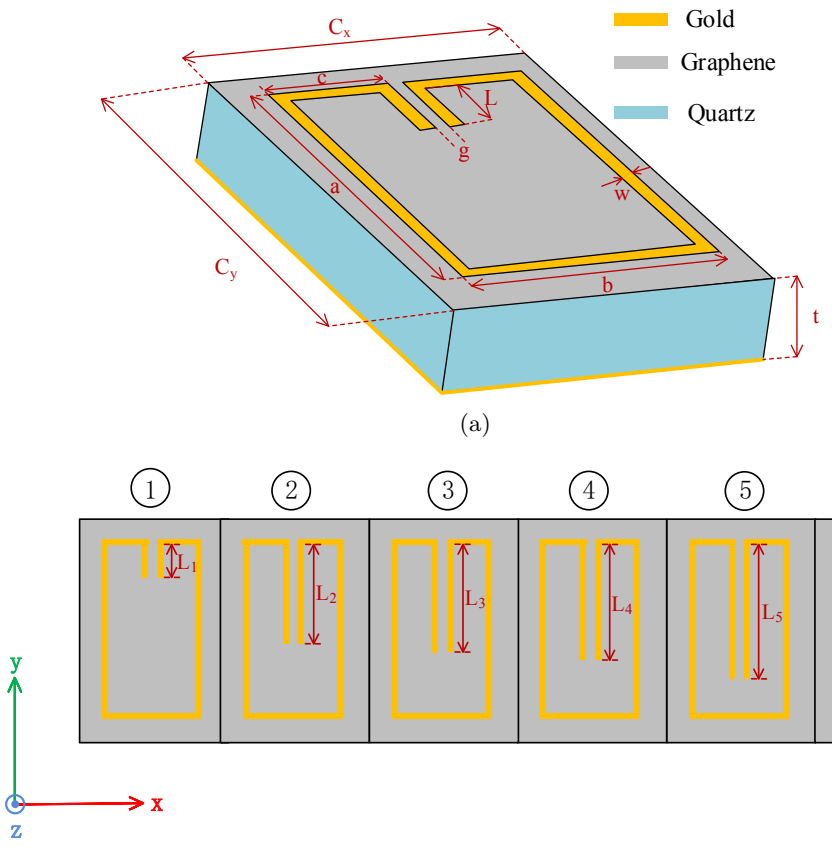

Figure 6.5: (a) Schematic of the reconfigurable graphene reflectarray unit cell. The dimensions of the unit cell are as follows, $a = 2.4$ µm, $b = 1.6$ µm, $c = 0.76$ µm, $g = 0.08$ µm, $w = 0.1$ µm, $C_x = 2$ µm and $C_y = 3$ µm. The inner tooth length (L) is varied in different unit cells. (b) Diagram of the 6-element super unit cell showing different inner tooth length. The dimensions of the inner tooth length are as follows, $L_1 = 0.1$ µm, $L_2 = 1.3$ µm, $L_3 = 1.5$ µm, $L_4 = 1.6$ µm, $L_5 = 1.8$ µm and $L_6 = 2.1$ µm

to design a phase-gradient meta-surface as a spoof plasmon polariton coupler in the microwave range [22], and provide a simple means of controlling the reflection phase when illuminated with an incident light source.

In order to obtain a constant phase gradient across the surface of the reflectarray, the inner tooth length of the split-ring is varied as shown in Figure 6.5(b). By changing the chemical potential of the graphene layer, the reflection phase of the unit cell can be modified. By carefully selecting the inner tooth length of each unit cell at the

Table 6-A: The Unit Cell Performance on the Graphene Sheet with $\mu_c = 0.1$ eV

Unit cell number	1	2	3	4	5	6
Reflection phase (degree)	0	-60	-120	-180	-240	-300
Reflection amplitude	0.97	0.91	0.7	0.59	0.66	0.82

Table 6-B: The Unit Cell Performance on the Graphene Sheet with $\mu_c = 0.9$ eV

Unit cell number	1	2	3	4	5	6
Reflection phase (degree)	-41	-40	-40	-50	-55	-59
Reflection amplitude	0.65	0.75	0.68	0.65	0.68	0.57

desired frequency of operation, the phase gradient of the whole surface can be switched between two distinct states by tuning the graphene chemical potential. As a result, a binary reflection array enabled by a continuous graphene monolayer can be realised. The reflection phase and amplitude are summarised in Table 6-A and Table 6-B. From the equation (6.2), it can be determined that, in order to reflect a 32 THz incident wave to an angle of 50°, a phase shift 60° between adjacent elements on the reflective surface is required and this can be achieved with 6 adjacent unit cells.

When the graphene layer is biased with $\mu_c = 0.1$ eV, the reflection phase of the unit cell is strongly dependent on the value of L. As the tooth length is increased from 0.1 μm to 2.1 μm the reflection phase varies by almost 300°. The amplitude of the reflection coefficient varies between 0.97 and 0.59, with the minimum at a tooth length of 1.6 μm , due to resonant effects of the metallic split-ring structure. When the μ_c is increased to 0.9 eV, the reflection amplitude varies between 0.57 and 0.75.

6.3.2 Binary Reflection

In FDTD simulations, a plane wave with linearly polarised electric fields in the $y-$direction, as shown in Figure E.1, is employed to illuminate the structure. Unit cells have been designed to work at 32 THz. Graphene sheet is modelled by the method proposed in chapter 3. Parameters of the graphene sheet are summarised in Table 6-C. A typical

Table 6-C: Graphene Properties Used in FDTD Modelling

μ_c (eV)	0.1	0.9
$\tau(ps)$	0.1	0.1
Electron mobility ($cm^2/(Vs)$)	1×10^4	1.1×10^3
σ_s ($\times 10^{-5}$ S) at 32 THz	$1.578 - 2.688i$	$2.603 - 52.281i$

relaxation time of $\tau = 0.1$ ps is assumed, and the chemical potential, μ_c is varied between 0.1 and 0.9 eV to achieve the required phase gradient modification.

As can be seen from Table 6-C, the imaginary part of surface conductivity of the graphene sheet is significantly increased when the chemical potential is increased from 0.1 eV to 0.9 eV. This has the effect of altering the impedance created by the capacitance between the inner-teeth of the SRR structure, shifting the resonant frequency away from the operational frequency of 32 THz. This phenomenon allows us to design an array with two chemical potential which can generate required phase gradient profiles in order to achieve the binary reflection effect.

The binary reflection can be confirmed through the FDTD simulations. The reflected field is obtained by eliminate the background incidence from the total filed. Figure 6.6 shows the reflected E_y field from the array surface for the two previously mentioned μ_c values, normalised to the maximum value which occurs when $\mu_c = 0.1$ eV. It can clearly be seen that the direction of the E_y field switches when the chemical potential is switched. When the chemical potential is equal to 0.9 eV, the maximum normalised field strength is at about 0.7, which is in good agreement with the reflection coefficient results obtained from the single unit cell simulations shown in Table 6-B. However, the wave front is not as flat as ideal, which should blame the effects of the uneven amplitude and phase distribution of unit cells.

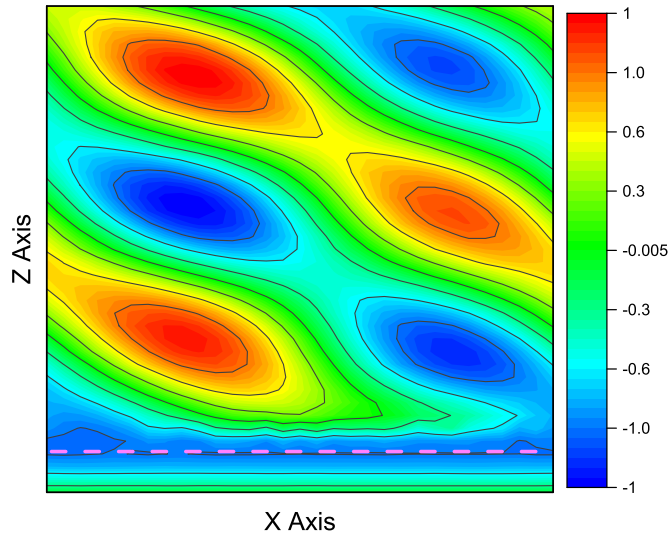

(a)

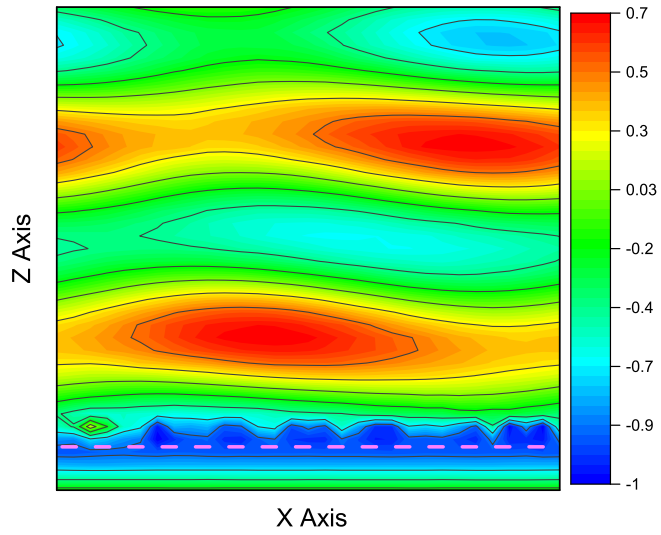

(b)

Figure 6.6: The E_y component of electric field reflected from the array surface for graphene chemical potential of 0.1 (a) and 0.9 (b) eV at 32 THz. The pink dash line represents the reflectarray surface.

6.3.3 Further Discussion

The novelty of this design lies in the utilization of a continuous single graphene sheet on which the SRR structures are deposited. The simplicity of the design and size of the features are suitable for applying common fabrication techniques such as chemical vapour disposition (CVD) and electron beam photo-lithography. By tuning the chem-

ical potential of graphene sheet through electrostatic biasing, binary-state reflection is obtained.

The proposed reconfigurable reflectarray structure does not have the ideal reflection phase and amplitude characteristics that are typically required in optimal array designs. The initial array was designed with the intention that a constant phase gradient could be achieved across the surface for two different states, and that an even amplitude distribution could be achieved, ideally close to unity. In practice, dynamically tuning between 0.1 eV and 0.9 eV would be difficult to achieve, requiring large electric fields.

6.4 Summary

In this chapter, we have proposed two designs for graphene-enabled reconfigurable reflectarray antennas operating in the mid-infrared spectrum. The first structure is based on an array of graphene patch. The second one utilises a continuous graphene sheet with an aperiodic array of near-resonant metallic split-ring structures. By tuning the chemical potential of the graphene, both structures are able to change the reflection phase of unit cells to achieve required phase distribution on the reflective surface. The proposed designs open up the possibility of novel applications at mid-infrared wavelength in imaging and communications.

References

[1] D. Berry, R. Malech, and W. Kennedy, "The reflectarray antenna," *IEEE Transactions on Antennas and Propagation*, vol. 11, no. 6, pp. 645–651, 1963.

[2] N. Yu, P. Genevet, M. A. Kats, F. Aieta, J.-P. Tetienne, F. Capasso, and Z. Gaburro, "Light propagation with phase discontinuities: generalized laws of reflection and refraction," *Science*, p. 1210713, 2011.

[3] D. C. Fernandez, R. Bhargava, S. M. Hewitt, and I. W. Levin, "Infrared spectroscopic imaging for histopathologic recognition," *Nature Biotechnology*, vol. 23, no. 4, p. 469, 2005.

[4] A. P. Michel, P. Q. Liu, J. K. Yeung, P. Corrigan, M. L. Baeck, Z. Wang, T. Day, F. Moshary, C. F. Gmachl, and J. A. Smith, "Quantum cascade laser open-path system for remote sensing of trace gases in Beijing, China," *Optical Engineering*, vol. 49, no. 11, p. 111125, 2010.

[5] J. P. Gianvittorio and Y. Rahmat-Samii, "Reconfigurable patch antennas for steerable reflectarray applications," *IEEE Transactions on Antennas and Propagation*, vol. 54, no. 5, pp. 1388–1392, 2006.

[6] V. W. Brar, M. S. Jang, M. Sherrott, J. J. Lopez, and H. A. Atwater, "Highly confined tunable mid-infrared plasmonics in graphene nanoresonators," *Nano Letters*, vol. 13, no. 6, pp. 2541–2547, 2013.

[7] L. Falkovsky, "Optical properties of graphene," in *Journal of Physics: Conference Series*, vol. 129, no. 1. IOP Publishing, 2008, p. 012004.

[8] T. Low and P. Avouris, "Graphene plasmonics for terahertz to mid-infrared applications," *ACS Nano*, vol. 8, no. 2, pp. 1086–1101, 2014.

[9] S. H. Mousavi, I. Kholmanov, K. B. Alici, D. Purtseladze, N. Arju, K. Tatar, D. Y. Fozdar, J. W. Suk, Y. Hao, A. B. Khanikaev *et al.*, "Inductive tuning of Fano-resonant metasurfaces using plasmonic response of graphene in the mid-infrared," *Nano Letters*, vol. 13, no. 3, pp. 1111–1117, 2013.

[10] J. Huang and J. A. Encinar, *Reflectarray antennas*. John Wiley & Sons, 2007, vol. 30.

[11] T. Niu, W. Withayachumnankul, B. S.-Y. Ung, H. Menekse, M. Bhaskaran, S. Sriram, and C. Fumeaux, "Experimental demonstration of reflectarray antennas at terahertz frequencies," *Optics Express*, vol. 21, no. 3, pp. 2875–2889, 2013.

[12] F. Yang, P. Nayeri, A. Z. Elsherbeni, J. C. Ginn, D. J. Shelton, G. D. Boreman, and Y. Rahmat-Samii, "Reflectarray design at infrared frequencies: Effects and models of material loss," *IEEE Transactions on Antennas and Propagation*, vol. 60, no. 9, p. 4202, 2012.

[13] J. C. Ginn, B. A. Lail, and G. D. Boreman, "Phase characterization of reflectarray elements at infrared," *IEEE Transactions on Antennas and Propagation*, vol. 55, no. 11, pp. 2989–2993, 2007.

[14] M. Farmahini-Farahani and H. Mosallaei, "Birefringent reflectarray metasurface for beam engineering in infrared," *Optics Letters*, vol. 38, no. 4, pp. 462–464, 2013.

[15] P. Liu, W. Cai, L. Wang, X. Zhang, and J. Xu, "Tunable terahertz optical antennas based on graphene ring structures," *Applied Physics Letters*, vol. 100, no. 15, p. 153111, 2012.

[16] E. Carrasco, M. Tamagnone, J. R. Mosig, T. Low, and J. Perruisseau-Carrier, "Gate-controlled mid-infrared light bending with aperiodic graphene nanoribbons array," *Nanotechnology*, vol. 26, no. 13, p. 134002, 2015.

[17] L. Ju, B. Geng, J. Horng, C. Girit, M. Martin, Z. Hao, H. A. Bechtel, X. Liang, A. Zettl, Y. R. Shen *et al.*, "Graphene plasmonics for tunable terahertz metamaterials," *Nature Nanotechnology*, vol. 6, no. 10, p. 630, 2011.

[18] E. Carrasco and J. Perruisseau-Carrier, "Reflectarray antenna at terahertz using graphene," *IEEE Antennas and Wireless Propagation Letters*, vol. 12, pp. 253–256, 2013.

[19] A. B. Constantine *et al.*, "Antenna theory: analysis and design," *third edition, John wiley & sons*, 2005.

[20] E. Buitrago, R. Fallica, D. Fan, T. S. Kulmala, M. Vockenhuber, and Y. Ekinci, "SnOx high-efficiency EUV interference lithography gratings towards the ultimate resolution in photolithography," *Microelectronic Engineering*, vol. 155, pp. 44–49, 2016.

[21] G. Power, J. Vij, and M. Shaw, "Refractive index at infrared wavelengths and dielectric permittivity of pure and fluorinated silicon dioxide from measurements of their thin films deposited on Si," *Journal of Physics D: Applied Physics*, vol. 37, no. 9, p. 1362, 2004.

[22] J. Wang, S. Qu, H. Ma, Z. Xu, A. Zhang, H. Zhou, H. Chen, and Y. Li, "High-efficiency spoof plasmon polariton coupler mediated by gradient metasurfaces," *Applied Physics Letters*, vol. 101, no. 20, p. 201104, 2012.

Chapter 7

Conclusion and Future Work

In this chapter, the work presented in this thesis is summarised, and a few ideas for the future research are also proposed.

7.1 Conclusion

This section summarises the main work in each chapter and the main contributions of the thesis.

Chapter 1 introduces two important concepts in the thesis: the THz spectrum and numerical modelling methods.

Chapter 2 provides the background of graphene including fabrication, electronic properties, plasmonics and devices.

Chapter 3 depicts the FDTD modelling on linear response of graphene. An FDTD method based on the auxiliary element is proposed. The validation work compares FDTD results with theoretical and experimental results from different aspects such as transmission coefficient, reflection coefficient, Faraday rotation and Kerr rotation. The comparison demonstrates a good agreement. The modelling method is suitable for

graphene-based structures with both electrostatic bias and magnetostatic bias.

Chapter 4 depicts the FDTD modelling on the nonlinear response of graphene. An FDTD method based on $J-E$ characteristics is proposed. The modelling method demonstrates simulation results on odd-harmonic generations and frequency-mixing effects. The modelling work numerically investigated the effects of chemical potential on the nonlinearity of graphene. The results of parameter sweeps indicate the existence of the optimised chemical potential for nonlinear response of graphene.

Chapter 5 describes the work on a magnetically tunable graphene-based reflector under linear polarised incidence at room temperature. The details of modelling, fabrication and measurement are provided. The experimental results mainly focus on the variation in reflection intensity. The effects of chemical potential, magnetostatic bias and Kerr rotation are discussed via numerical modelling. Numerical investigation demonstrates that graphene with lower chemical potential can be used to increase the tunability of magnetostatic bias.

Chapter 6 describes the work on two graphene-based reflectarray antennas. Their performance is numerically investigated. The first structure is a graphene patch array, which theoretically, the reflective surface can realise various phase distribution. However, the non-uniform distribution of the reflection amplitude shifts the main beam away from the desired direction. The second one is based on a continuous graphene sheet with an array of metallic split-ring structures. By tuning the chemical potential of the continuous graphene, two states of reflection can be obtained. Due to the fixed physical dimensions of split-ring structures, its phase distribution cannot be as flexible as the graphene patch array.

The main contributions of this thesis are summarised as below:

1. A novel FDTD method based on auxiliary element method has been proposed for tunable linear responses of graphene. FDTD results are compared with theoretical results and measurement results from published literature. In addition, a novel FDTD

method has also been proposed for the nonlinear electrodynamic responses of graphene at terahertz frequencies. Simulation results demonstrate nonlinear phenomena in wave transmission through graphene. The proposed modelling methods can be used to design graphene-based devices.

2. Graphene-based reflectors with magnetostatic bias are explored under linear polarised illumination at room temperature. An ECM has been modified and validated with full-wave simulations in order to extract the parameters of graphene used in measurements. Experimental results demonstrate a maximum intensity variation of 15% at the magnetostatic bias of 6 T. The work also numerically studies the reflection variation and the Kerr rotation.

3. Two designs of graphene-based reflectarray antennas with electrostatic tunability are numerically investigated. The reflection performance is analysed from the aspects of amplitude distribution and phase distribution. The work demonstrates the direction on potential optimised designs.

7.2 Future Work

Based on the work presented in this thesis, the following aspects are proposed as the potential for further research:

1. The FDTD method on graphene nonlinearity proposed in the thesis can demonstrate the nonlinear phenomenon of graphene. However, there is still a lack of qualitative comparison with experimental data. Thus, it is necessary that there will be more work on the validation of the proposed nonlinear modelling method.

2. The tunability of graphene-based reflectors in chapter 5 depends on the high strength of magnetostatic bias. The required strength is expected to be reduced by employing graphene metasurfaces which can enhance the anisotropic response of graphene.

3. The first design of reflectarray antennas suffers from non-uniform amplitude distribution and complex voltage-bias network. The second design of reflectarray antennas can avoid these problems. However, the phase distribution is not flexible enough to support multi-state reflection. Optimised designs are expected to deal with these issues.

4. The experimental work in the literature has shown the frequency-dispersive relaxation time of graphene encapsulated in h-BN materials. The existing FDTD modelling methods have not taken this aspect into account. It is necessary to extend the capability of FDTD modelling to cover the frequency-dispersive relaxation time.

Appendix A

Author's publications

Journal papers

1. **L. Yang**, J. Tian, K. Z. Rajab, and Y. Hao, "FDTD Modeling of Nonlinear Phenomena in Wave Transmission Through Graphene," *IEEE Antennas and Wireless Propagation Letters*, vol. 17, no. 1, pp. 126–129, 2018.

2. **L. Yang**, J. Tian, H. Giddens, JM. Poumirol, J.B. Wu, A.B. Kuzmenko, and Y. Hao "Magnetically tunable graphene-based reflector under linear polarized incidence at room temperature," *Applied Physics Letters* , vol. 112, no. 151103, 2018.

3. H Giddens, **L Yang**, J Tian, and Y Hao, "Mid-Infrared Reflect-Array Antenna with Beam Switching Enabled by Continuous Graphene Layer," *IEEE Photonics Technology Letters*, vol. 30, no. 8, pp. 748–751, 2018.

Conference papers

1. **L. Yang**, K. Z. Rajab, and Y. Hao, "FDTD Modelling on Intraband Gyrotropic Conductivity of Graphene," *2016 URSI Asia-Pacific Radio Science Conference* , Seoul, Korea, August 21-25, 2016.

Appendix B

FDTD Updating Equations Used for Glass and ITO

In the FDTD modelling, the glass and ITO have been described as fourth-pole Debye medium and Drude medium respectively.

The Ampere's law in the frequency domain can be expressed for the pth-pole Debye medium as

$$\nabla \times \mathbf{H} = \varepsilon_0 \left(\varepsilon_\infty + \sum_{p=1}^{P} \frac{\Delta\varepsilon_p}{1 + j\omega\tau_p} \right) j\omega\mathbf{E}. \tag{B.1}$$

Let the polarisation current with the pth-pole defined as

$$\mathbf{J}_p = \varepsilon_0 \Delta\varepsilon_p \left(\frac{j\omega}{1 + j\omega\tau_p} \right) \mathbf{E}. \tag{B.2}$$

The updating equation of time-domain electric filed of glass can be expressed as

$$\mathbf{E}^{n+1} = \mathbf{E}^n + \left(\frac{2\Delta t}{2\varepsilon_0\varepsilon_\infty + \sum_{p=1}^{P} \beta_p} \right) \cdot \left[\nabla \times \mathbf{H}^{n+1/2} - \frac{1}{2} \sum_{p=1}^{P} (1 + k_p)\mathbf{J}_p^n \right] \tag{B.3}$$

where $k_p = (2\tau_p - \Delta t)/(2\tau_p + \Delta t)$, $\beta_p = (\varepsilon_0 \Delta\varepsilon_p \Delta t)/(\tau_p + 0.5\Delta t)$ and $\mathbf{J}_p^n = k_p \mathbf{J}_p^{n-1} +$

$\beta_p(\mathbf{E}^n - \mathbf{E}^{n-1})/\Delta t$

The Ampere's law in the frequency domain can be expressed for the Drude medium as

$$\nabla \times \mathbf{H} = \varepsilon_0 \left(\varepsilon_\infty - \frac{\omega_p^2}{\omega^2 - j\omega\tau^{-1}} \right) j\omega \mathbf{E}. \tag{B.4}$$

Let the polarisation current of Lorentz medium defined as

$$\mathbf{J} = \left(\frac{-\varepsilon_0 \omega_p^2 j\omega}{\omega^2 - j\omega\tau^{-1}} \right) \mathbf{E}. \tag{B.5}$$

The updating equation of time-domain electric filed of ITO can be expressed as

$$\mathbf{E}^{n+1} = \left(\frac{2\varepsilon_0\varepsilon_\infty - \Delta t\beta}{2\varepsilon_0\varepsilon_\infty + \Delta t\beta} \right) \mathbf{E}^n + \left(\frac{2\Delta t}{2\varepsilon_0\varepsilon_\infty + \Delta t\beta} \right) \cdot \left[\nabla \times \mathbf{H}^{n+1/2} - \frac{1}{2} k J^n \right] \tag{B.6}$$

where $k = (2\tau - \Delta t)/(2\tau + \Delta t)$, $\beta = (\varepsilon_0 \tau \omega_p^2 \Delta t)/(2\tau + \Delta t)$ and $\mathbf{J}^n = k\mathbf{J}^{n-1} + \beta(\mathbf{E}^n + \mathbf{E}^{n-1})/\Delta t$

Appendix C

Scanning Electron Microscope of ITO

In the literature, as discussed in chapter 5, the parameters of an ITO film depend on its thickness. With the help of Dr. Hangfeng Zhang at QMUL, the thickness of the ITO film in the sample has been obtained from the scanning electron microscope image shown in Figure C.1.

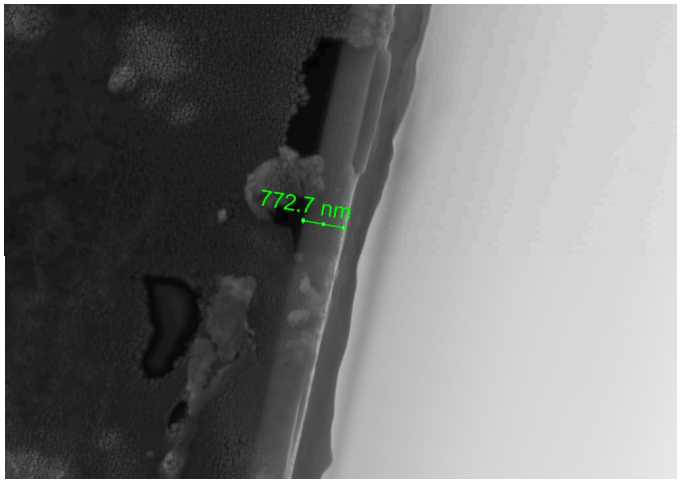

Figure C.1: The scanning electron microscope image of the ITO film with 772.7 nm thickness.

Appendix D

Raw Measurement Data

In this appendix, the raw data of magnetostatic measurement in chapter 5 is shown in Figure D.1 and Figure D.2. The variation of reflection intensity of the graphene-based sample in Figure D.1 is small. With the considerations of any variation in the measurement system due to the generation of the magnetic field, a gold mirror was used as reference. The data of the reference sample in Figure D.2 indicates that the system variation can be ignored.

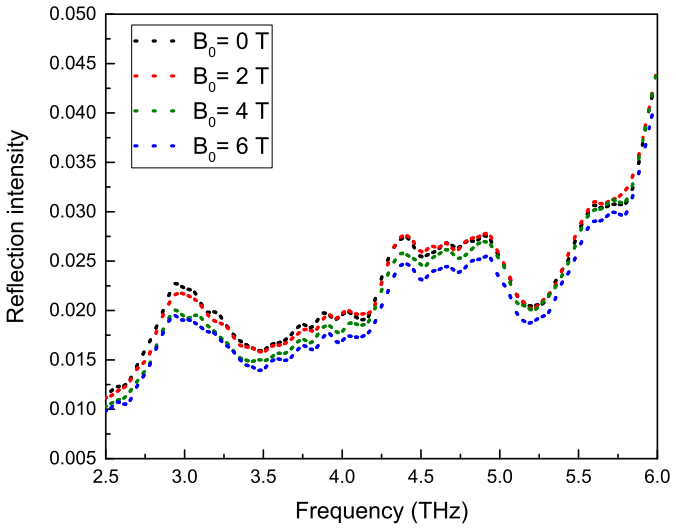

Figure D.1: Absolute reflection intensity of graphene-based sample used in FTIR measurement.

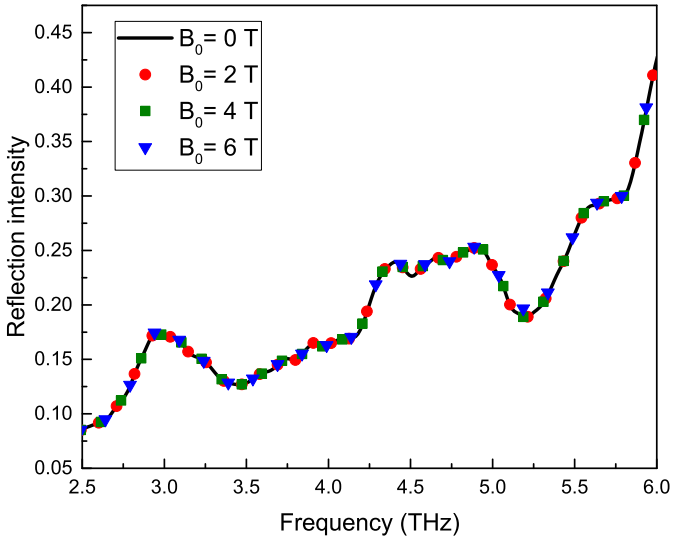

Figure D.2: Absolute reflection intensity of gold mirror used as reference in FTIR measurement.

Appendix E

Plane-wave Excitation Used in Chapter 6

In this appendix, the image of plane-wave excitation used in FDTD simulations to illuminate reflectarray structures is provided, as shown in Figure E.1.

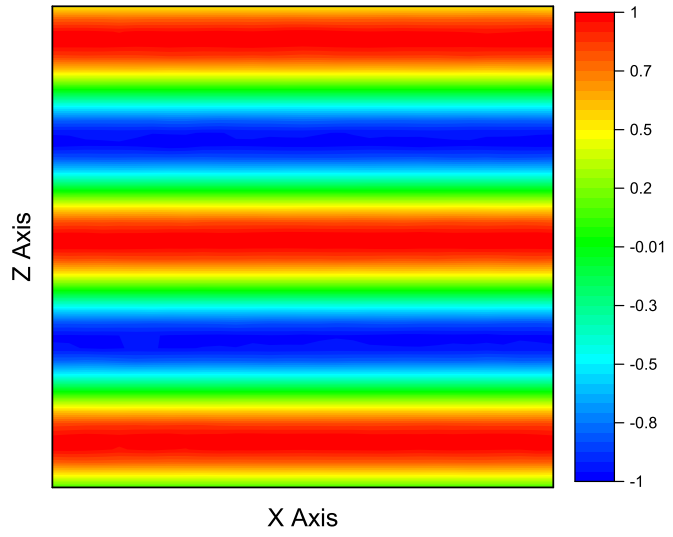

Figure E.1: The plane-wave excitation with the absence of structures in FDTD simulations